Environmental sciences and engineering

SIE Master Project

Novelty Detection in Convolutional Neural Network Using Density Forest

Author:

Cyril Wendl

Supervisors:

Prof. Devis Tuia (WUR)
Diego Marcos (WUR)
Prof. François Golay (EPFL)

Spring semester 2018

Wageningen, August 14, 2018

Acknowledgements

I would first and foremost like to thank my supervisors Devis Tuia and Diego Marcos who, with their helpful guidance, critical questions and regular feed-back greatly helped me make a hopefully meaningful scientific contribution. I would like to thank Devis Tuia in particular for his financial and administrative support in allowing me to spend a semester at the University of Wageningen. The regular exchange with PhD students and researchers of the GRS lab was a strongly motivating factor throughout my thesis. I would like to thank Diego Marcos in particular for his regular availability, assistance and critical-feedback to my numerous questions.

Secondly, I would like to address special thanks to my secondary supervisor Prof. François Golay at EPFL (École Polytechnique Fédérale de Lausanne), who supported my Master thesis greatly and allowed me to spend the last week of my thesis at EPFL.

I would first and foremost like to thank my family for having supported me both morally and financially during my Master and Bachelor studies at EPFL and at the University of Fribourg respectively.

Contents

List of Figures ii

List of Tables v

Acronyms vi

1 Introduction 1

2 Literature Review 3
- 2.1 Methods Based on Network Output . . . 4
  - 2.1.1 Single-Pass Methods . . . 4
  - 2.1.2 Invariance to Image Transformations . . . 5
  - 2.1.3 MC-Dropout . . . 6
- 2.2 Methods Based on Network Activations . . . 6
- 2.3 Network Architectures for Confidence Estimation . . . 7
- 2.4 Comparison to Novelty Detection Methods . . . 7
- 2.5 Summary . . . 7

3 Methodology 8
- 3.1 Overview: Density Forests . . . 8
- 3.2 Decision Trees . . . 9
- 3.3 Random Forests . . . 10
- 3.4 Density Forests . . . 10

4 Datasets 13
- 4.1 Synthetic Datasets . . . 13
- 4.2 Modified National Institute of Standards and Technology (MNIST) Dataset . . . 14
- 4.3 Zurich Dataset . . . 15

5 Experimental Setup 16
- 5.1 Network Architectures . . . 16
- 5.2 Novelty Detection Baselines . . . 18
- 5.3 Dimensionality Reduction and Data Separability . . . 19
- 5.4 Evaluation . . . 21
- 5.5 Hyperparameter Search . . . 21

6 Results 23
- 6.1 Experiments . . . 23
- 6.2 Synthetic Data . . . 23
- 6.3 MNIST . . . 25
- 6.4 Zurich Dataset . . . 30
- 6.5 Overall Results . . . 30
- 6.6 Visual interpretation . . . 34
- 6.7 Particular Objects . . . 41

7 Discussion 44

7.1 MNIST dataset . . . 44
7.2 Zurich dataset . . . 44

8 Conclusion **45**
8.1 Main Contributions . . . 46
8.2 Future Research . . . 47

9 Appendices **53**
A Code Documentation . . . 53
B Random Forest . . . 53
C Data Structure . . . 55
D MNIST Evaluation Metrics . . . 56
E Zurich Network Architecture . . . 57
F MNIST Dataset Figures . . . 58
G Zurich Dataset Figures . . . 60
H Hyperparameter Search Results . . . 72

List of Figures

1 Invariance To Image Transformation: Schema for MNIST digit example [2]. . . . 5
2 Workflow Diagram . . . 9
3 Illustration of tree growth for a fictive dataset. Covariance ellipses are indicated in red lines and splitting lines in red dotted lines, indicating the dimension and value along which a node is split. D_i and V_i denote the split dimension and value of the i-th split. Nodes are considered leaf nodes when no further split is necessary or possible, either because the Information Gain of a new split would lower than a defined threshold or because the maximum tree depth is reached. In a Density Forest, every tree would see a subset of all points and fit slightly different leaf nodes each time. . . . 12
4 Synthetic datasets . . . 14
5 Sample images of the MNIST dataset for true y labels 0 to 9 [26] . . . 14
6 Sample pair of images and ground truth for the Zurich dataset [54] . . . 15
7 Label distribution in the Zurich dataset . . . 16
8 U-Net architecture, according to Ronneberger et al. [43]. Numbers on top of each blue block indicate the number of filters, numbers on the bottom left of the blocks indicate the resolution of each filter. . . . 17
9 Explained variance as a function of the number of components . . . 19
10 t-distributed Stochastic Neighbor Embedding (t-SNE) schema with toy data. t-SNE finds a mapping between the original, high-dimensional data (left) and the data in a lower dimensionality (right). Classes of data points are shown in blue, red and green. If data points within the same class are more similar to each other in high-dimensional space, they will be closer to each other in the t-SNE visualization. . . . 20

11 Parameter Search: Gray boxes show activations belonging to data points of seen classes, red boxes activations belonging to data points of the unseen class. In principle, the true class label is unknown for the test set. For each hyperparameter combination, the classifier is trained `n` times on a subset of the training set activations belonging only to seen classes (blue arrow) and evaluated on a subset of the seen and unseen points of the validation set (green arrows). The best hyperparameter combination found that way is applied to the entire test set (gray arrows), predicting for every point whether it belongs to a seen or unseen class. 22
12 Covariance ellipses of individual Density Tree (subset of all points shown) 23
13 Splitting steps of a single node, showing the data, covariance ellipses and information gain of the parent node for dataset 2 24
14 Gaussian Probability Density Function (PDF) distribution according to single tree, and according to a Density Forest consisting of 20 trees 25
15 Predicted labels for networks with left-out classes 4 and 8 (top) and 1 and 7 (bottom). While digits showing a 4 are mostly mislabeled as a 9, the digit 8 is mislabeled less homogeneously. While one could suppose that digits 1 and 7 look similar and might be confused, digits 7 are mostly classified as digit 9, and digit 1 mostly as digits 4 and 8. 27
16 t-SNE of MNIST activations, model with left-out class 7. Both before and after Principal Component Analysis (PCA), activations of different classes seem well separable, including the unseen class. 28
17 t-SNE of MNIST activations, after PCA transformations. 29
18 Prediction and ground truth for the model trained without the roads class 31
19 Predictions for network with left-out class "roads" and "trees". While roads are mostly mislabelled as buildings, trees are mislabelled less homogeneously. 31
20 t-SNE of Zurich dataset activations, model with left-out class buildings. The same number of points are shown by class, although the real class distribution is imbalanced (cf. table 8). 32
21 t-SNE of Zurich dataset activations after PCA. 33
22 Original and equalized confidence distributions for Density Forest (DF), using the left-out class "Roads". While outliers are visible in the original figure, smaller confidence differences between classes are better visible after histogram equalization. . . . 35
23 Visual uncertainty results for selected methods on left-out class "Roads" and corresponding ground truth. Contrast stretching and histogram equalization have been applied to One-Class Support Vector Machines (OC-SVM) and DF images for better visibility. Variance per PCA component and Receiver Operating Characteristic (ROC) curves are shown below the confidence images. 36
24 Visual uncertainty results for selected methods on left-out class "Trees" and corresponding ground truth. Contrast stretching and histogram equalization have been applied to OC-SVM and DF images for better visibility. Variance per PCA component and ROC curves are shown below the confidence images. 38

25 Confidence for the left-out class "Trees" according to different methods plotted onto t-SNE, showing the n points with the lowest confidence where n is the number of points per class shown in the t-SNE plot. Points of the unseen classes are indicated with a solid-edge circle. Ideally, all solid-edge circles should be red, and all other points green. The original t-SNE plot and the ROC curves for each method are shown for comparison. 40
26 Swimming pool object with MSR and DF confidence images 42
27 Soccer pitch object with Maximum Softmax Response (MSR) and DF confidence scores 43
28 Alternative confidence measure scheme: red parts are to be retrieved and multiplied to measure the degree of agreement of the softmax inputs. 48
B.1 Decision boundaries of a single Decision Tree on 2-dimensional synthetic data, splitting the data until every leaf node only contains data of one cluster. Left: decision boundaries with Data, right: decision boundaries only. The Decision Tree clearly overfits the data. 53
B.2 Decision tree with unlimited depth on the training data for shown for illustrative purposes, with the split dimension and value at every non-leaf node and the class label at every leaf node. The tree clearly overfits the data and produces edgy decision boundaries 54
B.3 Decision boundaries of a Random Forest on 2-dimensional synthetic data. 1000 Decision Trees have been trained on a 30% bootstrap sample of the original data. Left: decision boundaries with Data, right: decision boundaries only. The Random Forest manages to smooth out the class decision boundaries. 54
C.1 Implemented data structure for Decision Tree nodes. Every node saves a pointer to its parent, the unique labels contained at its split level, the split dimension and value, methods for tree descending and formatting as well information about its child nodes. 55
C.2 Implemented data structure for Density Tree nodes. Every node saves a pointer to its parent, the unique labels contained at its split level, the split dimension and value, methods for tree descending and formatting as well information about its child nodes. In addition, every root node pre-stores the inverse and determinant of the covariance matrix of both clusters situated to the right and left of the node for faster calculation of the Gaussian PDF. 55
F.1 Count of predictions for each left-out class 58
F.2 t-SNE of MNIST dataset activations after PCA transformations for each left-out class 59
G.1 Explained variance by first PCA components, for activations of each left-out class and for activations of the model trained on all classes. The number of PCA components was chosen such as to explain more than 95% of the variance. 60
G.2 t-SNE of Zurich dataset activations after PCA transformations for each left-out class and for the activations of the network trained on all classes. The same number of points are shown by class to show class separability, although the real class distribution is imbalanced (cf. table 8). 61
G.3 Image and ground truth for visualized novelty detection methods 62
G.4 Ground truth and visual results for left-out class "roads". 63
G.5 Ground truth and visual results for left-out class "buildings". 64
G.6 Ground truth and visual results for left-out class "trees". 65
G.7 Ground truth and visual results for left-out class "grass". 66
G.8 Ground truth and visual results for left-out class "bare soil". 67

G.9 Ground truth and visual results for left-out class “water”. 68
G.10 Ground truth and visual results for left-out class “railways”. 69
G.11 Ground truth and visual results for left-out class “swimming pools”. 70
G.12 ROC curves of confidence measures for novelty detection and for error detection . . 71
H.1 Radial Basis Function (RBF) Kernel visualizations for One-Class Support Vector Machines in Zurich dataset. Kernels were applied to a class-balanced subsample of training activations belonging to the seen classes. Best kernels found using hyperparameter search are labelled in bold. 73
H.2 Polynomial kernel visualizations for One-Class Support Vector Machines in Zurich dataset with best degree r. Kernels were applied to a class-balanced subsample of training activations belonging to the seen classes. Contrast stretching has been applied to the images of the polynomial kernels to highlight more local variation. Best kernels found using hyperparameter search are labelled in bold. 74

List of Tables

1 Summary of reviewed confidence measures for neural networks. Implemented baselines are indicated in bold. 8
2 Density Forest parameters and suggested parameter ranges 13
3 Architecture of the Convolutional Neural Network (CNN) used for MNIST digit classification. $|b|$ = batch size, p = dropout probability. 17
4 Confusion Matrix for classification problem with r classes. UA = User's Accuracy = Precision, PA = Producer's Accuracy = Recall, OA = Overall Accuracy, $1, 2, \ldots, r$=classes. n_{ij} counts the number of labels predicted as class i and belonging to the true class j. Bullet indexes signify either the sum of the row (e.g., $n_{O\bullet}$), the sum of the column (e.g., $n_{\bullet O}$) or the sum of all elements of the Confusion Matrix ($n_{\bullet\bullet}$). 21
5 Density Forest parameters for each dataset 22
6 Mean Overall Accuracy in % for the CNN models trained on $N-1$ classes 26
7 Mean Area Under the curve of the Receiver Operating Characteristic (AUROC) for each left-out class in the MNIST dataset 29
8 Test set accuracy for the UNET CNN trained on all classes (Overall Accuracy: 77.59 %) 30
9 Accuracy measures for the UNET CNN trained on $N-1$ classes. 30
10 AUROC for each left-out class 34
D.1 Accuracy metrics in % for the CNN trained on $N-1$ classes for the MNIST dataset 56
D.2 AUROC for each left-out class in the MNIST dataset 56
E.1 U-Net Architecture of the CNN used for Zurich Dataset, according to Ronneberger et al. [43]. Conv. = convolution, filt = filters, str = stride, p = dropout probability, dim = dimensions, Input dimensions $|b|, w, h, n_c$ = batch size, width, height, number of channels. A convolution or transpose convolution always takes the previous layer in the network as input. 57
H.1 Best hyperparameters for the MNIST Dataset 72
H.2 Best hyperparameters for the Zurich Dataset 73

Acronyms

AA	Average Accuracy
AI	Artificial Intelligence
AUC	Area Under the Curve
AUROC	Area Under the curve of the Receiver Operating Characteristic
BNN	Bayesian Neural Network
CM	Confusion Matrix
CNN	Convolutional Neural Network
DF	Density Forest
EM	Expectation-Maximization
FC	Fully Connected
GMM	Gaussian Mixture Models
GPU	Graphics Processing Unit
IF	Isolation Forest
IG	Information Gain
***k*-NN**	k-Nearest Neighbors
KS	Kolmogorov-Smirnov
LOF	Local Outlier Factor
MC-Dropout	Monte-Carlo Dropout
ML	Machine Learning
MLP	Multi-Layer Perceptron
MNIST	Modified National Institute of Standards and Technology
MSR	Maximum Softmax Response
OA	Overall Accuracy
OC-SVM	One-Class Support Vector Machines
PCA	Principal Component Analysis
PDF	Probability Density Function
RBF	Radial Basis Function
ReLU	Rectified Linear Unit
RF	Random Forest
ROC	Receiver Operating Characteristic
SVM	Support Vector Machine
t-SNE	t-distributed Stochastic Neighbor Embedding

Abstract

Uncertainty in deep learning has recently received a lot of attention in research. While state-of-the-art neural networks have managed to break many benchmarks in terms of accuracy, it has been shown that they are susceptible to fooling, yielding unreasonably high confidence scores while being wrong by applying minor perturbations to the input. While some research has gone into the design of new architectures that are probabilistic in nature, such as Bayesian Neural Networks, other researchers have tried to model uncertainty of standard architectures heuristically. This work presents a novel method to assess uncertainty in Convolutional Neural Networks, based on fitting a forests of randomized Decision Trees to the network activations before the final classification layer. Experiments are provided for patch classification on the MNIST dataset and for semantic segmentation on satellite imagery used for land cover classification. The land cover dataset consists of overhead imagery of the city of Zurich in Switzerland taken in 2002, with corresponding manually annotated ground truth. The Density Forest confidence estimation method is compared to a number of baselines based on softmax activations and pre-softmax activations. All methods are evaluated with respect to novelty detection. Confidence methods based on pre-softmax activations show better overall performance in the Zurich dataset than softmax measures, while for the MNIST dataset softmax measures outperform pre-softmax based novelty detection measures. Main reasons for the varying performance are related to the curse of dimensionality when working with high-dimensional activation vectors and class separability issues with partially trained networks.

Keywords: Uncertainty, neural networks, Decision Trees, Density Forest, novelty detection, patch classification, semantic segmentation, remote sensing, land cover classification

1 Introduction

The recent breakthroughs in Machine Learning (ML), Artificial Intelligence (AI) and in computing power have set new accuracy standards in many computer vision tasks, including, but not limited to, medical applications [27, 43], autonomous driving [28] and remote sensing [55, 22, 60, 47]. Within the framework of image classification, a particularly successful used type of Machine Learning algorithms are Convolutional Neural Networks (CNNs). While CNNs have superseded many supervised classification approaches in terms of accuracy, CNNs typically fail to provide reliable and consistent uncertainty measures and network outputs have often been misinterpreted as probabilities [37, 17]. This has raised the question for better uncertainty estimates [24, 14].

Model uncertainty accounts for incomplete information, such as our inability to distinguish a mug from a cup on an image if the handle is invisible [44]. Model uncertainty is also crucial for detecting objects belonging to a new class which was never seen in the training set. A typical application of ML methods in medical imaging is disease detection, in which ML methods can perform some of the tasks usually done by human experts [27]. In such applications, it is not only crucial to determine the diseases with high accuracy, but also to provide a measure of certainty. This is where current ML methods typically fall short of human experts, who can accurately assess their certainty and consult more colleagues if needed [27].

In remote sensing, relevant applications of uncertainty measures include tasks related to land cover classification and change detection after natural disasters. In Active Learning, model performance can be improved by asking the user to provide labels for the most uncertain pixels of an image [35,

58, 41, 52, 53]. For change detection, it would be desirable to have a reliable confidence measure providing high confidence values for correctly predicted changes in order to avoid false alarms.

Uncertainty estimation has become a crucial and open field of research and many different approaches to account for uncertainty have been put forward [14, 9, 24, 49, 27, 50]. The sources of uncertainty have traditionally been classified in two parts: epistemic uncertainty, accounting for model uncertainty which can be reduced by adding more training samples, and aleatoric uncertainty, representing intrinsic noise in the data, which cannot be reduced by additional training samples [24]. Sources of uncertainty have been attributed to noise, outliers and errors in the input data and model uncertainty. Model uncertainty can be split into uncertainty in model parameters that explain best the observed data, and structural uncertainty, accounting for the decision which model structure should be used [18, 14].

Contrary to probabilistic classification models, many current ML models do not provide a direct measure of confidence. Thus, many authors have proposed new network structures that are either probabilistic or that show better robustness to data transformation and fooling attempts. An example of probabilistic network architectures are Bayesian Neural Networks (BNNs), which provide a direct measure of confidence by optimizing over distributions rather than single-valued weights [14, 24].

Rather than changing the network architecture completely, some authors have proposed approaches to measure confidence by applying minor changes to existing networks, such as adding a special meta-loss function to maximize class distances between activations [31] or training a confidence detector on top of a network [2]. A different set of methods model uncertainty by working with the direct outputs of the network, which can either be network activations of intermediate network layers or of the final network layer.

In classification, a common pitfall is to interpret the network's output activation as probabilities. Some shortcoming of using the softmax activations as a confidence measure are explained in section 2. Yet, these methods have the advantage that they don't require a change in the network architecture and are applicable to many different standard network types.

Most of these confidence methods are either evaluated with respect to error detection, which can be seen as a binary classification of identifying each class prediction as correct of incorrect, or to novelty detection, where the confidence score is used to assess whether a point from the test set belongs to a class not yet seen in the training set [31, 36]. Typically, a confidence measure should give a low value to a false prediction in error detection, and a low value to unseen classes in novelty detection.

This study presents a density-based clustering approach for uncertainty estimation within the framework of image classification, using the activations of the pre-softmax layer in a CNN. These activations are retrieved during test time and are clustered using an ensemble of Density Trees, called Density Forests (DFs), following the method proposed by Criminisi et al. [10]. Similar to Random Forests (RFs), which use many Decision Trees to separate labelled data, Density Forest separate unlabelled data using several Density Trees. An Information Gain (IG) function is used to determine the best split at each tree node by maximizing the Gaussianity of the two resulting splits. Unlike Decision Trees, the goal of Density Trees is not to predict a label but to best partition the data into Gaussian-like clusters. To predict the probability of each sample to belong to a seen class, each Density Tree in a Forest is descended and the Gaussian Probability Density Function (PDF)

to belong to the leaf node is calculated.

The objectives of this study are the following:

1. To implement Density Forests and evaluate them with respect to novelty detection, using pre-softmax CNN activations;
2. To compare Density Forests to other novelty detection methods using pre-softmax activations as well as baselines using softmax activations;
3. To study the potential of these novelty detection methods both for the case of patch classification and semantic segmentation.

The Density Forest confidence measure is compared to other, standard novelty detection methods as well as to baseline confidence measures for CNNs. The main requirement for all tested methods is that they do not need any changes in the network architecture: they all have to work directly with the activations of either the final or intermediate network layers.

The performance of the Density Forest algorithm is evaluated both with respect to patch classification in the MNIST dataset and with respect to semantic segmentation of the "Zurich Summer Dataset v1.0" (Zurich) dataset, using networks trained on $N - 1$ of the available classes and predicting on all classes [26, 54]. Receiver Operating Characteristic (ROC) curves are used to evaluate each novelty detection measure.

2 Literature Review

The shortcomings of standard deep learning tools in capturing model uncertainty have been pointed out by many authors, such as Gal and Ghahramani [16], Nguyen et al. [37], and Mandelbaum and Weinshall [31]. As Subramanya et al. [49] show, the notions of confidence and accuracy are related: a model with high accuracy should ideally give high confidence values to its predictions on average, as otherwise the model would suggest high confidence for incorrect predictions.

Confidence scores for ML methods are typically evaluated either in *error detection*, which aims at identifying each class prediction as correct or incorrect, or in *novelty detection*, consisting of identifying labels different from the classes seen during training. Both error detection and novelty detection can be seen as binary classification tasks, with the aim of attributing a binary label (-1 / 1) to each class according to whether the label is likely to be wrong, in error detection, or according to whether it belongs to one of the seen classes in the training set, in novelty detection [2, 31]. Although most confidence methods either focus either on error detection or novelty detection, some methods are applied to both [50, 2, 31].

Novelty detection is an important field of research in Machine Learning and has been subject of numerous literature reviews [4, 32, 33, 40, 36]. Novelty detection is described as the task of classifying test data that differ from the data available during training [40]. This can been seen as "one-class classification", in which a model is trained to model the "normal" distribution, hoping that data following an "abnormal" distribution will be recognized as being different. Related topics are *anomaly detection* and *outlier detection*, which usually require the novelties to be few and different from the samples of the seen classes [36, 40].

Typologies of uncertainty heuristics have been made in categories such as "white box" methods, requiring changes in the model architecture to fit the purpose of detecting confidence, "gray box" methods, which require only some degree of re-training, and "black-box" methods, in which the confidence is based on the softmax output of the trained network and no re-training is needed [2]. This general scheme fits well into the framework of the developed methodology, which mainly focuses on methods requiring little changes to the network structure.

The following literature review tackles some of the most prominent confidence measures with respect to both error detection and novelty detection. A selection of these methods will be tested with respect to their performance in novelty detection and compared to Density Forests. Since many of the presented confidence measures as well as Density Forests are applied to novelty detection, some popular novelty detection methods are also briefly addressed.

The following notation is based on [10]. Vectors are denoted in bold ($\mathbf{v}$), matrices in telescope uppercase letters ($\mathtt{M}$) and sets using calligraphic notation ($\mathcal{S}$). Furthermore, following notation is used for classes and membership probabilities:

$$\mathcal{L} = \{c_i\}_{1 \leq i \leq n_c} \qquad \text{Set of classes} \tag{1}$$

$$P^{(c)}(\mathbf{x}) = P(\mathbf{x} \in c) \qquad \text{Membership probability of a sample } \mathbf{x} \text{ to class } c \tag{2}$$

There are many overviews on neural networks architectures and building blocks available, therefore, they are only covered very briefly in the following literature review [45, 60, 23].

2.1 Methods Based on Network Output

2.1.1 Single-Pass Methods

A first set of methods look at the simple network outputs of a single pass of the data through the network, typically a softmax activation in image classification. The simplest possible baseline consists of considering the Maximum Softmax Response (MSR) as a confidence indicator [19, 59]:

$$C_1(\mathbf{x}) = P^{(c_1)}(\mathbf{x}) \tag{3}$$

where $\mathbf{x}$ is a data point and $c_1 = \text{argmax}_{c \in \mathcal{L}} P^{(c)}(\mathbf{x})$.

A similar approach takes into account the two highest network outputs and calculates a confidence score based on the margin between the two [38, 31]:

$$C(\mathbf{x}) = P^{(c_1)}(\mathbf{x}) - P^{(c_2)}(\mathbf{x}) \tag{4}$$

where $c_1 = \text{argmax}_{c \in \mathcal{L}} P^{(c)}(\mathbf{x})$ and $c_2 = \text{argmax}_{c \in \mathcal{L} \setminus c_1} P^{(c)}(\mathbf{x})$.

The negative entropy of all normalized softmax activations can be used to take into account all output activations [59]:

$$C_2(\mathbf{x}) = -H(\mathbf{P}(\mathbf{x})) = \sum_{c \in \mathcal{L}} P^{(c)}(\mathbf{x}) \log P^{(c)}(\mathbf{x}) \tag{5}$$

where $\mathbf{P}(\mathbf{x})$ denotes the network output activation vector for a data point $\mathbf{x}$ and H denotes the entropy function. The entropy is zero if all activations but one are zero and it is minimal when all activations are equally probable.

Many further, similar measures have been developed using the final network output scores to predict uncertainty, such as Sun and Lampert [50], proposing the use of network activations to predict out-of-order behaviour of a network, by applying a Kolmogorov-Smirnov (KS) test to the distribution of the softmax activation values.

2.1.2 Invariance to Image Transformations

In contrast to the baseline methods explained above which rely on using the softmax output scores of a single pass through the network, Bahat and Shakhnarovich [2] use a more sophisticated approach which relies on multiple softmax outputs of transformed input data (fig. 1). In the case of an image classifier, a test image is transformed multiple times before prediction, for instance by applying contrast enhancements, blurring the image, applying a gamma filter or by flipping and rotating the image. The assumption is that a classifier will react differently to transformations of correctly and incorrectly classified data points, being more invariant to transformations of correctly classified input. Softmax activations are retrieved for the original image as well as for each transformed image using the same model. All softmax scores are reordered in the rank of descending softmax response in the original image. The scores can be truncated such as to keep only the first n components in each softmax response, reducing the subsequent calculation time. All reordered and truncated softmax scores are then concatenated and used as a training set for a Multi-Layer Perceptron (MLP), a simple Neural Network structure, which calculates the probability of the network to make a wrong prediction.

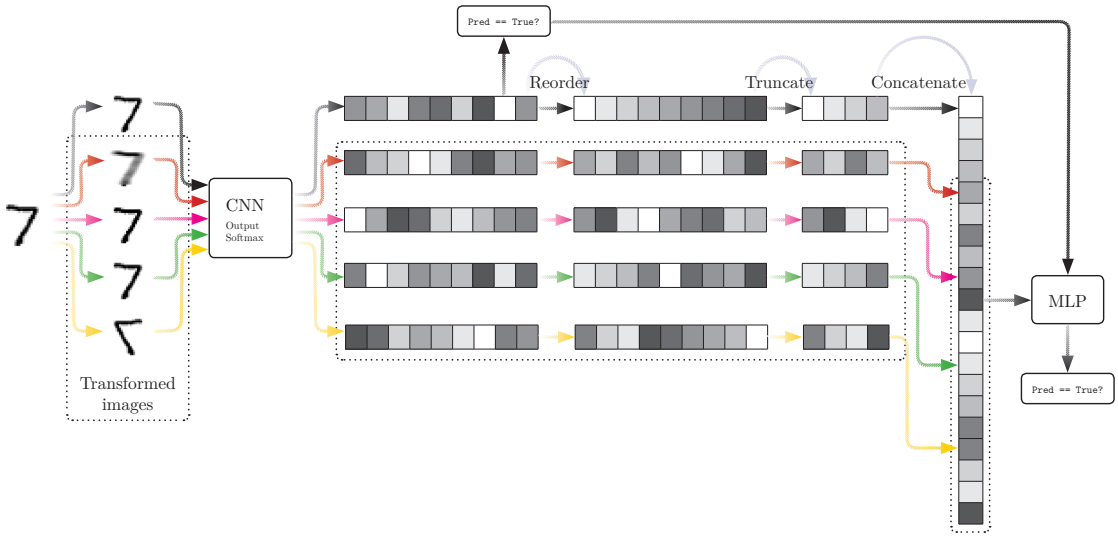

Figure 1: Invariance To Image Transformation: Schema for MNIST digit example [2].

This approach requires training an MLP on top of an existing network to assess uncertainty, which can however be done efficiently and in time linear in the number of image transformations. They also propose a slightly more complex version of their algorithm for novelty detection [2].

2.1.3 MC-Dropout

Gal and Ghahramani [16] propose the use of Monte-Carlo Dropout (MC-Dropout) during prediction to quantify the model uncertainty. In order for MC-Dropout to work the neural network has to be trained with dropout applied after every convolution layer. Then, in order to retrieve the uncertainty $C(\mathbf{x})$ for a data point $\mathbf{x}$, T stochastic forward passes through the network are performed, each time randomly dropping a certain number of weights using test-time dropout, thus only using a subset of all available weights for the prediction. The predictions are calculated as the average output of all T runs and the certainty as the mean variance of the softmax outputs. This method has been used as a de-facto uncertainty measure for neural networks in many papers [31, 27, 25, 49, 23].

2.2 Methods Based on Network Activations

As Gal and Ghahramani [16] point out, a model can be very uncertain about its predictions despite yielding a high softmax output. Nguyen et al. [37] demonstrate that neural networks can be easily fooled using an algorithm that generates images unrecognizable to humans but creating almost-100 per cent certainty predictions by the softmax activation output of the network. In addition, Goodfellow et al. [17] have shown that an adversary network can induce minor perturbations into an image which create false predictions with very high confidence. Thus, many authors have decided to model the density of the network's pre-softmax activations of the training set for error detection and novelty detection tasks [49, 31, 4].

Subramanya et al. [49] point out that softmax scores can vary drastically when applying transformations such as Gaussian noise, blurring or JPEG compression to an image. In order to provide a more robust confidence estimator, they propose to model the density over each seen class in the pre-softmax activations: In order to estimate the confidence score of a prediction, they calculate the Gaussian densities belonging to the activations of the N classes in a classification problem. Their confidence estimate yields more robust to image transformations such as noise injection and JPEG compression, but may suffer in case of Gaussian blurring and adversarial training.

Mandelbaum and Weinshall [31] have opted for a similar approach, however approximating local density by the Euclidean distance between a point and its k-Nearest Neighbors (k-NN) in the embedded space created by the network in one of its pre-softmax layers. During test time, their method retrieves the activations of each data point and computes the distance to the k nearest neighbors of each sample. In order to provide reasonable uncertainty estimates, this method requires either adversarial training or a special loss function in which the distance between pairs of adjacent points belonging to different classes is maximized. Without this special loss function, their method yields worse or similar results compared to the baselines max margin and entropy [31]. Using a modern GPU implementation of nearest neighbor search, they achieve a computational complexity of $O(kN)$, k being the number of nearest neighbors to search and N the number of data points, making their method scale well with big datasets.

2.3 Network Architectures for Confidence Estimation

The current state-of-the art method to estimate uncertainty in ML is based on BNNs, allowing for direct estimation of the uncertainty from the model probabilities [15, 16, 24]. However, this approach requires the network to be a Bayesian network, which implies changes such as optimizing over weight distributions instead of fixed weights. However, in Gal and Ghahramani [15, 16], the authors demonstrate the equivalence between a BNN and a standard MLP with dropout applied after every weight layer during test time (MC-Dropout) with respect to confidence estimation.

Goodfellow et al. [17] show that adversarial examples can be used to improve the resistance of the network against *fooling* attempts (sec. 2.2), using *Adversarial Training*. This however comes at a high price in computational cost at up to twice the training time [31].

Further methods have been developed based on *ensembles* of NN models, such as in Lakshminarayanan et al. [25] and Mandelbaum and Weinshall [31]. These methods however suffer from heavily increased computation complexity for training several models.

2.4 Comparison to Novelty Detection Methods

Many more novelty detection methods have been developed to model the support of data belonging to the "normal" class versus new "anormal" data [40, 32, 33]. They have been mainly characterized as probabilistic, distance-based, reconstruction-based and domain-based detection. Since not all methods could be implemented and evaluated, only a subset of the most popular novelty detection are covered.

Two of the most common novelty detection methods are presented in this paper. The first are Gaussian Mixture Modelss (GMMs), in which the assumption is made that the data was generated by an underlying mixture of Gaussian distributions [42]. GMM work by defining a pre-defined number of Gaussian distributions with random mean and covariance parameters, then fitting them iteratively to the training data via the Expectation-Maximization (EM) algorithm [11]. Some applications of GMMs to novelty detection are presented in [40]. The second are One-Class Support Vector Machiness (OC-SVMs), in which the support boundary is searched for a given set of training points [56, 3]. Support Vector Machines (SVMs) try to find a linear hyperplane using a kernel function, which can represent similarities between pairs of data points in an abstract geometric space [51].

A difference between anomaly detection and novelty detection is that anomaly detection usually assumes novelties to be rare [36]. Some of the methods for anomaly detection include Isolation Forests (IFs) and Local Outlier Factor (LOF) [40, 7, 29]. In contrast, GMM and DF can be seen as a clustering method, which require sufficient novelties to be available.

2.5 Summary

A summary of the reviewed literature and methods for confidence estimation in neural networks is given in table 1. Since the existing body of research on Confidence Estimation is vast and many related papers exist to each of the presented topics, only a selection of reviewed papers is presented.

Type	Reference	Method	Focus
Softmax scores	Hendrycks and Gimpel [19]	**MSR, Margin, Entropy**	Softmax activations
	Bahat and Shakhnarovich [2]	*Tranformations Invariance*	Data Perturbations
	Gal and Ghahramani [16]	**MC-Dropout**	Model Perturbations
	Sun and Lampert [50]	KS-Test	KS-test on softmax output
Pre-softmax activations	Subramanya et al. [49]	*Density*	Density Modelling
	Mandelbaum and Weinshall [31]	*Distance*	k-NN Distance
New Network Architectures	Goodfellow et al. [17]	*Adversarial Training*	Training Perturbations
	Kendall and Gal [24]	*BNNs*	Bayesian Neural Networks
	Mandelbaum and Weinshall [31]	*Ensembles*	Neural Network Ensembles

Table 1: Summary of reviewed confidence measures for neural networks. Implemented baselines are indicated in bold.

3 Methodology

3.1 Overview: Density Forests

Similar to the activations-based methods presented in section 2.2, the confidence measure developed below tries to distinguish activations of the training set from new, unseen activations in the test set. Similar to the way Decision Trees and Random Forests are used in the case of labelled data, Density Trees and Density Forests are used for unlabelled data to distinguish "normal", seen data from unseen, new data points.

The methodology proposed below is based on previous work by Criminisi et al. [10], who propose a unified framework for random decision forests, which can be extended to classification, regression, density estimation and other tasks. Therefore, this unifying framework of decision forests is first addressed before covering the extension to Density Forests.

An overview of the methodology for novelty detection using Density Forests is shown in figure 2.

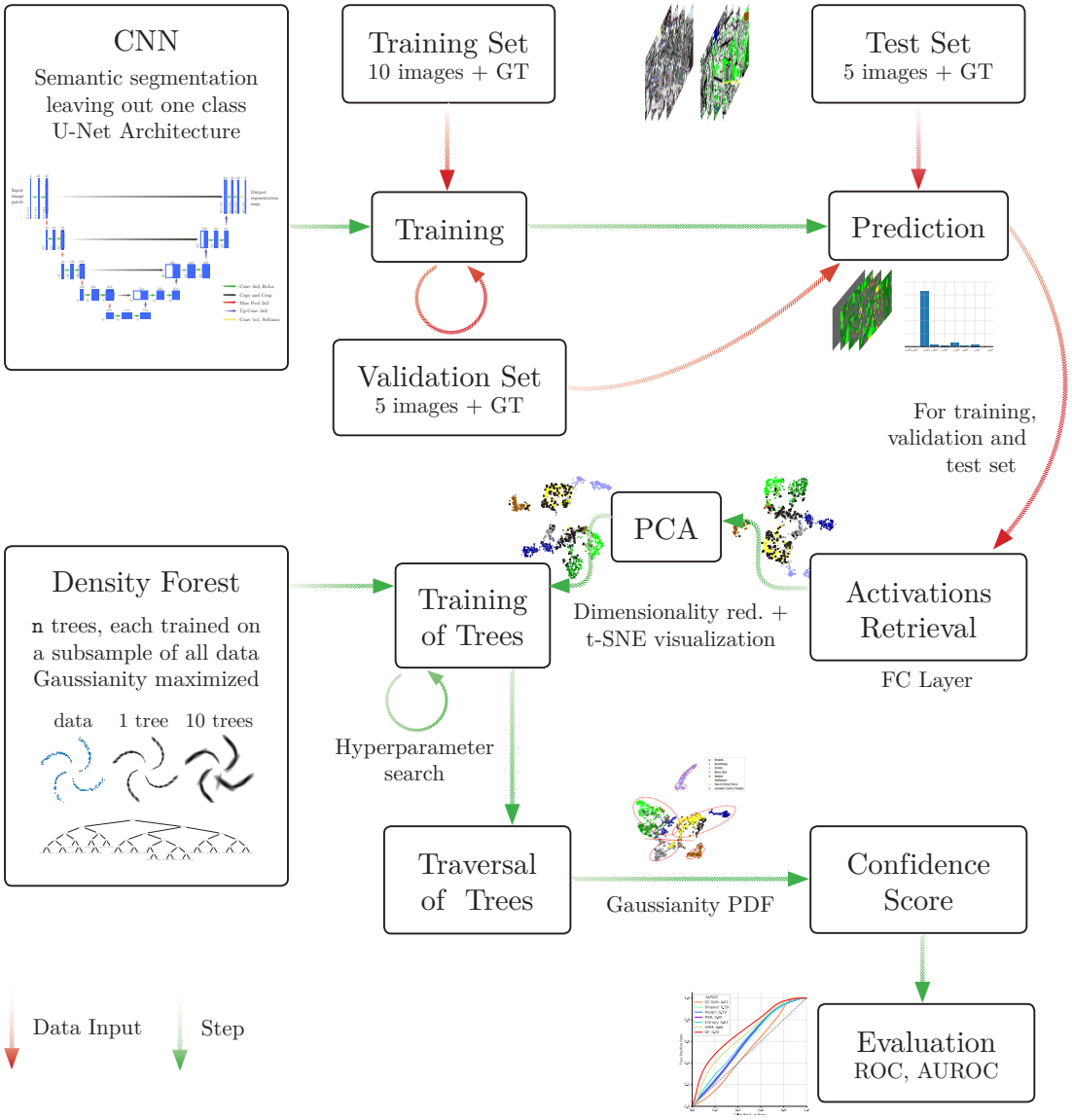

Figure 2: Workflow Diagram

3.2 Decision Trees

A Decision Tree is a binary tree consisting of hierarchical nodes and edges which, at each level, provide the most important features to determine the outcome of a dependent variable, given an arbitrary number of independent variables [10]. Using an entropy function $H(S)$, the goal of a Decision Tree is to find the best possible split to partition the feature space S at each level starting

from top to bottom such as to maximize an Information Gain function:

$$I = H(\mathcal{S}) - \sum_{i \in \{l,r\}} \frac{|\mathcal{S}_i|}{|\mathcal{S}|} H(\mathcal{S}_i) \tag{6}$$

Where I is the Information Gain, H is an optimizer or entropy function, S is the original dataset at a node and S_i is left and right data subset resulting from the split.

For instance, in the case of labelled data and decision forests, the Shannon entropy is often used:

$$H(\mathcal{S}) = -\sum_{c \in \mathcal{L}} P^{(c)}(\mathbf{x}) \log P^{(c)}(\mathbf{x}) \tag{7}$$

$P^{(c)}(\mathbf{x})$ being the probability of an outcome c for a discrete random variable $\mathbf{x}$ with possible outcomes $\mathcal{L}$. Within each dimension, a range of possible split values is checked to find the split which minimizes entropy, i.e., maximizing information gain. For each candidate split dimension, a number of candidate split values have been tested randomly between the interval of the *dim*-th smallest and *dim*-th largest data point values, such as to ensure at least *dim* datapoints to either side of the split to ensure invertible matrices.

Stopping criteria for growing individual tree branches have been implemented according to [10], based on maximum maximum tree depth and based on the minimum Information Gain required at each node to continue splitting. The implemented data structure of a Decision Tree node is represented in appendix A.

3.3 Random Forests

Smoother and more generalized boundaries can be obtained by using Random Forests, which combine a set of individually trained trees on bootstrapped subsamples of the initial data [10, 6]. Bootstrapping is a technique of sampling a smaller subset of data from a larger subset with replacement [61]. The aggregation of multiple predictors based on bootstrapped samples is usually referred to as bagging [5]. A simple visualization of Random Forests on generated synthetic data is provided in appendix B. Aside of the parameters and stopping criteria mentioned for individual trees, important factors for Random Forests are the number of trees, the subsample size of the initial data on which each tree is trained and the number of dimensions each node may consider as a candidate dimension for splitting.

3.4 Density Forests

A Density Tree can be seen as similar to Decision Trees, but with the aim of clustering *unlabelled* data into regions that maximize the Gaussianity of each cluster [57]. Same as with Decision Trees, a generic information gain function is maximized (eq. 6). An unsupervised entropy function is designed based on the assumption of a multivariate Gaussian distribution at each tree node [10]:

$$H(\mathcal{S}) = \frac{1}{2} \log \Big((2\pi e)^d |\Lambda(\mathcal{S})| \Big) \tag{8}$$

Λ being the associated $d \times d$ covariance matrix. Hence, the information gain at the j^{th} split becomes [10]:

$$I_j = \log(|\Lambda(\mathcal{S}_j)|) - \sum_{i \in \{l,r\}} \frac{|\mathcal{S}_j^i|}{|\mathcal{S}_j|} \log(|\Lambda(\mathcal{S}_j)|) \tag{9}$$

For a description of the motivation behind this optimization method, refer to [10]. The implemented data structure for Density Trees is represented in in appendix A.

At prediction time, a given data point descends the Density Tree according to the split dimension and value associated with each tree node until it reaches a leaf node. The probability of the data point to belong to a cluster of the tree is calculated with respect the leaf node cluster [10]:

$$p_t(\mathbf{x}) = \pi_l \mathcal{N}(\mathbf{x} | \boldsymbol{\mu}_{l(\mathbf{x})}, \Lambda_{l(\mathbf{x})}) \tag{10}$$

With $\boldsymbol{\mu}_{l(\mathbf{x})}$ and $\Lambda_{l(\mathbf{x})}$ denoting the mean and covariance of the leaf node corresponding to the data point $\mathbf{x}$, π_l being the proportion of points falling into the respective leaf node. The multivariate Gaussian PDF is defined as follows:

$$\mathcal{N}(\mathbf{x} | \boldsymbol{\mu}, \Lambda) = \frac{1}{\sqrt{(2\pi)^k \det \Lambda}} \exp\left(-\frac{1}{2}(\mathbf{x} - \boldsymbol{\mu})^\top \Lambda^{-1} (\mathbf{x} - \boldsymbol{\mu})\right) \tag{11}$$

Where $\boldsymbol{\mu}$ is the mean, Λ is the co-variance matrix and k is the number of dimensions of $\mathbf{x}$ [46]. The thus obtained probability is weighted by the percentage π_l of all the data used for training the Density Tree falling into this leaf node. For the purpose of this study, no probability normalization term has been implemented, as we are only interested in relative confidence values between classes. Figure 3 illustrates the splitting steps for a single Density Tree.

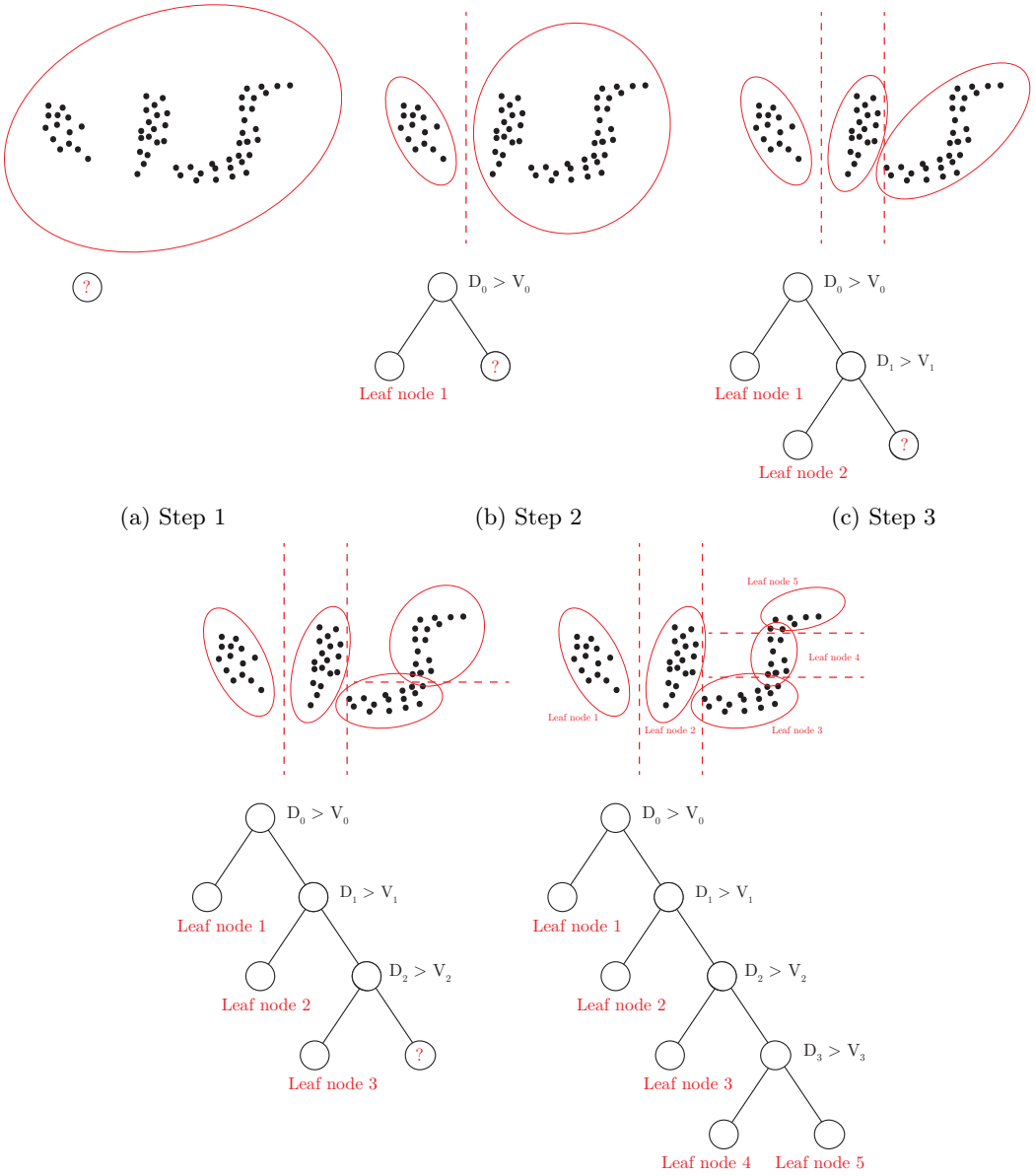

(a) Step 1 (b) Step 2 (c) Step 3

(d) Step 4 (e) Step 5

Figure 3: Illustration of tree growth for a fictive dataset. Covariance ellipses are indicated in red lines and splitting lines in red dotted lines, indicating the dimension and value along which a node is split. D_i and V_i denote the split dimension and value of the i-th split. Nodes are considered leaf nodes when no further split is necessary or possible, either because the Information Gain of a new split would lower than a defined threshold or because the maximum tree depth is reached. In a Density Forest, every tree would see a subset of all points and fit slightly different leaf nodes each time.

At every step of the Density Tree creation, splits are created such as to maximize the Gaussianity on either side of the node. The maximum number of splits can either be based on an Information Gain criterion or maximum tree depth. Parameters for Density Forest are listed in table 2.

Parameter	Description	Parameter Range
`n_trees`	Number of trees to create. A higher number of trees increases training and prediction time by a linear amount.	20 - 50
`subsample_pct`	Size of each random data subset sampled from the original dataset used as input for a Density Tree, in percentage of the size of the original dataset	(0, 1)
`max_depth`	Maximum depth allowed for each tree. Improves generalization ability of individual trees.	1 - 5
`min_subset`	Minimum subset of each data to be contained in each cluster, as percentage of the subsample dataset size.	2 - 3 $\times$ `dim`
`n_max_dim`	Number of dimensions to consider for splitting at each node. If `dim` ≤ 0, all dimensions are considered. If `dim` > 0, a random number of dimensions between 1 and dim is considered for splitting at each node. Increases speed and further adds randomization to trees.	[0, `dim`)
`ig_improvement`	The Information Gain improvement that has to be made at each node in order to create a new split. Avoids unnecessary splits in already Gaussian-like clusters	(0, 0.9)

Table 2: Density Forest parameters and suggested parameter ranges

4 Datasets

4.1 Synthetic Datasets

First, some synthetic data were produced to test how well individual Density Trees could fit points generated in 2-dimensional space, and visualize the decision boundaries. The following three data generators have been implemented:

1. A generator which produces n clusters according to Gaussian distributions $\mathcal{N}(\mathbf{x}|\boldsymbol{\mu}, \Lambda)$ with fixed parameters $\boldsymbol{\mu}, \Lambda$. The mean μ is chosen between a defined minimum and maximum value in each dimension and the covariance Λ is For each cluster, the covariance matrices Λ can be randomly multiplied by a coefficient in one dimension, such as to create an elongated cluster, and non-linear transformations to make the cluster less Gaussian-like can be applied.

2. A spiral data generator, which produces points along a spiral, with the points x and y being generated as:

$$\begin{aligned} x &= a\sqrt{\theta}\cos\theta \\ y &= a\sqrt{\theta}\sin\theta \end{aligned} \tag{12}$$

θ being the angle and a being the distance between successive terms of the spiral.

3. A generator which produces data along an S shape similar to the method above, but with only one arm, generating data points as follows:

$$\begin{aligned} x &= a\sqrt{\theta}\sin\theta \\ y &= xa\sqrt{\theta}\sin\theta \end{aligned} \tag{13}$$

Datasets generated according to these three data generators are shown in figure 4.

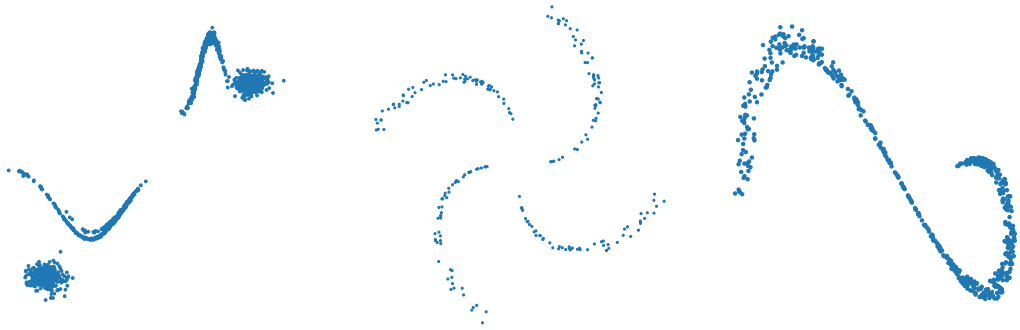

(a) 4 clusters with transformations

(b) Spiral with 4 arms

(c) S-shaped distribution

Figure 4: Synthetic datasets

4.2 MNIST Dataset

Confidence Measures have been first applied to the MNIST dataset, containing 24 × 24 gray level images of handwritten digits from 0 to 9 and corresponding labels [26]. The training set and test set consist of 60'000 and 10'000 samples respectively, with roughly the same amount of images for each class. Some examples of handwritten digits are shown in figure 5.

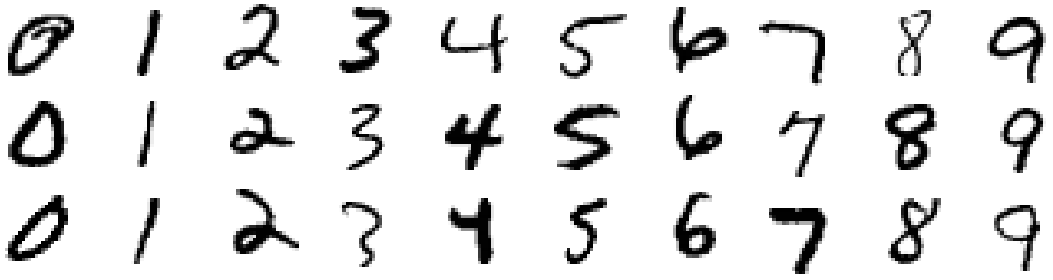

Figure 5: Sample images of the MNIST dataset for true y labels 0 to 9 [26]

4.3 Zurich Dataset

In addition to confidence estimation on synthetic data and the MNIST dataset, the confidence measures were applied to semantic segmentation, which consists of attributing a class label to every pixel of an image [55]. For this task, the "Zurich Summer v1.0" (Zurich) dataset was used, consisting of a set of 20 RGB-IR satellite images taken from a QuickBird acquisition of the city of Zurich (Switzerland) in August 2002, together with a corresponding set of annotated ground truth images [54]. 8 different urban and peri-urban cases have been annotated: Roads, Buildings, Trees, Grass, Bare Soil, Water, Railways and Swimming Pools. The Zurich dataset was split into a training set consisting of images 1-10, a validation set consisting of images 11-15 and a test set consisting of images 16-20, corresponding roughly to a 50/25/25 split. An example pair of an RGB-IR image and its ground truth is given in fig. 6.

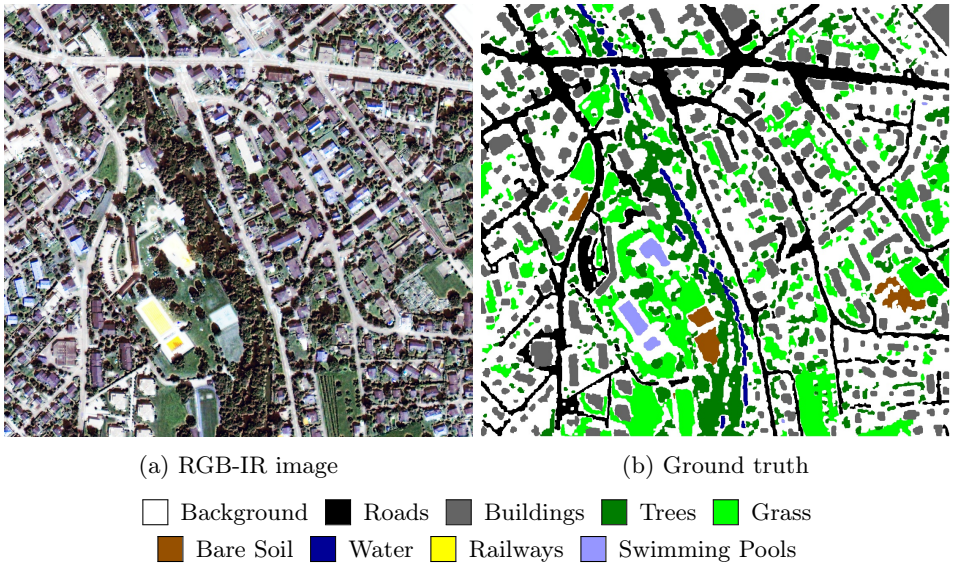

Figure 6: Sample pair of images and ground truth for the Zurich dataset [54]

Classes are imbalanced, with only very few samples for some classes, such as swimming pools or railways (fig. 7).

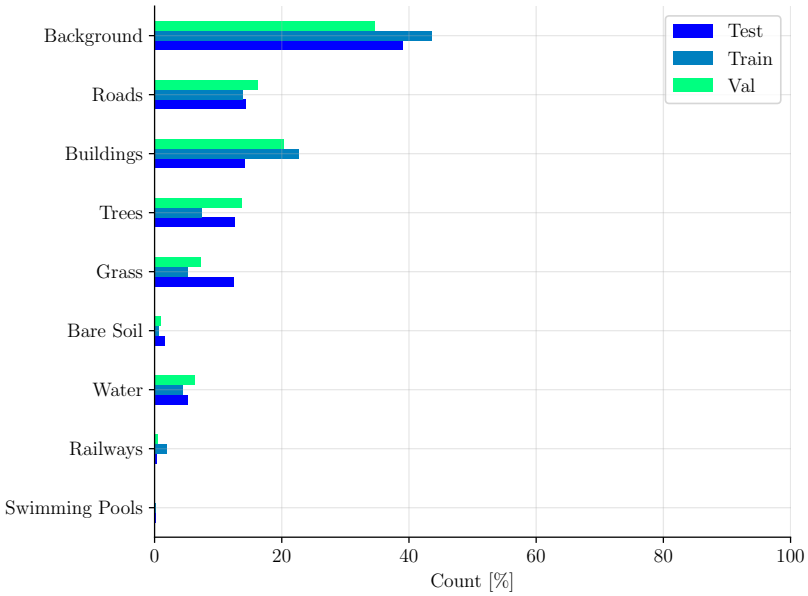

Figure 7: Label distribution in the Zurich dataset

5 Experimental Setup

5.1 Network Architectures

MNIST dataset The MNIST dataset consists of a training set of 60'000 images and a test set of 10'000 images, both containing a roughly equal amount of images belonging to the labels 0-9 [26]. 10 CNN models were each trained on about 54'000 training images, removing images of the left-out class, and validated on 10'000 test images, including images of the left-out class.

CNNs were trained both for novelty detection using the network architecture described in table 3. For novelty detection, CNNs have been trained leaving out each time one class. Dropout was added after each MaxPooling layer to increase the redundancy of the network and avoid overfitting [48]. The Rectified Linear Unit (ReLU) activation function ($f(x) = \max(0, x)$) was used after each convolution layer of the network. The Fully Connected (FC) layer denotes the pre-classification layer in the network, in which every input is connected to every output by a weight and followed by a ReLU activation.

Layer	Properties
Input	Dimension $\|b\| \times 28 \times 28$
Convolution + ReLU	32 3×3 filters
Convolution + ReLU	64 3×3 filters
MaxPooling	2×2 pool size
Dropout	$p = 0.25$
Flatten	
Dense (FC) + ReLU	128 neurons
Dropout	$p = 0.5$
Output + Softmax	9 neurons

Table 3: Architecture of the CNN used for MNIST digit classification. $|b|$ = batch size, p = dropout probability.

Zurich dataset Similar as for the MNIST dataset, CNN models were trained for each left-out class. The U-Net network architecture shown in figure 8 was applied to perform semantic segmentation on the Zurich dataset. It consists of a sequence of down-sampling and up-sampling layers, yielding a "U"-shaped layer architecture [43]. This architecture has shown good performance in various semantic segmentation tasks, and has been especially applied in medical imaging [43, 1, 13]. A full overview of the layers is given in appendix table E.1.

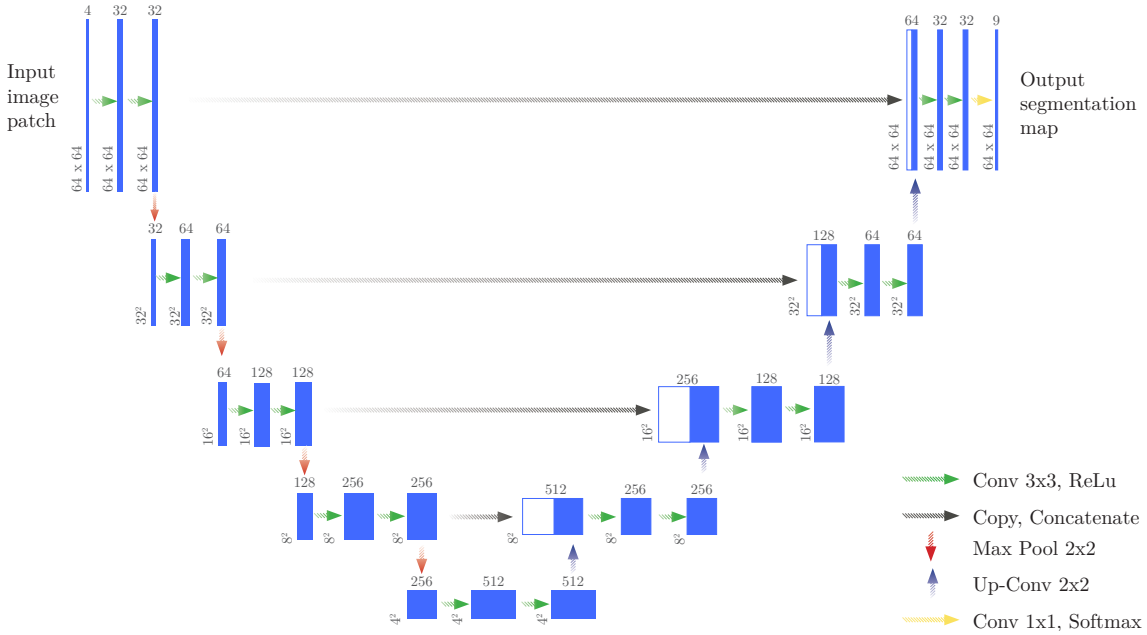

Figure 8: U-Net architecture, according to Ronneberger et al. [43]. Numbers on top of each blue block indicate the number of filters, numbers on the bottom left of the blocks indicate the resolution of each filter.

Image Tiling For training the U-Net model, the training and validation images were tiled into *non-overlapping* patches of patch size size $64 \times 64 \times n_c$ where n_c is the number of channels. For prediction, the test set images were tiled into *overlapping* patches using the same patch size of $64 \times 64 \times n_c$, with several different strides between patches, keeping only the central overlapping *stride* $\times$ *stride* pixels between adjacent patches. Central pixels of a patch are assumed more certain because of the larger available spatial context in the patch compared to pixels near the patch borders which partially lack neighbor information, leading to strong border effects [34]. Although the optimal stride would seem to be 1, keeping only the central pixel would lead to excessive computational costs with little additional accuracy gain. Therefore, intermediate strides have to be chosen empirically. Since only the central part of each patch is kept, the original images first had to be padded in order to avoid cropping. For a given stride and patch size, the image was first padded on each side to make it divisible by the amount of overlapping pixels, and by an additional amount *(patch size - stride) / 2* on either side of the image to be able to fit patches of size 64×64 with the given stride around the entire padded image. For each patch, only the *stride* $\times$ *stride* central pixels were kept and any remaining pad was removed from the image to give it the same dimensions as the input image. Several strides were chosen and results averaged to further reduce border effects. For instance, for a stride of 32 pixels and a patch size of 64 pixels, patches of $64 \times 64 \times n_c$ are created and only the $32 \times 32 \times n_c$ central pixels are kept for the final prediction.

Data Augmentation Data augmentation was performed to improve the accuracy of the network. Following transformations have been applied both to the image and ground truth patches, according to Volpi and Tuia [55]:

1. Extraction of patches at random locations of the training set images to avoid seeing the same types of patches in each training minibatch. Class imbalance is not considered during patch extraction.
2. Random horizontal and vertical flipping and random rotations in steps of 90 degrees (0, 90, 180 or 270 degrees). These transformations aim at improving invariance to differing spatial organizations of the image.
3. Noise injection: Add noise to every pixel of the image, sampling the noise from a Normal distribution in $\mathcal{N}(0, 0.01)$ with subsequent rescaling of the data values between $[0, 1]$

5.2 Novelty Detection Baselines

Some implementation details are discussed below for other novelty detection baselines to which Density Forests are compared.

MSR, Margin, Entropy The confidence measures relying on the softmax output of a network which were implemented using the equations of section 2 (eq. 3, 4 and 5).

MC-Dropout In this study, a slightly simplified version of the MC-Dropout algorithm was implemented, performing dropout during test time only in the FC pre-softmax layer and calculating the entropy (eq. 5) on the mean of the softmax activations. This has the advantage of speeding up

calculations by having to repeat only the pass through the last layers of the network instead of the entire pass.

Pre-softmax methods In addition to the implemented baselines indicated in bold in table 1, Novelty Detection methods GMM and OC-SVM have been implemented to detect novelties using the network's pre-softmax activations. In this work, the GMM and OC-SVM approaches have been applied to novelty detection using the same activations as the Density Forest. Both GMM and OC-SVM model the "normal" data, consisting of activations of seen classes. As confidence values, GMM calculates the log-likelihood for a given a data point and OC-SVM calculates the signed distance from the separating hyperplane, being positive for inliers and negative for outliers. For both GMM and OC-SVM, the Scikit-learn implementations were used [39].

5.3 Dimensionality Reduction and Data Separability

For both the MNIST dataset and the Zurich dataset, activations of the fully connected layer were retrieved, resulting in a large number of input dimensions. For example, the FC layer of the MNIST dataset contains 128 filters, therefore, for a batch of n patches, the activation weights retrieved during prediction are of dimension $n \times 128$ (table 3). Many of these activations are similar, which causes collinearity and matrix inversion issues during the calculation of the Gaussian entropy. Therefore, a dimensionality reduction was performed using Principal Component Analysis (PCA). For MNIST, the 15 first components were kept, explaining about 70-80 % of the initial data variance (fig. 9). For the Zurich dataset, the first 5 dimensions were kept, explaining about 90-95 % of the data variance. The choice not to exceed 15 components for the MNIST set was made to limit the already high computation complexity for Gaussianity estimation. Another reason to prefer low-dimensional data is related to the curse of dimensionality, which causes notions of distance between points to become meaningless and which, together with data noise, negatively impacts performance of many clustering algorithms [20, 21].

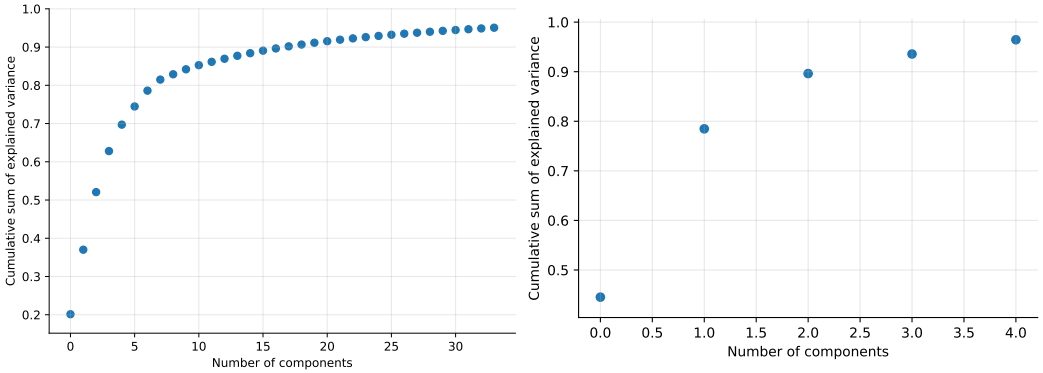

(a) MNIST dataset, left-out class 8

(b) Zurich dataset, left-out class roads

Figure 9: Explained variance as a function of the number of components

Separability between activations corresponding to different classes was ensured before and after PCA, using t-distributed Stochastic Neighbor Embedding (t-SNE) for visualization of high-dimensional data [30]. t-SNE tries to find a mapping between high-dimensional data points and their representation in a lower-dimensional space, typically in 2 to 3 dimensions, by preserving the local structure of the original, high-dimensional data (fig. 10). To preserve the original data structure, t-SNE models the pairwise similarity between data points in their high-dimensional and lower-dimensional space. Similarities between pairs of data points x_j and x_i are measured as the conditional probabilities of x_i choosing x_j as its neighbor, if neighbors were picked in proportion to their probability density of a Gaussian centered at x_i [30]. t-SNE uses a cost function to minimize the sum of Kullback-Leibler divergences over all data points, measuring the differences between similarity values in higher and lower dimensions. Since t-SNE directly transforms the training data without finding a parametric mapping, it can only be applied to the training data. This reduces the scalability of t-SNE due to increased training times.

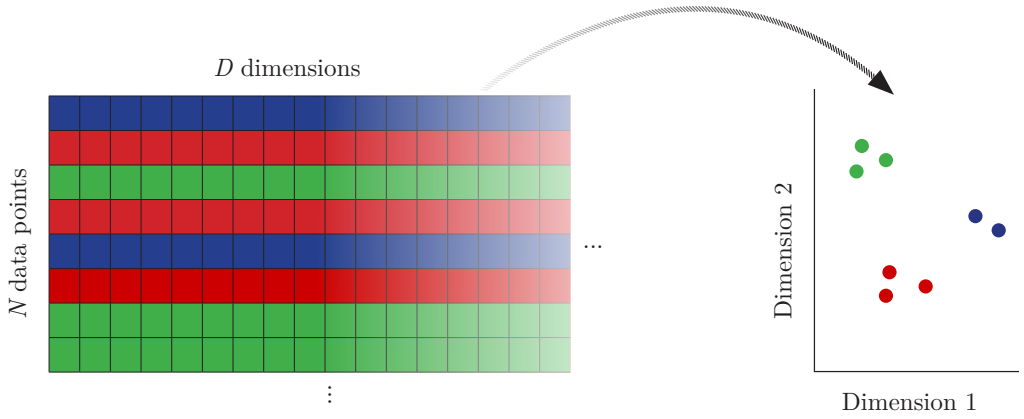

Figure 10: t-SNE schema with toy data. t-SNE finds a mapping between the original, high-dimensional data (left) and the data in a lower dimensionality (right). Classes of data points are shown in blue, red and green. If data points within the same class are more similar to each other in high-dimensional space, they will be closer to each other in the t-SNE visualization.

Density Forests were trained on the dimensionality-reduced activations belonging to one of the seen classes of the training set. To further improve performance, only activations of correctly predicted training points were used. Some activations of the seen classes might strongly differ from the other activations and be wrongly predicted, in which case they should be detected as novelties. The baselines GMM and OC-SVM both use the same dimensionality-reduced activations as the Density Forests for the hyperparameter search and for fitting the final model with the best found parameters. For all methods based on pre-softmax activations, hyperparameters are found using the scheme described in section 5.5. The same procedure was also applied to error detection, in which case the training set activations of correctly predicted points were used to fit the GMM, OC-SVM and Density Forest. These results are only presented in the appendix G.

5.4 Evaluation

For predictions from trained CNN models, accuracy metrics are indicated using Overall Accuracy (OA) and Average Accuracy (AA) as well as precision and recall, (table 4). For a given set of true class labels, precision measures the percentage of correctly predicted points, while recall measures the number of correctly predicted points over all points predicted as the class. While OA reports the percentage of all data points correctly classified, AA calculates the mean of the percentage of correctly classified data points per class.

		True labels y				PA
		1	2	...	r	
Predicted labels y	1	n_{11}	n_{12}	...	n_{1r}	$n_{11}/n_{1\bullet}$
	2	n_{21}	n_{22}	...	n_{2r}	$n_{22}/n_{2\bullet}$
	$\vdots$	$\vdots$	$\vdots$	$\ddots$	$\vdots$	$\vdots$
	r	n_{r1}	n_{r2}	...	n_{rr}	$n_{rr}/n_{r\bullet}$
UA		$n_{11}/n_{\bullet 1}$	$n_{22}/n_{\bullet 2}$	...	$n_{rr}/n_{\bullet r}$	OA= $\sum_i n_{ii}/n_{\bullet\bullet}$

Table 4: Confusion Matrix for classification problem with r classes. UA = User's Accuracy = Precision, PA = Producer's Accuracy = Recall, OA = Overall Accuracy, $1, 2, \ldots, r$=classes. n_{ij} counts the number of labels predicted as class i and belonging to the true class j. Bullet indexes signify either the sum of the row (e.g., $n_{O\bullet}$), the sum of the column (e.g., $n_{\bullet O}$) or the sum of all elements of the Confusion Matrix ($n_{\bullet\bullet}$).

Evaluation of the confidence measures is made according to the target of novelty detection: We are interested in a binary outcome, predicting whether a new point will belong to one of the seen classes or to an unseen class. All data points belonging to a seen class are attributed a value 0 and all data points belonging to an unseen class a value 1, meaning that they should be detected as different from the other data. In a binary classification setting, true positives are points correctly predicted as positive and true negatives are points correctly predicted as negative. Performance of the uncertainty measures is evaluated using ROC curves, which plot the true positives (TP) rate against the true negatives (TN) rate for varying confidence thresholds. The Area Under the Curve (AUC) is used to summarize the ROC curve (AUROC).

5.5 Hyperparameter Search

For the synthetic datasets, no hyperparameter search was performed since their only purpose is to show the behaviour of Density Forest splits visually. Density Trees and Density Forests were trained using the parameters listed in table 5. The same parameters have been used for each synthetic dataset.

Parameter	Value
`n_trees`	20
`subsample_pct`	.02
`max_depth`	5
`min_subset`	.02
`n_max_dim`	-1
`ig_improvement`	.5

Table 5: Density Forest parameters for each dataset

For the MNIST dataset and the Zurich dataset, best hyperparameters were searched for the novelty detection methods Density Forest, OC-SVM as well as GMM. The range of tried parameter combinations are listed in appendix H. For each candidate parameter combination, models were trained in parallel several times on a subset of the training set activations belonging to points of the seen classes being correctly classified and evaluated on a subset of all validation data (fig. 11)[1].

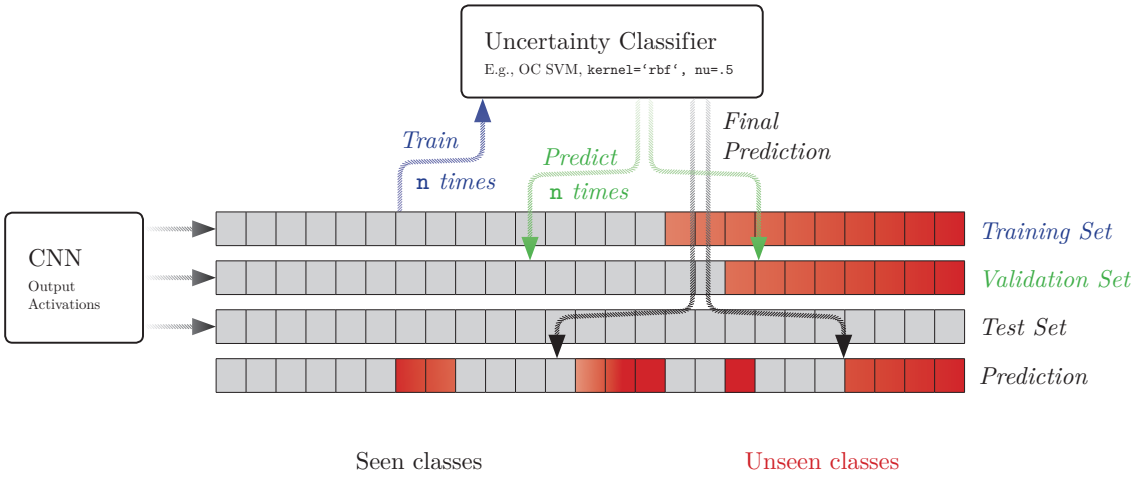

Figure 11: Parameter Search: Gray boxes show activations belonging to data points of seen classes, red boxes activations belonging to data points of the unseen class. In principle, the true class label is unknown for the test set. For each hyperparameter combination, the classifier is trained `n` times on a subset of the training set activations belonging only to seen classes (blue arrow) and evaluated on a subset of the seen and unseen points of the validation set (green arrows). The best hyperparameter combination found that way is applied to the entire test set (gray arrows), predicting for every point whether it belongs to a seen or unseen class.

Finally, the parameter set with the highest AUROC is applied to the test set. In addition to finding best hyperparameters, kernel spaces have been visualized for OC-SVM (fig. H.1 and H.2). Hyperparameter results and visualizations are shown in appendix H.

[1]For the class "swimming pools" of the Zurich dataset, hyperparameters were both trained and evaluated on the training set, since the there are no samples of the "swimming pools" class in the validation set.

6 Results

6.1 Experiments

In the following section, the experiments will be presented in the following order: In section 6.2, Density Forests will be illustrated by fitting individual Density Trees to the generated synthetic data, visualizing the effects of the Density Tree parameters on the number and shape of generated clusters. In section 6.3, Density Forests as well as the baseline confidence measures explained in section 2 will be applied to the MNIST dataset, and their performance will be compared with regards to novelty detection. In section 6.4, Density Forests as well as the baseline confidence measures will be applied to the Zurich dataset, again measuring performance with respect to novelty detection and highlighting in addition some objects with low confidence values.

6.2 Synthetic Data

Figure 12 shows points of the synthetic dataset generated according to the data generator described in section 4.1 and covariance ellipses of an individual Density Tree trained on all data using the parameters listed in table 5.

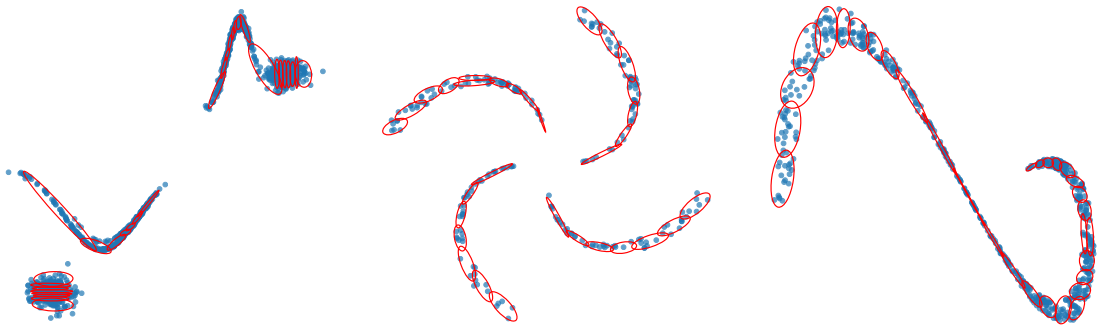

(a) Dataset 1 (b) Dataset 2 (c) Dataset 3

Figure 12: Covariance ellipses of individual Density Tree (subset of all points shown)

Figure 13 shows the covariance ellipses of the splits found at each depth of a Density Tree used to fit dataset 2. With deeper levels of the tree, more splits are created, but only in regions of the spiral arms with fewer points. It seems that in these regions, since there are less points, more ellipses are necessary to fit the local distribution.

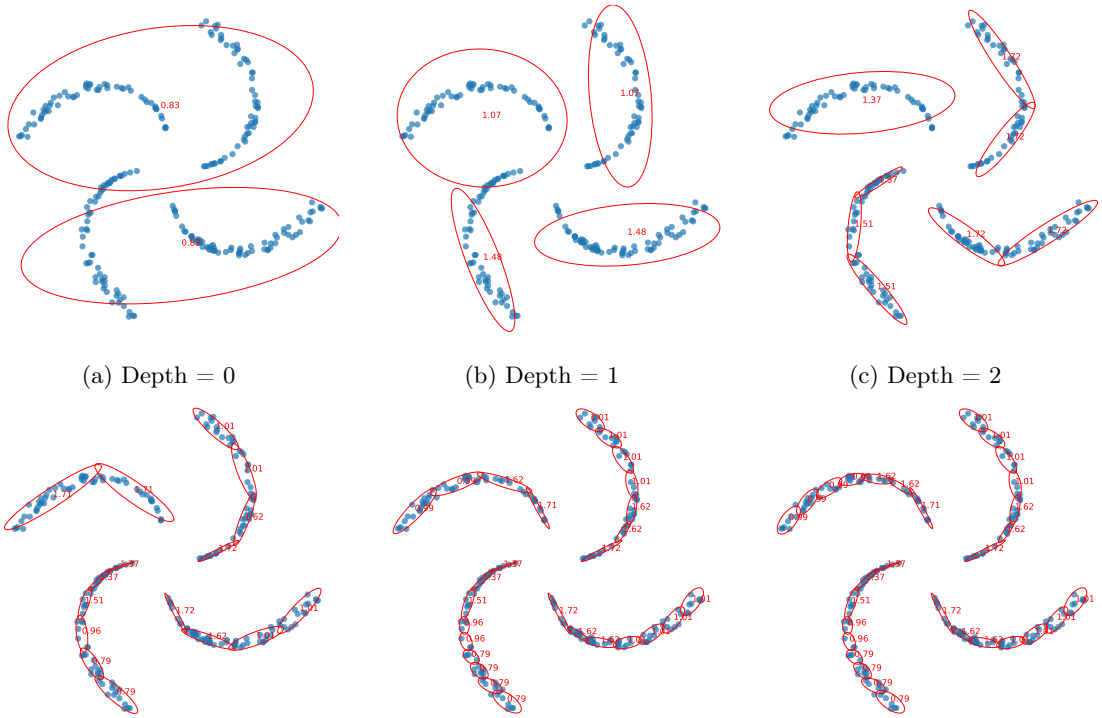

(a) Depth = 0 (b) Depth = 1 (c) Depth = 2

(d) Depth = 3 (e) Depth = 4 (f) Depth = 5

Figure 13: Splitting steps of a single node, showing the data, covariance ellipses and information gain of the parent node for dataset 2

Figure 14 shows the Gaussian PDF distribution of the corresponding leaf nodes on a regular grid according to one tree and according to a Density Forest of 20 trees.

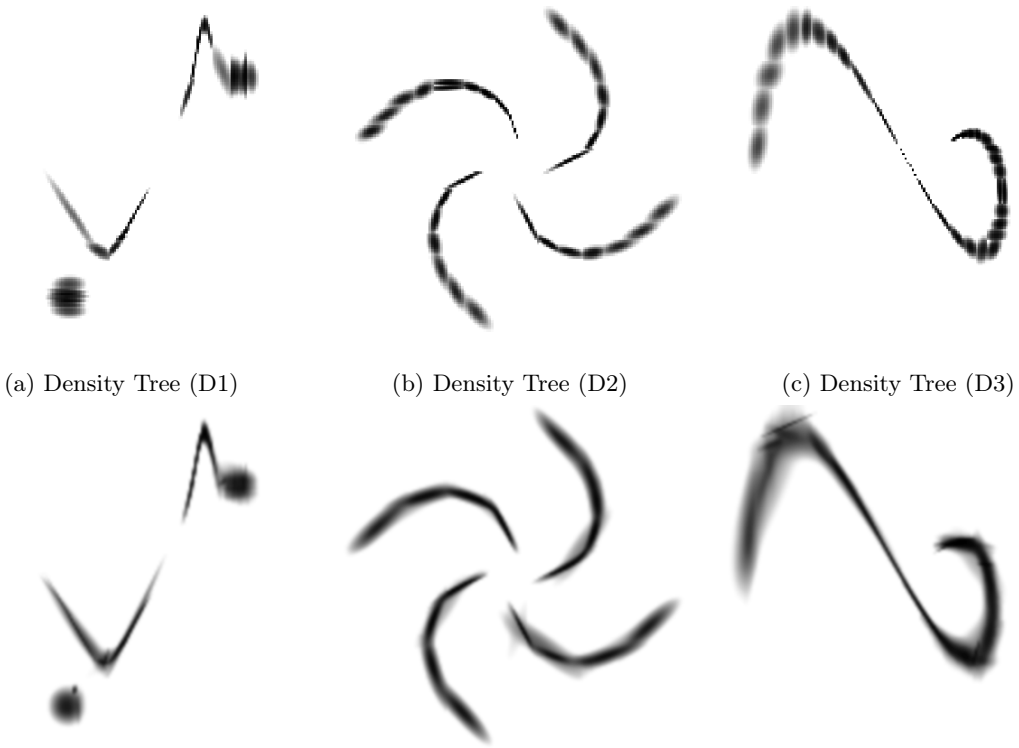

(a) Density Tree (D1) (b) Density Tree (D2) (c) Density Tree (D3)

(d) Density Forest (D1) (e) Density Forest (D2) (f) Density Forest (D3)

Figure 14: Gaussian PDF distribution according to single tree, and according to a Density Forest consisting of 20 trees

While the single tree in figure 14 still clearly reflects the ellipsoids visible in figure 12, the Density Forest shows a smoother probability distribution. In particularly densely concentrated regions, such as near the central parts of the spiral arms in dataset 2, the density is higher, due to smaller Gaussians being fitted to theses regions.

6.3 MNIST

Using the CNN architecture listed in table 3, $N = 10$ models were trained on all training data except for images belonging to the left-out class. The accuracy of each network was evaluated on training and test points belonging to the seen classes (table 6). Since classes are balanced in the MNIST dataset, only the Overall Accuracy, which is almost identical to Average Accuracy in this case, is indicated. Detailed accuracy measures for each left-out class are shown in appendix D.

Training set	Test set
99.34	99.03

Table 6: Mean Overall Accuracy in % for the CNN models trained on $N-1$ classes

First, predictions were made for the unseen class to inspect the outcome distribution (fig. 15). Some left-out classes are mispredicted more homogeneously than others and have a higher mean MSR. A possible explanation could be the different visual similarity between certain digits, such as 4 and 9 which may look similar, whereas no digit clearly resembles the digit 8. It is important to notice that higher intrinsic similarity between classes can make the task of novelty detection harder. Prediction counts for all left-out classes are shown in appendix F.1.

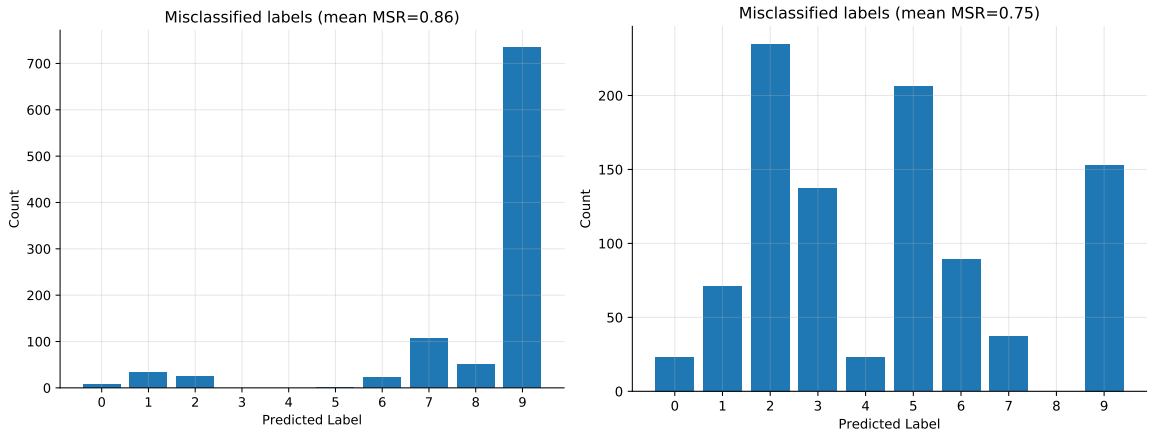

(a) Left-out class 4

(b) Left-out class 8

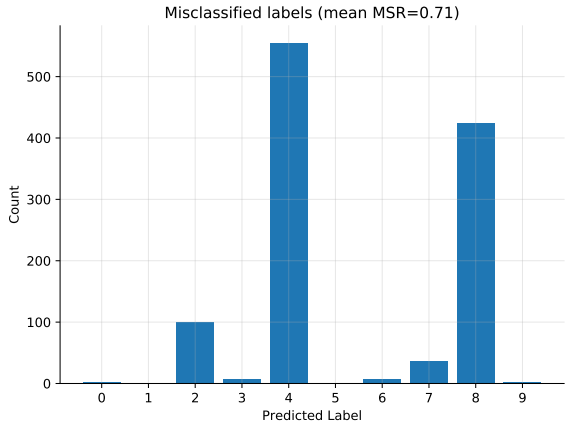

(c) Left-out class 1

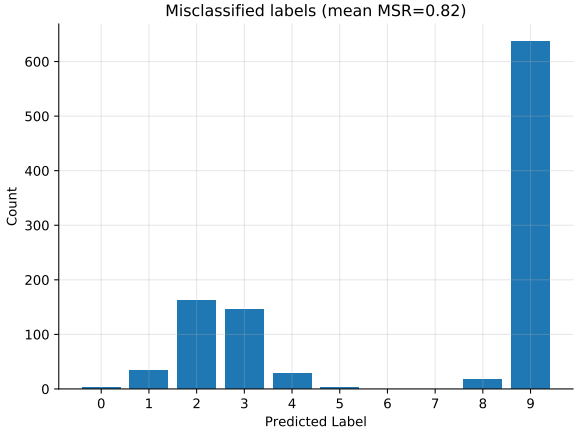

(d) Left-out class 7

Figure 15: Predicted labels for networks with left-out classes 4 and 8 (top) and 1 and 7 (bottom). While digits showing a 4 are mostly mislabeled as a 9, the digit 8 is mislabeled less homogeneously. While one could suppose that digits 1 and 7 look similar and might be confused, digits 7 are mostly classified as digit 9, and digit 1 mostly as digits 4 and 8.

Second, ReLu activations of the Fully Connected layer were extracted as described in section 5.3. For each image, a vector of 128 activations was retrieved. PCA was applied to this vector in order to reduce the redundancy of the filters. For the activations before and after PCA, data separability was checked using t-SNE visualizations (fig. 16). The t-SNE visualizations in all cases looked similar before and after PCA, and are therefore only presented for one of the 10 trained models. t-SNE visualizations for activations of each left-out class after PCA are shown in appendix F.

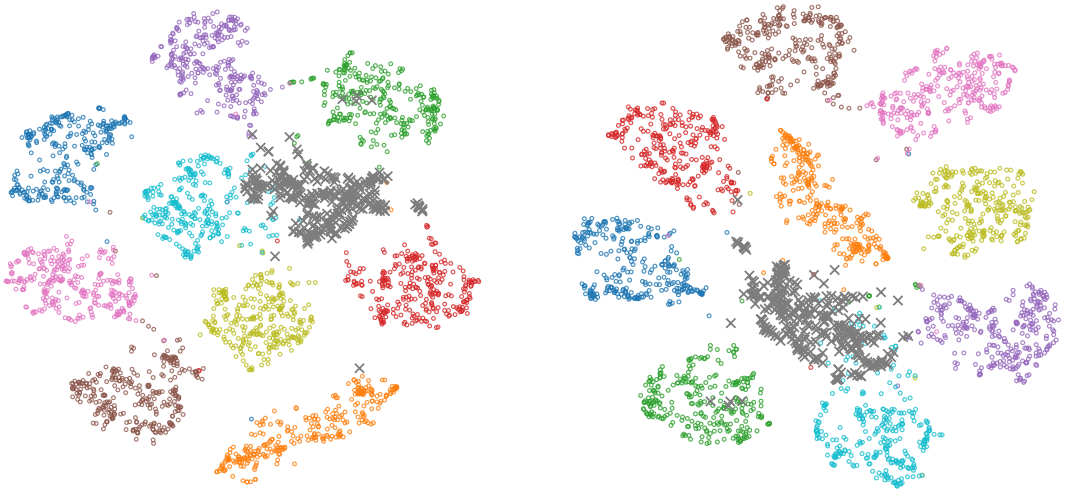

(a) t-SNE before PCA

(b) t-SNE after PCA

Class: 0 1 2 3 4 5 6 7 8 9

× Unseen class

Figure 16: t-SNE of MNIST activations, model with left-out class 7. Both before and after PCA, activations of different classes seem well separable, including the unseen class.

Figure 16 shows that the t-SNE visualizations of the network activations before and after PCA look almost identical. Note that the rotation of the plot before and after applying PCA is irrelevant, since the lower-dimensional data representation yielded by t-SNE only models the pairwise proximities between data points and not their absolute position in space.

For novelty detection methods to work well, the unseen class should be well-separated from the other, seen classes. The t-SNE visualization also indicates that all classes are well-separated, including the unseen class.

The same tendencies with respect to the class confusion shown in figure 15 can also be observed in the t-SNE visualizations (figure 17): while class 4 tends to be confused mainly with class 9, class 8 is confused with several clusters. Unseen class 8 seems to be slightly better separable than unseen class 4, which is very close to class 9.

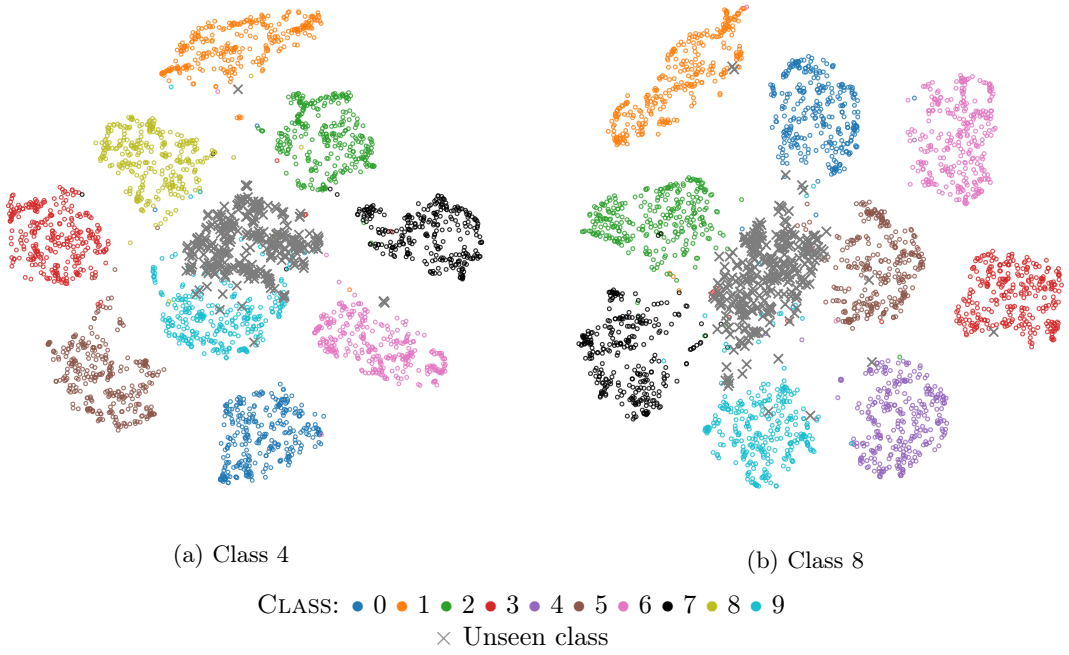

Figure 17: t-SNE of MNIST activations, after PCA transformations.

After retrieving the activations of all data points and applying PCA dimensionality reduction, parameter search has been performed for GMM, OC-SVM and Density Forests. Best hyperparameters found for each left-out class and novelty detection method are listed in table H.1.

AUROC metrics for the Density Forest method and baseline methods are indicated in table 7. Metrics for each class are indicated in appendix table D.2.

MSR	Margin	Entropy	MC-Dropout	GMM	OC-SVM	DF
0.97	**0.97**	**0.97**	0.96	0.67	0.75	0.75

Table 7: Mean AUROC for each left-out class in the MNIST dataset

In the MNIST dataset, GMM, OC-SVM and DF perform worse compared to the baseline methods MSR, margin, entropy and MC-Dropout. Reasons for the lower performance of the pre-softmax based novelty detection methods are discussed in section 7.

6.4 Zurich Dataset

6.5 Overall Results

Since class imbalance is greater than in the MNIST dataset, model performance is indicated for each left-out class separately in table 9. For comparison, accuracy metrics for a CNN trained on all classes is given in table 8. In this section, illustrations are shown for the model trained on all classes but "roads" and the equivalent figures for the other models are shown in appendix G.

Class	Precision [%]	Recall [%]	F1 Score [%]
Roads	83.63	69.77	76.07
Buildings	64.93	88.00	74.72
Trees	79.80	82.69	81.22
Grass	94.06	67.52	78.61
Bare Soil	48.04	71.81	57.57
Water	97.94	91.41	94.56
Railways	0.01	0.01	0.01
Swimming Pools	84.75	89.80	87.20
Average	69.15	70.13	68.75

Table 8: Test set accuracy for the UNET CNN trained on all classes (Overall Accuracy: 77.59 %)

	Training set		Validation set		Test set	
Left-out Class	OA [%]	AA [%]	OA [%]	AA [%]	OA [%]	AA [%]
Roads	71.33	65.09	91.79	80.39	87.92	76.39
Buildings	68.12	62.50	89.44	77.93	83.94	69.38
Trees	65.36	58.84	88.79	72.59	88.58	71.40
Grass	57.27	54.49	79.55	68.15	81.49	69.23
Bare Soil	59.41	53.97	80.43	72.28	80.49	71.01
Water	65.37	62.90	85.73	71.83	84.04	68.31
Railways	62.37	57.96	82.55	71.02	82.11	71.09
Swimming Pools	59.56	57.72	80.55	70.50	82.34	71.34
Mean	63.60	59.18	84.85	73.09	83.86	71.02

Table 9: Accuracy measures for the UNET CNN trained on $N-1$ classes.

A sample visualization of a prediction from a model with the left-out class "roads" is shown in figure 18. Most pixels annotated as "road" in the ground truth are either classified as "buildings", "bare soil" or "railways".

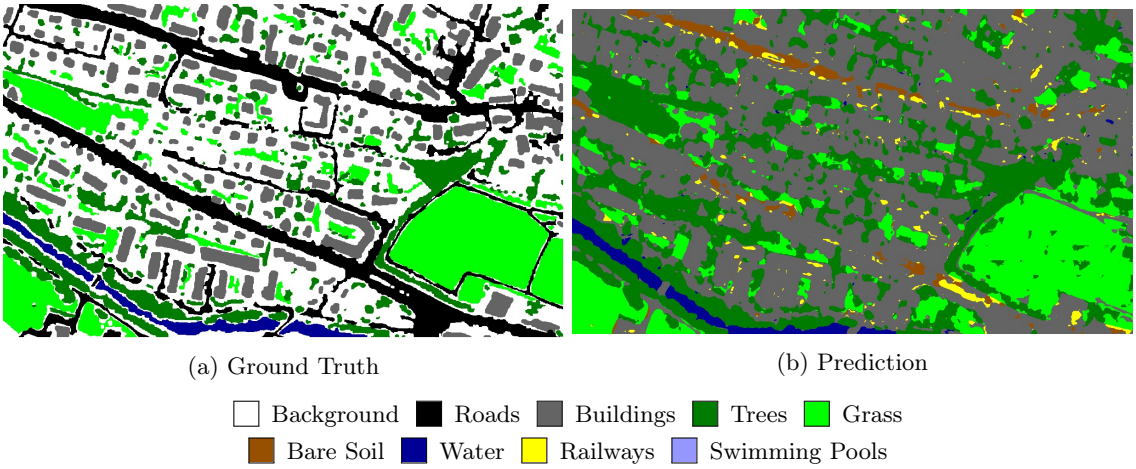

(a) Ground Truth (b) Prediction

Figure 18: Prediction and ground truth for the model trained without the roads class

As for the MNIST dataset, misclassification distributions were checked for all models (fig. 19). Again, more homogeneously misclassified class samples are correlated with higher mean MSR.

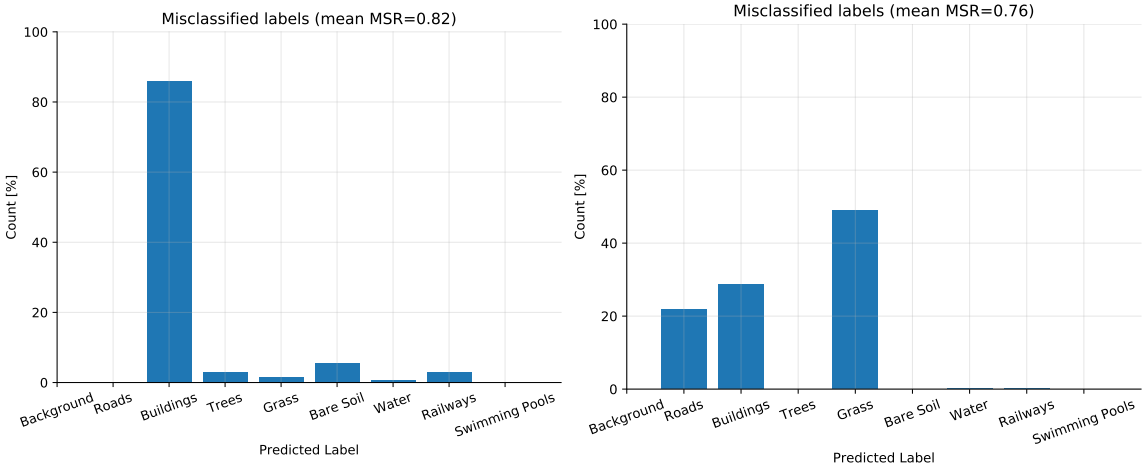

(a) Left-out class "Roads" (b) Left-out class "Trees"

Figure 19: Predictions for network with left-out class "roads" and "trees". While roads are mostly mislabelled as buildings, trees are mislabelled less homogeneously.

After training of the network, activations of all images in the training, validation and test sets were retrieved and PCA was applied to reduce their dimensionality. The cumulative variance explained by each additional component is shown for the model with the left-out class "roads" in figure 9b. As figure 9 shows, less components are needed to explain a high percentage of the data variance compared to the MNIST dataset.

Similar to the MNIST dataset, it was checked by t-SNE visualization if the pre-softmax activations are separable, both before and after PCA (fig. 20). Ideally, both t-SNE plots should show the same relative arrangement between classes. While clusters may be of different sizes, they should be separated according to the classes for a well-enough trained network.

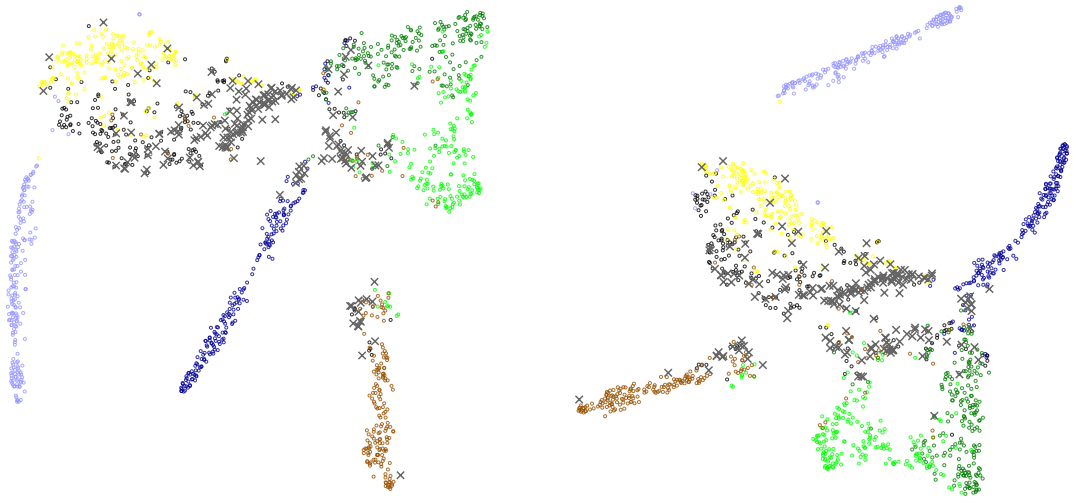

(a) t-SNE before PCA

(b) t-SNE after PCA

Class: • Roads • Buildings • Trees • Grass
• Bare Soil • Water • Railways • Pools
× Unseen class

Figure 20: t-SNE of Zurich dataset activations, model with left-out class buildings. The same number of points are shown by class, although the real class distribution is imbalanced (cf. table 8).

Fig 20 shows that t-SNE visualizations before and after PCA look almost the same. The unseen class "buildings" is confused most strongly with the class "roads", and partly with the classes "'tree" and "grass".

t-SNE visualizations of the classes "roads" and "trees" are shown in figure 21.

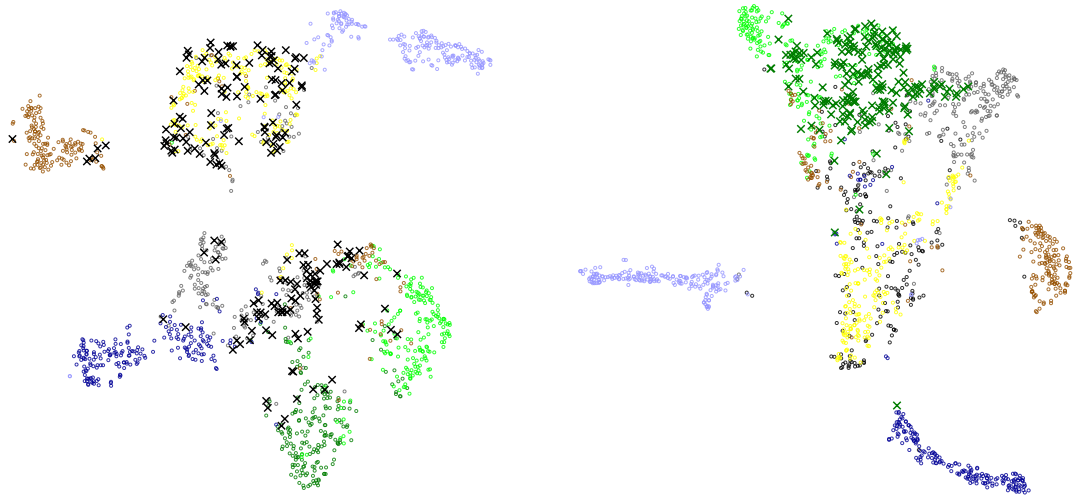

(a) Roads (b) Trees

Class: • Roads • Buildings • Trees • Grass
• Bare Soil • Water • Railways • Pools
× Unseen class

Figure 21: t-SNE of Zurich dataset activations after PCA.

Although there seems to be a confusion between the classes "roads" and "railways" which suggests difficulties to separate both classes, the class "railways" is very rare (fig. 7). It is expected that Density Trees first fit ellipses in high-density regions. Therefore, it is likely that a Density Forest with limited depth will never fits any Gaussians onto the "railways" class. Figure G.2 in appendix shows t-SNE of the activations after PCA for all left-out classes and for the model trained on all classes. While some classes are always clearly separable from each other, such as bare soil, water and swimming pools, some classes are more mixed together, such as buildings and roads, or grass and trees. It is also noteworthy that some classes are only separable from others when seen during training, such as the class "water", while some also remain separable when unseen, such as the class "swimming pools".

Best parameters for each left-out class model and novelty detection method are shown in appendix table H.2. AUROC for each left-out class and novelty detection method is shown in table 10.

Left-Out Class	MSR	Margin	Entropy	MC-Dropout	GMM	OC-SVM	DF
Roads	0.60	0.59	0.61	0.59	0.66	0.50	**0.70**
Buildings	0.65	**0.66**	0.65	0.65	0.58	0.63	0.64
Trees	0.74	0.74	0.74	0.75	0.66	**0.76**	0.56
Grass	0.38	0.37	0.39	0.39	0.47	0.31	**0.54**
Bare Soil	0.68	0.70	0.63	0.60	0.66	**0.78**	0.65
Water	0.59	0.60	0.58	0.58	0.59	0.39	**0.64**
Railways	0.57	**0.59**	0.53	0.54	0.44	0.52	0.37
Swimming Pools	0.26	0.28	0.23	0.28	**0.99**	0.97	**0.99**
Average	0.56	0.57	0.55	0.55	0.63	0.61	**0.64**

Table 10: AUROC for each left-out class

Table 10 indicate that the DF outperforms other novelty detection methods in 3 of 8 classes and pre-softmax-based methods GMM, OC-SVM and DF together outperform the softmax-based methods in 6 out of 8 classes. DF clearly outperforms other methods on the Roads and Water classes. Pre-softmax based methods clearly outperform softmax-based methods on the Swimming Pools class. Visual results of the different methods are shown in appendix figures G.4 - G.5. ROC curves used to produce the AUROC metrics of table 10 are shown in appendix figure G.12.

6.6 Visual interpretation

To illustrate the performance of the novelty detection methods, confidence images for individual left-out classes can be analyzed and visualized. In this section, results are compared according to the classes on which the Density Forest performs better or worse than baseline methods. Visual examples are provided for MSR and Density Forests. Figures for all methods and left-out classes are shown in appendix figures G.4 - G.11.

A property of novelty detection methods is that they attribute extreme values to outliers, leading to skewed distributions of the confidence values. This can be observed in the results of the methods GMM, OC-SVM and DF. In the case of novelty detection, some particular objects of the image may be recognized as very uncertain, leading to lesser visibility of confidence differences in the rest of the image. Therefore, histogram equalization was applied to the confidence images of GMM, OC-SVM and DF to enhance the overall image contrast and show more local differences between classes [12]. Individual objects with very high uncertainty are shown using the original image (fig. 22).

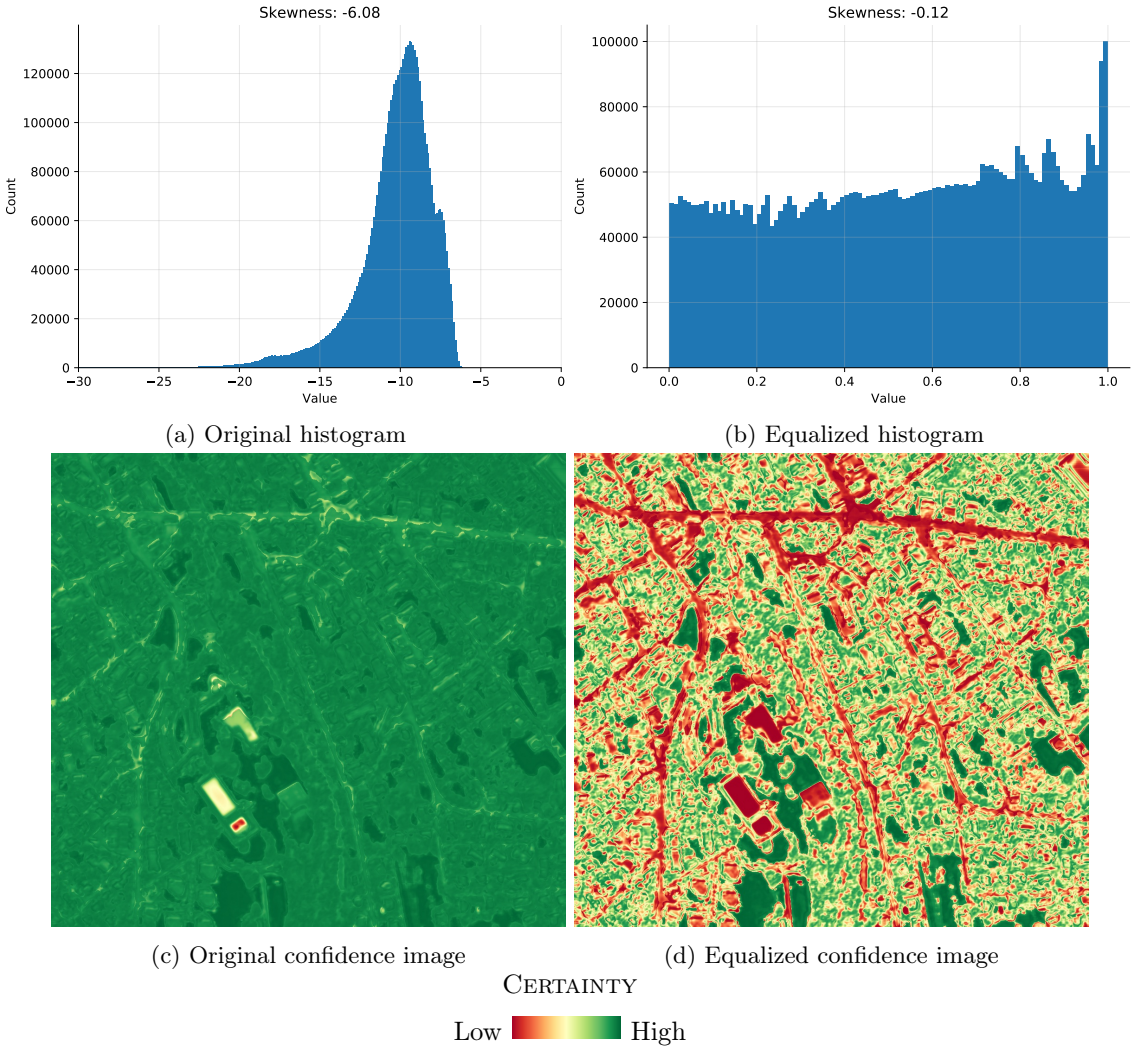

(a) Original histogram

(b) Equalized histogram

(c) Original confidence image

(d) Equalized confidence image

Figure 22: Original and equalized confidence distributions for DF, using the left-out class "Roads". While outliers are visible in the original figure, smaller confidence differences between classes are better visible after histogram equalization.

Figure 23 shows visual results for the class "roads". Density Forest here outperforms the other methods, confirming visually that it has the highest AUROC values of all confidence estimation methods (table 10). The unseen class "Roads" clearly appears to be the least certain, while for MSR, the roads seem as uncertain as other classes. MSR just like margin and entropy, the other baseline methods based on the softmax output, mainly show low certainty along class changes (figure G.4.

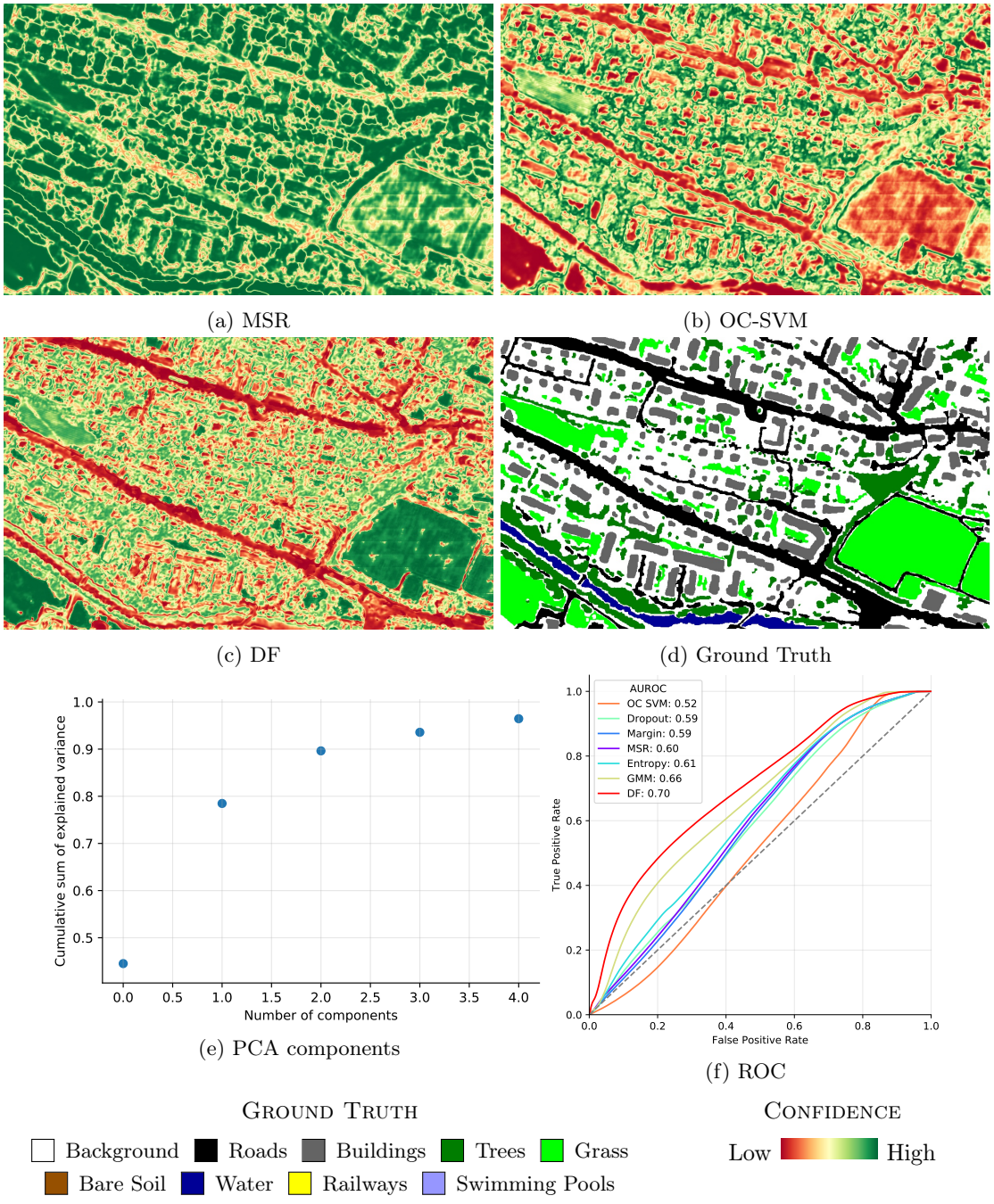

Figure 23: Visual uncertainty results for selected methods on left-out class "Roads" and corresponding ground truth. Contrast stretching and histogram equalization have been applied to OC-SVM and DF images for better visibility. Variance per PCA component and ROC curves are shown below the confidence images.

Figure 24 shows a class for which the Density Forest underperforms. In this case, OC-SVM shows the best performance in detecting the unseen class "trees" (along the river and on the top-right side of the field). While both the winning method OC-SVM and DF show low confidence in the regions containing trees, the Density Forest in addition shows very low confidence along the river and along some parts of the roads.

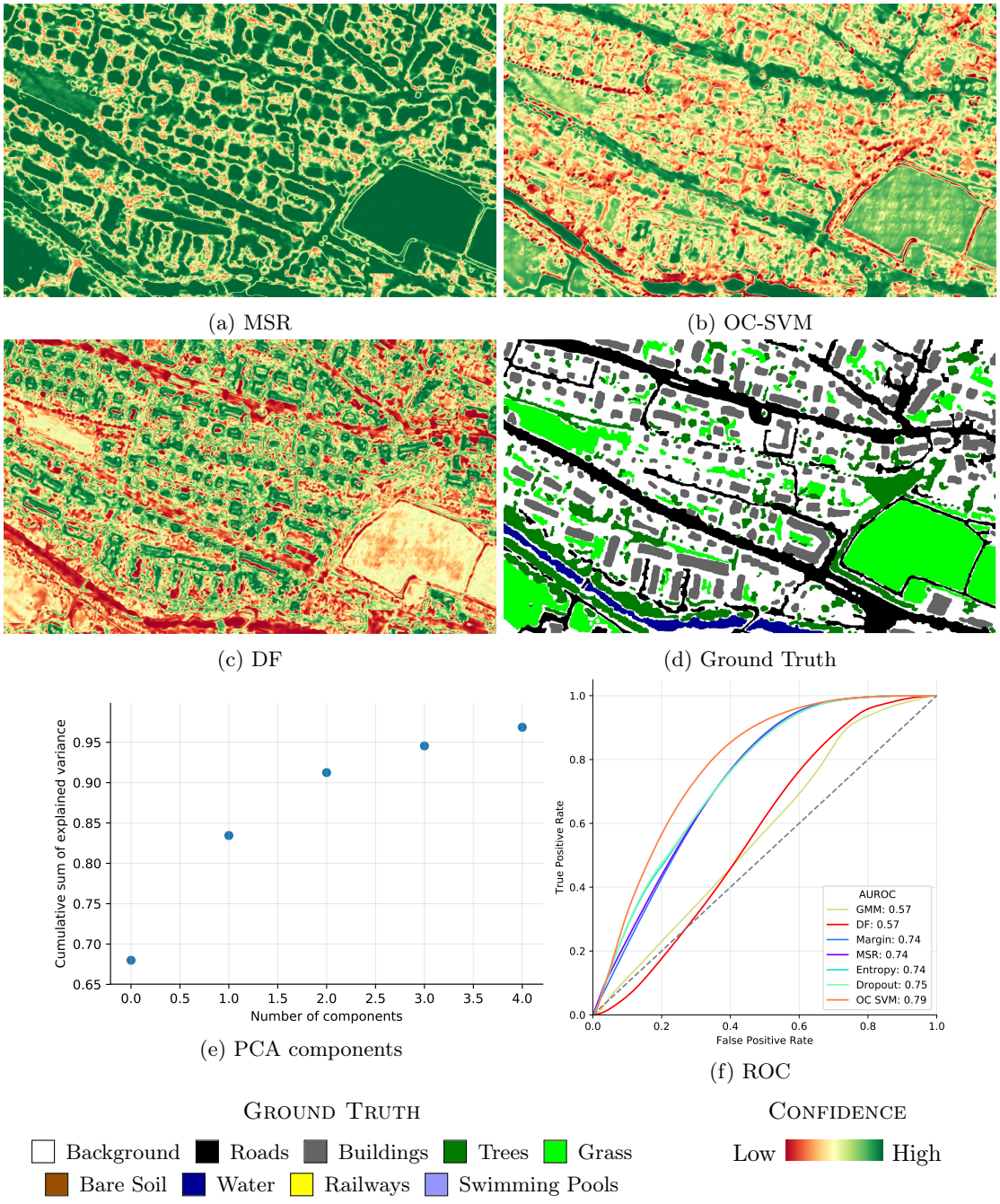

(a) MSR (b) OC-SVM

(c) DF (d) Ground Truth

(e) PCA components (f) ROC

Figure 24: Visual uncertainty results for selected methods on left-out class "Trees" and corresponding ground truth. Contrast stretching and histogram equalization have been applied to OC-SVM and DF images for better visibility. Variance per PCA component and ROC curves are shown below the confidence images.

For both left-out classes roads and trees, a low number of PCA components are needed to explain the initial variance of activations. Visual results, explained variance by PCA components and ROC curves are provided for all left-out classes in appendix G.

Figure 25 shows the confidence values of the different methods for the left-out class "trees" on a subset of all points used to produce the t-SNE visualizations. All points with a solid border belong to the unseen class. Ideally, those points should be colored red (uncertain) while points of other classes should be yellow or green. Figure 25 also shows different behavior in the seen classes between novelty detection methods. Softmax-based methods MSR, margin, entropy and MC-Dropout all behave similarly and identify the regions of lowest confidence at the borders of clusters and within the unseen class. The pre-softmax based confidence measures GMM, OC-SVM and DF behave similarly and generally attribute a higher confidence to the cluster centers and unseen class, while GMM and DF also attribute lower certainty to points of the class "bare soil' and identify the class "swimming pool" as particularly uncertain, which could indicate their ability better identify heterogeneous classes, such as "bare soil", and classes with few samples, such as "swimming pools".

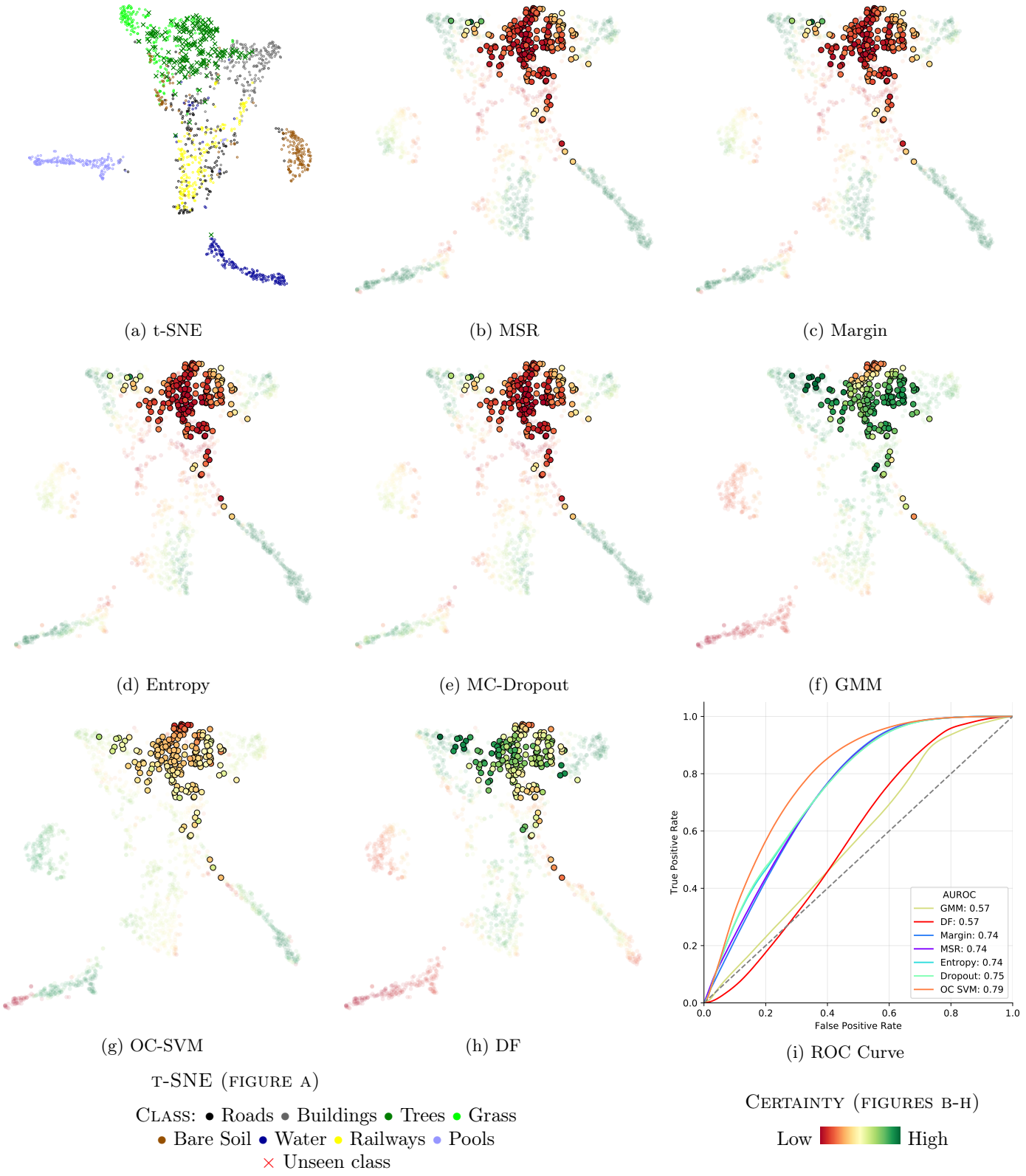

(a) t-SNE (b) MSR (c) Margin

(d) Entropy (e) MC-Dropout (f) GMM

(g) OC-SVM (h) DF (i) ROC Curve

Figure 25: Confidence for the left-out class "Trees" according to different methods plotted onto t-SNE, showing the n points with the lowest confidence where n is the number of points per class shown in the t-SNE plot. Points of the unseen classes are indicated with a solid-edge circle. Ideally, all solid-edge circles should be red, and all other points green. The original t-SNE plot and the ROC curves for each method are shown for comparison.

6.7 Particular Objects

In addition to analyzing the performance of Density Forest and baseline methods in novelty detection, a few particular objects can be distinguished on the test images for which the pre-softmax activations-based methods GMM, OC-SVM and Density Forest all show particularly low confidence. In the following, confidence maps of the Density Forest and MSR methods of are shown for particular objects for which Density Forest indicates low confidence. GMM or OC-SVM mostly yield confidence values similarly low as those of Density Forest for these objects and are shown in appendix G.

Figure 26 shows a particular object annotated as a swimming pool, containing visible swimming lanes. While MSR attributes a fairly high confidence to this region, again just highlighting the borders of the object, DF yields a very low confidence within the object.

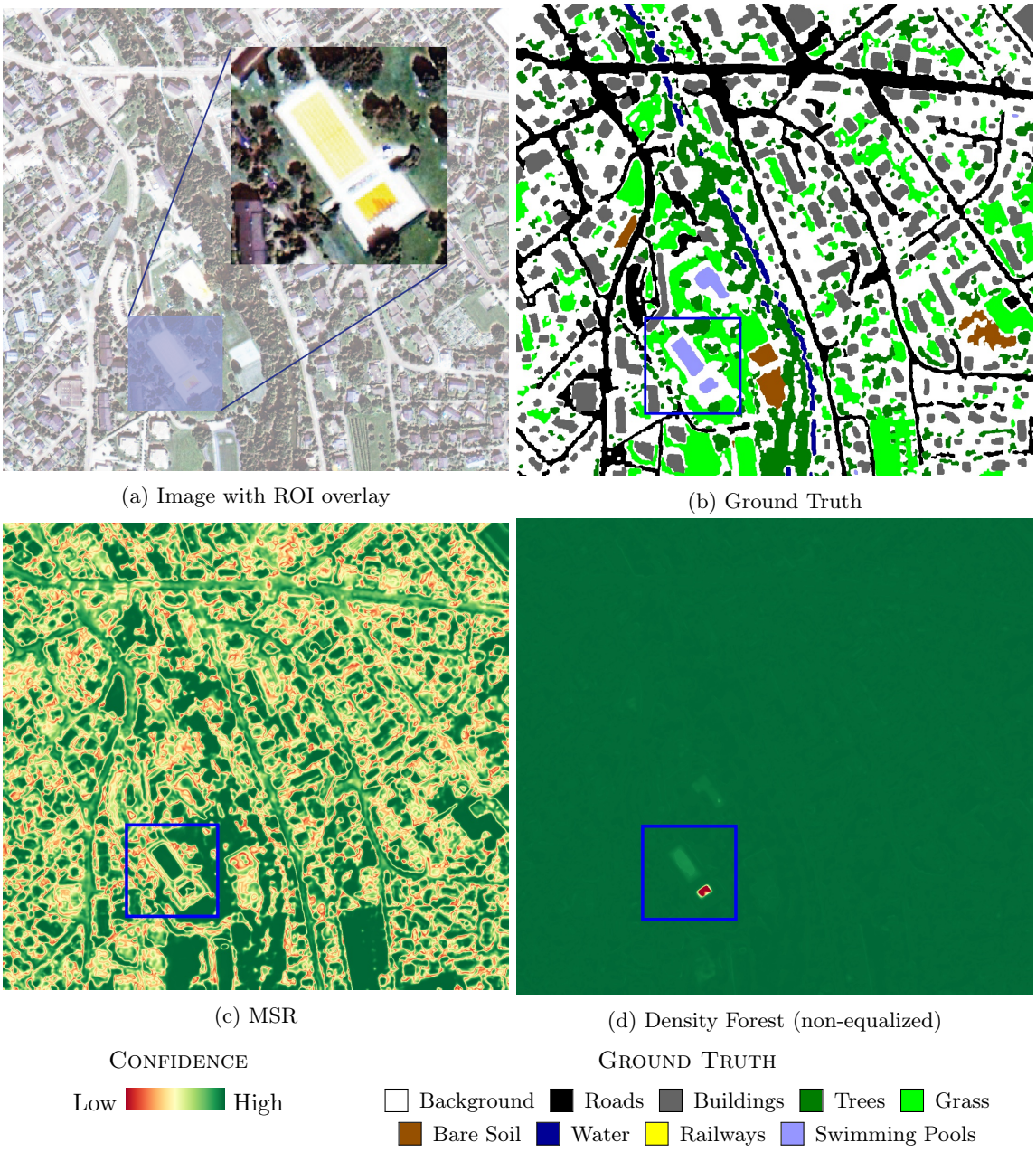

Figure 26: Swimming pool object with MSR and DF confidence images

Figure 26 shows another region around a soccer pitch for which DF yields low confidence, seemingly a race track.

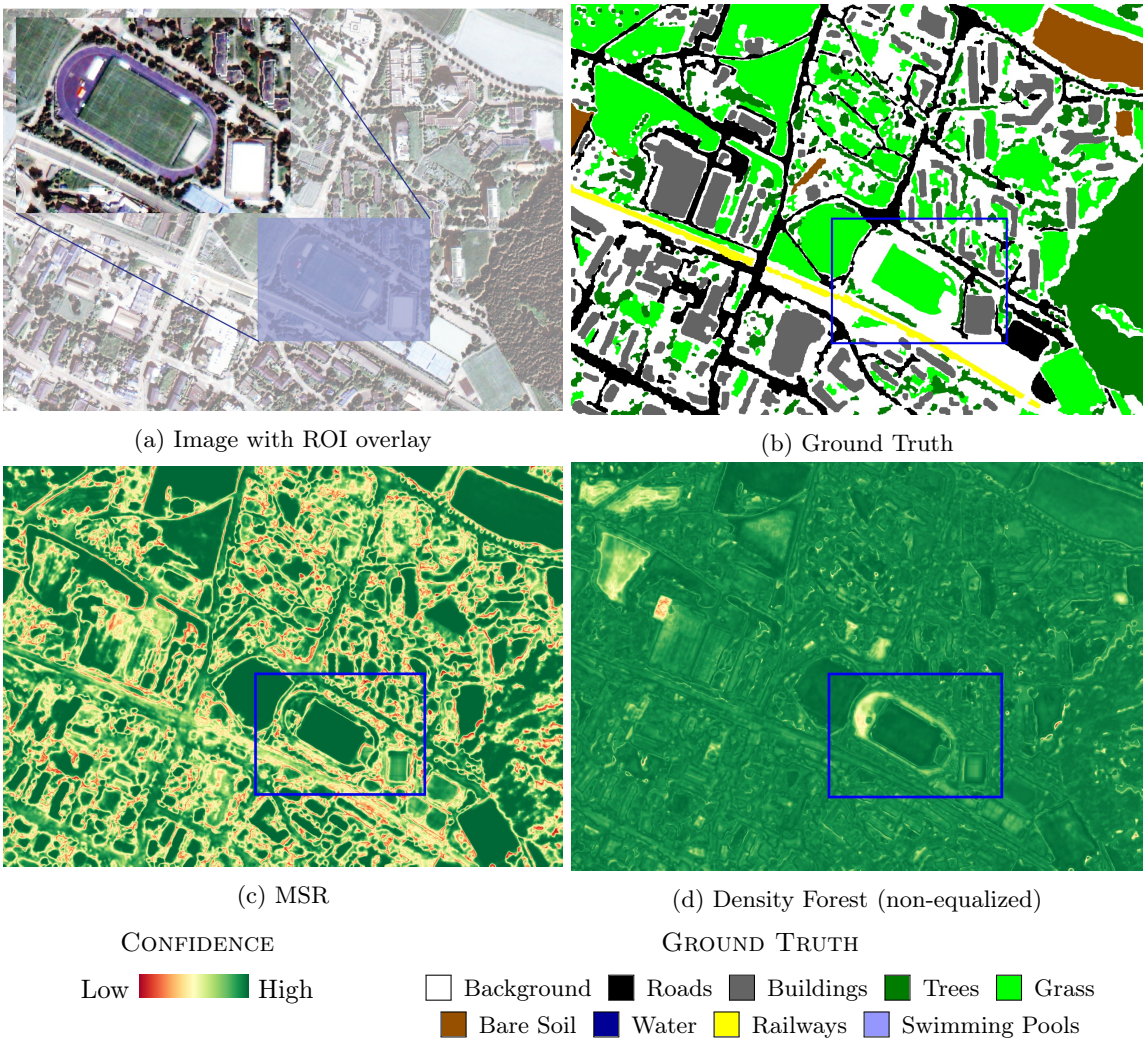

(a) Image with ROI overlay

(b) Ground Truth

(c) MSR

(d) Density Forest (non-equalized)

Figure 27: Soccer pitch object with MSR and DF confidence scores

For the swimming pool in figure 26, the reason for the varying confidence between MSR and Density Forest could be the number of training samples for the swimming pool class (fig. 7). For the race track in figure 27, there is no corresponding land cover class, explaining the lower confidence of the Density Forest.

Generally, GMM, OC-SVM and DF attribute very low values to particular objects which seem very different. For the class "swimming pools", all three methods strongly outperform softmax-based confidence estimators (table 10). Since the class "swimming pool" is very rare, this might indicate that these methods work best for outlier detection, where the novelties are very few and different from the "normal" distribution.

7 Discussion

7.1 MNIST dataset

For the MNIST dataset, Density Forests and other pre-softmax based confidence estimation methods showed worse performance in detecting novel classes than all other baselines, despite t-SNE visualizations which indicate that data should be separable (fig. 16). A reason for this could be the low variance explained by the first PCA components, requiring to keep a high number of PCA components (fig. 9).

Dimensionality reduction A reason for this under-performance of pre-softmax novelty detection methods in the MNIST dataset could lie in the variance explained by the first PCA components of the activations. While for the Zurich dataset, a lower number of components is needed to explain the initial data variance, MNIST requires a much higher amount of components to explain the initial data variance (fig. 9). A possible explanation for this could be the number of components used in the FC layer of the network: the MNIST CNN (table 3) has 128 filters in the FC layer, while the U-Net used for the Zurich dataset has only 32 layers before the final softmax activation layer. For the MNIST and Zurich datasets, PCA can reduce the initial high-dimensional data from 128 to around 30-40 dimensions and from 32 to 5-10 dimensions respectively, preserving more than 95% of the variance (tables 3 and E.1). A different dimensionality reduction method than PCA would be desirable in order to reduce the data to a lower number of dimensions while preserving the structure of the high-dimensional data. The influence of other dimensionality reduction method on the performance of Density Forests should be studied more deeply.

Network accuracy Also, the networks have been trained to a very high test accuracy of around 99% and the softmax-based indicators MSR, margin, entropy show high performance. Investigating the influence of the network accuracy on the performance of softmax-based confidence estimation methods should be studied more deeply. A high network accuracy should correlate with linearly separable data at the end of the network, thus the pre-softmax activations should be very clearly separable. This seems to be confirmed in the t-SNE visualizations of the pre-softmax activations, showing clustering of activations by class.

7.2 Zurich dataset

Regarding the Zurich dataset, Density Forests and other pre-softmax-based confidence estimation methods show on average a significant improvement in terms of novelty detection over softmax-based methods. While the performance of the classifiers GMM, OC-SVM and DF is partly inconsistent, this shows at least that taking into account the pre-softmax network activations yields more information than just estimating the confidence based on the softmax output. Yet, the performance of various novelty detection methods differ strongly between classes. Some of the reasons for this varying performance are discussed below.

Class confusion Regarding the pre-softmax methods, part of the inconsistency might be due to the distribution of the activations used as input for training the confidence estimators. The t-SNE visualizations show different clustering behaviour for the activations of the Zurich dataset than for activations of the MNIST dataset, with some classes in the Zurich dataset being further away from other classes and some being regularly confused (fig. 20). Pre-softmax based methods seem to work better on class activations which are well-separated from other classes. All pre-softmax-based confidence methods clearly outperform other baselines in the class "swimming pools" (fig. G.11). This might be in part due to the fact that these activations are very well separable from others, even for the model trained without the class "swimming pools" (fig. G.2h). While the t-SNE also indicates good separation of the class water for models trained with the class, it seems that the class is less well-separated when not seen during training, making it thus more difficult to detect for activation-based methods (fig. G.2f). Therefore, a possible reason for the varying performance between classes could be how well they are separated even if they haven't been seen during training .

Gaussianity in high dimensions The partly inconsistent performance of Density Forests as well as GMM could be due to their underlying assumption of a Gaussian data distribution. Both methods rely on finding the support of the "normal" data through fitting a certain number of Gaussian distributions to the data. In high-dimensional, noisy data, this might be especially difficult due to the curse of dimensionality, making the notion of distance less meaningful [20].

Data separability Although the task of a neural network is to make data linearly separable, optimal hyperparameters for OC-SVM included non-linear kernels in some cases (table H.2). This could be due either to an inability of the network to separate the classes due to the number of filters and other aspects related to the network architecture, or too few training iterations. A possible advantage of algorithms such as OC-SVM could be their ability to increase data separability by explicitly reorganizing non-linearities from non-optimally trained networks, using the kernel trick. Although Density Forests do not explicitly apply any kind of feature augmentation, forest-based methods can model non-linear data distributions through bagging of many weak learners. The relation between the network accuracy, best OC-SVM kernel for novelty detection and novelty detection performance should be further studied.

8 Conclusion

Density Forests follow the idea to harness the information that a network produces in order to make data separable in order to detect new, unseen data in the test set. This study has shown that the developed method works in a majority of cases, within certain limitations, and that softmax-based confidence measures are unsuitable for novelty detection in almost in all cases. While pre-softmax based confidence measures have outperformed softmax-based measures most times, there are some critical limitations.

First, the implemented pre-softmax-based confidence measures require a certain number of hyper-parameters to be tuned in order to work. This task may be time-consuming and the correct range of parameters difficult to identify, while in some cases being not even possible due to a too small

dataset, making it difficult to split it into a training, validation and test set of sufficient sizes to perform such hyperparameter search. If the unseen class is very rare, it may not be present in a validation set used to find optimal parameters. Second, the network structure may play an important role for the performance of both softmax-based and pre-softmax-based confidence measures. A network with many filters in the fully-connected layer may produce redundant and noisy information spread over many filters, resulting in a long activations vector even after PCA. This not only deteriorates the training and prediction time of each model but may also lead to greater difficulties in separating high-dimensional activations. In addition, the influence of the network accuracy on the performance of each confidence measure is to be discussed. Third, Density Forests, GMM and OC-SVM work better for very different activations, such as those of the class "swimming pools". Thus, in order to effectively identify unseen points, a special meta-loss would need to be introduced in the network to maximize the distance between pairs of activations of different classes.

8.1 Main Contributions

- Density Forests have been implemented and applied to a toy dataset as well as a more complex dataset consisting of high-dimensional neural network activations. Their potential for novelty detection in the MNIST dataset and in a real-world, complex dataset has been assessed and discussed.
- Importantly, a ready-to-use library was implemented with detailed usage instructions and code documentation, which can be easily installed using the command `pip install density_forest`. The code and illustrations are hosted on GitHub (`https://github.com/CyrilWendl/SIE-Master`), including a variety of methods training density trees or Density Forests on a training set and predicting a confidence value for a data set. In addition, the library includes a number of generic functions that include:

  1. Perform hyperparameter search to find the best parameter set for training a Density Forest as described in section 5.5.
  2. Generate synthetic datasets as described in section 4.1.
  3. Data augmentation functions on to transform an image and a corresponding ground truth at the same time for semantic segmentation, as described in section 5.1.
  4. Generic plotting functions to produce all the visualizations of this report.

  The syntax for fitting Density Forests, predicting confidence values, performing hyperparameter search and using auxiliary functions is described in the `README.md` of the GitHub repository.
- First, this study has aimed to show the potential of using pre-softmax activation vector to assess the possibility to improve novelty detection in trained CNNs. In a more complex, real-world example, this idea has proven successful, however only within the limited scope of the restrictions described above.

8.2 Future Research

Further research should go into understanding the reasons for the inconsistent behaviour of Density Forests.

Influence of network architectures Regarding Density Forests, the influence of the dimensionality on the performance of Density Forests should be evaluated more thoroughly. For instance, different network architectures with a varying number of pre-softmax activations could be trained and compared with respect to the Density Forest performance. Such a comparison has not been implemented because of the explicit assumption that Density Forests should not be applicable to many different standard network architectures without modifying them. Yet, there are good reasons to assume that Density Forests will deal better with lower-dimensional activations.

Datasets Similarly, to further study the performance of Density Forests, the method should be applied to further dataset, and using different network architectures than the ones tested [43, 8].

Meta-Loss to increase class separability For similar reasons, contrary to the method proposed by Mandelbaum and Weinshall [31], no special meta-loss has been implemented to maximize the distance between activations belonging to different classes, again because of the assumption that the proposed confidence measure should not require any changes in the network architecture. It would however be interesting to see if there are significant performance gains for any of the pre-softmax-based methods if such a meta-loss was implemented.

Parameter sensitivity In addition to finding the best parameter set, the sensitivity of each parameter should be assessed. This could potentially reduce the number of hyperparameters and thus accelerate parameter search.

Further research ideas To avoid having to model the distribution of high-dimensional activations, a different idea for a confidence measure would be to work directly with the network activations and weights: In addition to retrieving the activations $\mathrm{x}_i^{(L)}, i \in 1...n$, one could also retrieve the weights $\mathrm{w}_{i,j}^{(L)}$ for a class j just before they are passed to the final softmax activation (fig. 28). By looking at their sign (negative / positive contribution to a class) or measuring their entropy, the degree of agreement between activations could be measured and used as a confidence indicator.

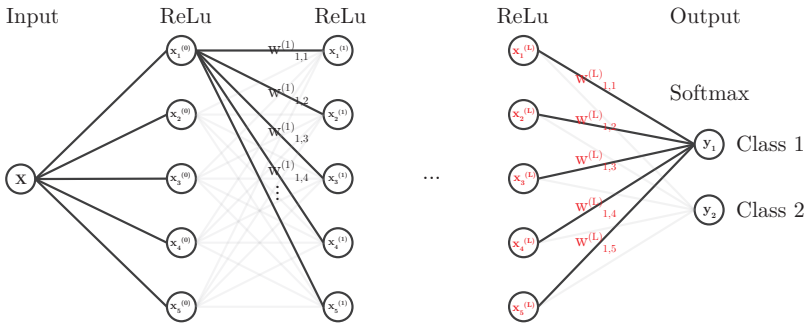

Figure 28: Alternative confidence measure scheme: red parts are to be retrieved and multiplied to measure the degree of agreement of the softmax inputs.

Further, similar ideas to estimate the confidence using activations include maximizing differences between the separating planes produced by each softmax input, via a special meta-loss. This way, the network would learn to find as many distinct separations between classes as possible, and thus map class distributions. However, this again contradicts the basic idea of the proposed methodology, which is to build on an existing network architecture.

Evaluation Any of the analyzed confidence methods are heuristic in nature and are evaluated according to an application-specific goal. The notion of confidence in many cases remains related to particular applications such as error detection, anomaly detection or novelty detection. A formal proof of the equivalence between some optimal, pre-softmax activations-based confidence measure and probabilistic uncertainty measures yet has to be provided. Due to their heuristic nature, confidence measures should also be evaluated in applied contexts, such as active learning.

Conclusion Ultimately, this study has shown a high potential of Density Forests and pre-softmax confidence measures to improve novelty detection performance without changing the structure of the network. Although less successful in error detection, the network activations-based methods GMM, OC-SVM and DF in most cases show better performance than the baselines relying purely on the softmax output. Further research possibilities in this direction should show whether the information contained in the network activations can be used to determine the uncertainty of a network, without changing its architecture.

References

[1] M. Z. Alom, M. Hasan, C. Yakopcic, T. M. Taha, and V. K. Asari. "Recurrent Residual Convolutional Neural Network based on U-Net (R2U-Net) for Medical Image Segmentation". In: *CoRR* abs/1802.06955 (2018).

[2] Y. Bahat and G. Shakhnarovich. "Confidence from Invariance to Image Transformations". In: (Apr. 2018).

[3] A. Beghi, L. Cecchinato, and M. A. Rampazzo. "A One-Class SVM Based Tool for Machine Learning Novelty Detection in HVAC Chiller Systems". In: 2014.

[4] C. M. Bishop. "Novelty Detection and Neural Network Validation". In: 1994.

[5] L. Breiman. "Bagging Predictors". In: *Machine Learning* 24 (1996), pp. 123–140.

[6] L. Breiman. "Random Forests". In: *Machine Learning* 45.1 (2001), pp. 5–32.

[7] M. M. Breunig, H.-P. Kriegel, R. T. Ng, and J. Sander. "LOF: Identifying Density-Based Local Outliers". In: *SIGMOD Conference*. 2000.

[8] B. H. U. of California Berkeley and R. G. M. R. Redmond. "Hypercolumns for Object Segmentation and Fine-grained Localization". In: 2015.

[9] S. Choi, K. Lee, S. Lim, and S. Oh. "Uncertainty-Aware Learning from Demonstration using Mixture Density Networks with Sampling-Free Variance Modeling". In: *CoRR* abs/1709.02249 (2017).

[10] A. Criminisi, E. Konukoglu, and J. Shotton. *Decision Forests for Classification, Regression, Density Estimation, Manifold Learning and Semi-Supervised Learning*. Tech. rep. 2011. URL: https://www.microsoft.com/en-us/research/publication/decision-forests-for-classification-regression-density-estimation-manifold-learning-and-semi-supervised-learning/.

[11] A. P. Dempster, N. M. Laird, and D. B. Rubin. "Maximum Likelihood from Incomplete Data via the EM Algorithm". In: 1977.

[12] "Digital Image Processing Third Editionà-p E. Woods". In: 2012.

[13] H. Dong, G. Yang, F. Liu, Y. Mo, and Y. Guo. "Automatic Brain Tumor Detection and Segmentation Using U-Net Based Fully Convolutional Networks". In: *MIUA*. 2017.

[14] Y. Gal. "Uncertainty in Deep Learning". PhD thesis. University of Cambridge, 2016.

[15] Y. Gal and Z. Ghahramani. "Dropout as a Bayesian approximation: Insights and Applications". In: *Deep Learning Workshop, ICML*. 2015.

[16] Y. Gal and Z. Ghahramani. "Dropout As a Bayesian Approximation: Representing Model Uncertainty in Deep Learning". In: *Proceedings of the 33rd International Conference on International Conference on Machine Learning - Volume 48*. ICML'16. New York, NY, USA: JMLR.org, 2016, pp. 1050–1059.

[17] I. J. Goodfellow, J. Shlens, and C. Szegedy. "Explaining and Harnessing Adversarial Examples". In: *CoRR* abs/1412.6572 (2014).

[18] B. Hammer and T. Villmann. "How to process uncertainty in machine learning?" In: *ESANN*. 2007.

[19] D. Hendrycks and K. Gimpel. "A Baseline for Detecting Misclassified and Out-of-Distribution Examples in Neural Networks". In: *CoRR* abs/1610.02136 (2016). arXiv: 1610.02136. URL: http://arxiv.org/abs/1610.02136.

[20] A. Hinneburg, C. C. Aggarwal, and D. A. Keim. "What Is the Nearest Neighbor in High Dimensional Spaces?" In: *VLDB*. 2000.

[21] A. Hinneburg and D. A. Keim. "Optimal Grid-Clustering: Towards Breaking the Curse of Dimensionality in High-Dimensional Clustering". In: *VLDB*. 1999.

[22] M. Kampffmeyer, A. B. Salberg, and R. Jenssen. "Semantic Segmentation of Small Objects and Modeling of Uncertainty in Urban Remote Sensing Images Using Deep Convolutional Neural Networks". In: *2016 IEEE Conference on Computer Vision and Pattern Recognition Workshops (CVPRW)*. 2016, pp. 680–688.

[23] M. Kampffmeyer, A.-B. Salberg, and R. Jenssen. "Semantic Segmentation of Small Objects and Modeling of Uncertainty in Urban Remote Sensing Images Using Deep Convolutional Neural Networks". In: *2016 IEEE Conference on Computer Vision and Pattern Recognition Workshops (CVPRW)* (2016), pp. 680–688.

[24] A. Kendall and Y. Gal. "What Uncertainties Do We Need in Bayesian Deep Learning for Computer Vision?" In: *CoRR* abs/1703.04977 (2017). arXiv: 1703.04977. URL: http://arxiv.org/abs/1703.04977.

[25] B. Lakshminarayanan, A. Pritzel, and C. Blundell. "Simple and Scalable Predictive Uncertainty Estimation using Deep Ensembles". In: (Dec. 2016).

[26] Y. LeCun, C. Cortes, and C. Burge. *The MNIST Database of Handwritten Digits*. URL: http://yann.lecun.com/exdb/mnist/.

[27] C. Leibig, V. Allken, M. S. Ayhan, P. Berens, and S. Wahl. "Leveraging uncertainty information from deep neural networks for disease detection". In: 7 (Dec. 2017).

[28] J. Levinson, J. Askeland, J. Becker, J. Dolson, D. Held, S. Kammel, J. Z. Kolter, D. Langer, O. Pink, V. R. Pratt, M. Sokolsky, G. Stanek, D. Stavens, A. Teichman, M. Werling, and S. Thrun. "Towards fully autonomous driving: Systems and algorithms". In: *2011 IEEE Intelligent Vehicles Symposium (IV)* (2011), pp. 163–168.

[29] F. T. Liu, K. M. Ting, and Z.-H. Zhou. "Isolation Forest". In: *2008 Eighth IEEE International Conference on Data Mining* (2008), pp. 413–422.

[30] L. van der Maaten, G. E. Hinton, and Y. Bengio. "Visualizing Data using t-SNE". In: 2008.

[31] A. Mandelbaum and D. Weinshall. "Distance-based Confidence Score for Neural Network Classifiers". In: (Sept. 2017).

[32] M. Markou and S. Singh. "Novelty detection: a review - part 1: statistical approaches". In: *Signal Processing* 83 (2003), pp. 2481–2497.

[33] M. Markou and S. Singh. "Novelty detection: a review - part 2: : neural network based approaches". In: *Signal Processing* 83 (2003), pp. 2499–2521.

[34] D. Marmanis, J. D. Wegner, S. Galliani, K. Schindler, M. Datcu, and U. Stilla. "Semantic Segmentation of Aerial Images with an Ensemble of Cnns". In: 2016.

[35] A. Menderes, A. Erener, and G. Sarp. "Automatic Detection of Damaged Buildings after Earthquake Hazard by Using Remote Sensing and Information Technologies". In: *Procedia Earth and Planetary Science*. World Multidisciplinary Earth Sciences Symposium, WMESS 2015 15 (2015), pp. 257–262. ISSN: 1878-5220. DOI: 10.1016/j.proeps.2015.08.063. URL: http://www.sciencedirect.com/science/article/pii/S1878522015003264 (visited on 12/12/2016).

[36] F. de Morsier. "Semi-supervised and unsupervised kernel-based novelty detection with application to remote sensing images". In: (2014).

[37] A. M. Nguyen, J. Yosinski, and J. Clune. "Deep Neural Networks are Easily Fooled: High Confidence Predictions for Unrecognizable Images". In: *CoRR* abs/1412.1897 (2014). arXiv: 1412.1897. URL: http://arxiv.org/abs/1412.1897.

[38] W. Ouerghemmi, A. Le-Bris, N. Chehata, and C. Mallet. "A Two-Step Decision Fusion Strategy: Application to Hyperspectral and Multispectral Images for Urban Classification". In: *ISPRS - International Archives of the Photogrammetry, Remote Sensing and Spatial Information Sciences*. Vol. XLII-1-W1. Copernicus GmbH, 2017, pp. 167–174.

[39] F. Pedregosa, G. Varoquaux, A. Gramfort, V. Michel, B. Thirion, O. Grisel, M. Blondel, P. Prettenhofer, R. Weiss, V. Dubourg, J. Vanderplas, A. Passos, D. Cournapeau, M. Brucher, M. Perrot, and E. Duchesnay. "Scikit-learn: Machine Learning in Python". In: *Journal of Machine Learning Research* 12 (2011), pp. 2825–2830.

[40] M. A. F. Pimentel, D. A. Clifton, L. A. Clifton, and L. Tarassenko. "A review of novelty detection". In: *Signal Processing* 99 (2014), pp. 215–249.

[41] T. Postadjian, A. L. Bris, H. Sahbi, and C. Mallet. "Investigating the Potential of Deep Neural Networks for Large-Scale Classification of Very High Resolution Satellite Images". In: vol. IV-1-W1. Copernicus GmbH, 2017, pp. 183–190. (Visited on 08/17/2017).

[42] D. A. Reynolds. "Gaussian Mixture Models". In: *Encyclopedia of Biometrics*. 2009.

[43] O. Ronneberger, P. Fischer, and T. Brox. "U-net: Convolutional networks for biomedical image segmentation". In: *International Conference on Medical Image Computing and Computer-Assisted Intervention*. Springer. 2015, pp. 234–241.

[44] C. Rupprecht, I. Laina, R. DiPietro, and M. Baust. "Learning in an Uncertain World: Representing Ambiguity Through Multiple Hypotheses". In: *2017 IEEE International Conference on Computer Vision (ICCV)* (2017), pp. 3611–3620.

[45] J. Schmidhuber. "Deep learning in neural networks: An overview". In: *Neural networks : the official journal of the International Neural Network Society* 61 (2015), pp. 85–117.

[46] SciPy.org Documentation. *Scipy.org Reference Guide, Statistical functions (scipy.stats)*. 2014. URL: `https://docs.scipy.org/doc/scipy-0.14.0/reference/generated/scipy.stats.multivariate_normal.html` (visited on 01/05/2018).

[47] E. Shelhamer, J. Long, and T. Darrell. "Fully Convolutional Networks for Semantic Segmentation". In: *2015 IEEE Conference on Computer Vision and Pattern Recognition (CVPR)* (2015), pp. 3431–3440.

[48] N. Srivastava, G. E. Hinton, A. Krizhevsky, I. Sutskever, and R. Salakhutdinov. "Dropout: a simple way to prevent neural networks from overfitting". In: *Journal of Machine Learning Research* 15 (2014), pp. 1929–1958.

[49] A. Subramanya, S. Srinivas, and R. V. Babu. "Confidence estimation in Deep Neural networks via density modelling". In: *CoRR* abs/1707.07013 (2017).

[50] R. Sun and C. H. Lampert. "KS(conf): A Light-Weight Test if a ConvNet Operates Outside of Its Specifications". In: *CoRR* abs/1804.04171 (2018).

[51] L. Szymanski and B. McCane. "Visualising kernel spaces". In: 2011.

[52] D. Tuia, E. Pasolli, and W. Emery. "Using active learning to adapt remote sensing image classifiers". In: *Remote Sensing of Environment* 115.9 (2011), pp. 2232–2242. ISSN: 0034-4257. DOI: `https://doi.org/10.1016/j.rse.2011.04.022`. URL: `http://www.sciencedirect.com/science/article/pii/S0034425711001507`.

[53] D. Tuia, M. Volpi, L. Copa, M. F. Kanevski, and J. Muñoz-Marí. "A Survey of Active Learning Algorithms for Supervised Remote Sensing Image Classification". In: *IEEE Journal of Selected Topics in Signal Processing* 5 (2011), pp. 606–617.

[54] M. Volpi and V. Ferrari. "Semantic segmentation of urban scenes by learning local class interactions". In: *2015 IEEE Conference on Computer Vision and Pattern Recognition Workshops (CVPRW)* (2015), pp. 1–9.

[55] M. Volpi and D. Tuia. "Dense semantic labeling of sub-decimeter resolution images with convolutional neural networks". In: *IEEE Trans. Geoscience and Remote Sensing* 55 (2017), pp. 881–893.

[56] Y. Wang, J. Wong, and A. Miner. "Anomaly intrusion detection using one class SVM". In: *Proceedings from the Fifth Annual IEEE SMC Information Assurance Workshop, 2004.* (2004), pp. 358–364.

[57] C. Wendl. *Confidence Estimation for Convolutional Neural Networks using Density Trees*. 2017. URL: `https://github.com/CyrilWendl/SIE-Project` (visited on 05/15/2018).

[58] J. A. Womble, B. J. Adams, and K. C. Mehta. "Automated Building Damage Assessment Using Remote-Sensing Imagery". In: *Proceedings of the ASCE/SEI Structures Congress*. 2007. URL: `http://ascelibrary.org/doi/abs/10.1061/40943(250)8` (visited on 01/01/2017).

[59] H. Zaragoza and F. d'Alché-Buc. "Confidence Measures for Neural Network Classifiers". In: *Proceedings of the Seventh Int. Conf. Information Processing and Management of Uncertainty in Knowlegdege-Based Systems (IPMU)*. Vol. 1. Editions EDK (Paris), Jan. 1998, pp. 886–893. URL: `https://www.microsoft.com/en-us/research/publication/confidence-measures-for-neural-network-classifiers/`.

[60] X. xiang Zhu, D. Tuia, L. Mou, G.-S. Xia, L. Zhang, F. Xu, and F. Fraundorfer. "Deep learning in remote sensing: a review". In: *CoRR* abs/1710.03959 (2017).

[61] A. M. Zoubir and D. R. Iskander. "Bootstrap Methods and Applications". In: *IEEE Signal Processing Magazine* 24 (2007), pp. 10–19.

9 Appendices

A Code Documentation

The implementation of the Density Forest code can be found on GitHub: `https://github.com/CyrilWendl/SIE-Master`. Jupyter notebooks are available to illustrate results of the novelty detection methods applied to all datasets:

1. Synthetic dataset: In `/Code/Density Forest.ipynb`
2. MNIST dataset: In `/MNIST/MNIST Novelty Detection.ipynb`
3. Zurich dataset: In `/Zurich/Zurich Novelty Detection.ipynb`

B Random Forest

The results of the Decision Tree applied to synthetic data are shown in figure B.1. The ruggedness of the decision boundaries is in part due to visualizing the decision boundaries on a discrete coordinate mesh.

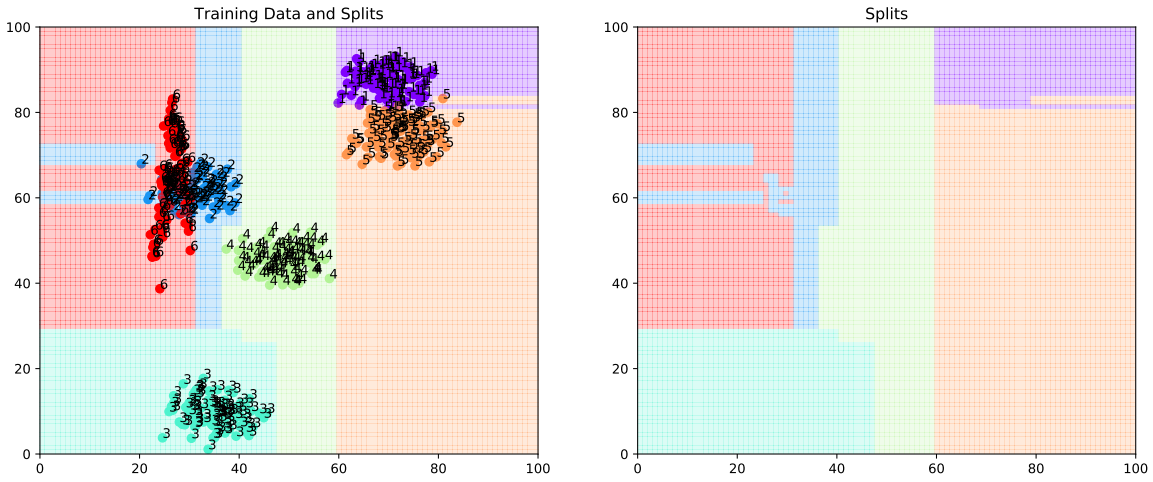

Figure B.1: Decision boundaries of a single Decision Tree on 2-dimensional synthetic data, splitting the data until every leaf node only contains data of one cluster. Left: decision boundaries with Data, right: decision boundaries only. The Decision Tree clearly overfits the data.

The Decision Tree with unlimited depth clearly overfits the data and tends to produce edgy boundaries. The associated Decision Tree is shown in figure B.2.

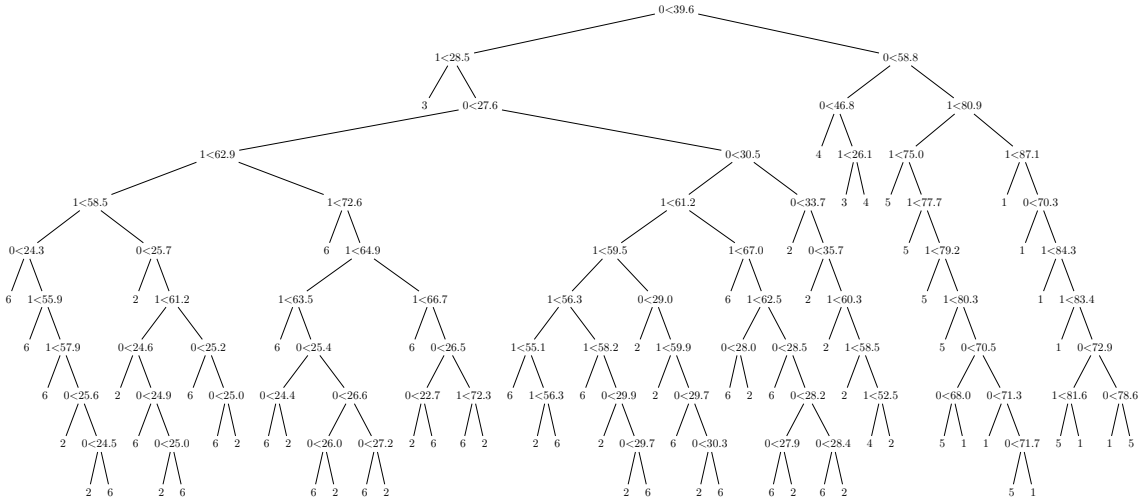

Figure B.2: Decision tree with unlimited depth on the training data for shown for illustrative purposes, with the split dimension and value at every non-leaf node and the class label at every leaf node. The tree clearly overfits the data and produces edgy decision boundaries

The classification using Random Forest is shown in figure B.3.

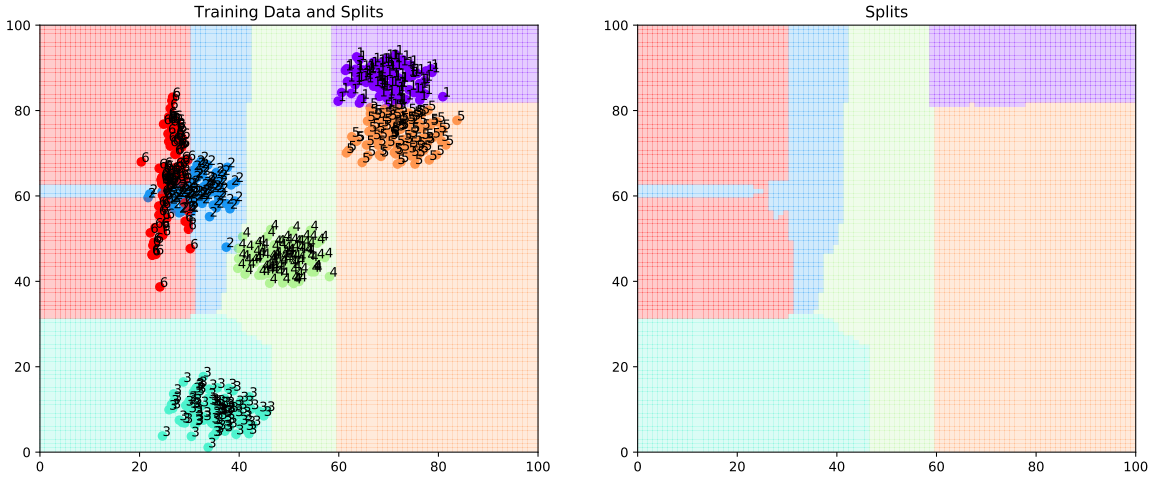

Figure B.3: Decision boundaries of a Random Forest on 2-dimensional synthetic data. 1000 Decision Trees have been trained on a 30% bootstrap sample of the original data. Left: decision boundaries with Data, right: decision boundaries only. The Random Forest manages to smooth out the class decision boundaries.

C Data Structure

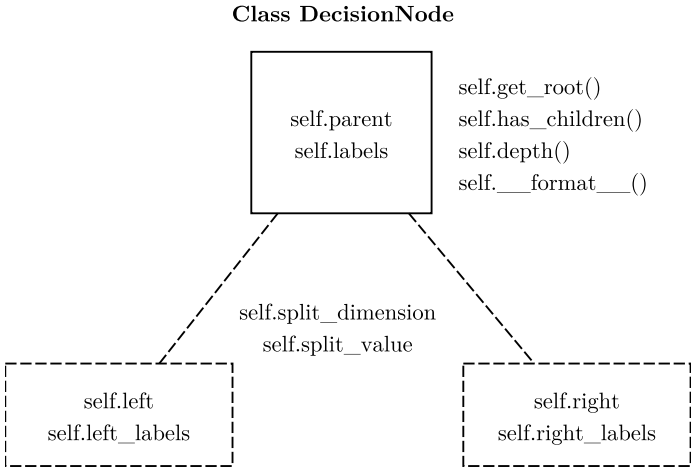

Figure C.1: Implemented data structure for Decision Tree nodes. Every node saves a pointer to its parent, the unique labels contained at its split level, the split dimension and value, methods for tree descending and formatting as well information about its child nodes.

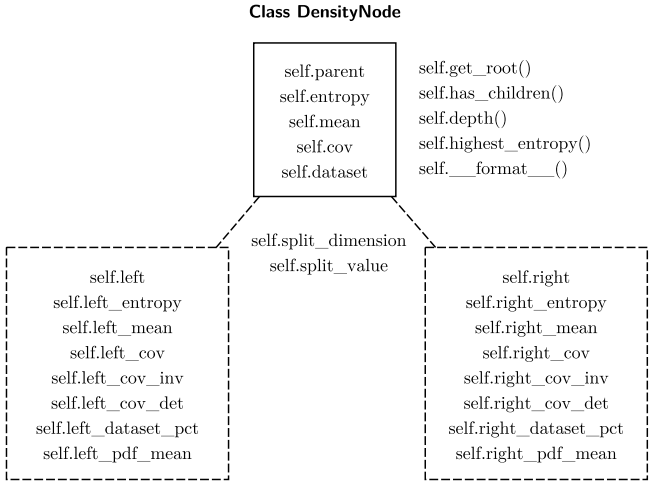

Figure C.2: Implemented data structure for Density Tree nodes. Every node saves a pointer to its parent, the unique labels contained at its split level, the split dimension and value, methods for tree descending and formatting as well information about its child nodes. In addition, every root node pre-stores the inverse and determinant of the covariance matrix of both clusters situated to the right and left of the node for faster calculation of the Gaussian PDF.

D MNIST Evaluation Metrics

Left-out class	Training set		Test set	
	OA	AA	OA	AA
0	99.29	99.30	99.01	99.02
1	99.21	99.21	98.97	98.98
2	99.34	99.35	98.80	98.80
3	99.27	99.27	99.12	99.12
4	99.33	99.32	98.95	98.93
5	99.46	99.46	99.11	99.11
6	99.36	99.36	98.94	98.94
7	99.39	99.38	99.20	99.19
8	99.38	99.38	99.03	99.04
9	99.39	99.39	99.19	99.18

Table D.1: Accuracy metrics in % for the CNN trained on $N-1$ classes for the MNIST dataset

Left-Out Class	MSR	Margin	Entropy	MC-Dropout	GMM	OC-SVM	DF
0	0.98	0.98	**0.98**	0.98	0.83	0.93	0.43
1	0.99	0.99	**0.99**	0.99	0.96	0.91	0.47
2	0.97	0.97	**0.97**	0.96	0.77	0.82	0.55
3	0.96	0.96	**0.96**	0.96	0.89	0.87	0.69
4	0.92	0.92	0.93	0.91	0.79	**0.95**	0.45
5	0.96	0.96	**0.96**	0.96	0.46	0.87	0.41
6	0.97	0.97	**0.97**	0.97	0.85	0.92	0.63
7	0.97	0.97	**0.97**	0.96	0.94	0.88	0.40
8	0.98	0.98	**0.98**	0.98	0.82	0.90	0.61
9	0.98	0.98	**0.98**	0.98	0.92	0.92	0.70
Mean	0.97	0.97	**0.97**	0.97	0.82	0.90	0.53

Table D.2: AUROC for each left-out class in the MNIST dataset

E Zurich Network Architecture

Name	Layer	Properties
	Input	Dim: $(\|b\|, w, h, n_c)$
	Conv. + ReLu	32 5×5 filt.
	Dropout	$p = .1$
`conv1`	Conv. + ReLu	32 5×5 filt.
	MaxPooling	2×2 pool size
	Conv. + ReLu	64 3×3 filt.
	Dropout	$p = .1$
`conv2`	Conv. + ReLu	64 3×3 filt.
	MaxPooling	2×2 pool size
	Conv. + ReLu	128 3×3 filt.
	Dropout	$p = .1$
`conv3`	Conv. + ReLu	128 3×3 filt.
	MaxPooling	2×2 pool size
	Conv. + ReLu	256 3×3 filt.
	Dropout	$p = .1$
`conv4`	Conv. + ReLu	256 3×3 filt.
	Conv. + ReLu	512 3×3 filt.
	MaxPooling	2×2 pool size
	Dropout	$p = .1$
`conv5`	Conv. + ReLu	512 3×3 filt.

(a) Downsampling Layers

Type	Remarks
Concat(Conv. T., `conv4`)	256 2×2 filt., 2 str
Conv. + ReLu	256 3×3 filt.
Dropout	$p = .1$
Conv. + ReLu	256 3×3 filt.
Concat(Conv. T., `conv3`)	128 2×2 filt., 2 str
Conv. + ReLu	128 3×3 filt.
Dropout	$p = .1$
Conv. + ReLu	128 3×3 filt.
Concat(Conv. T., `conv2`)	64 2×2 filt., 2 str
Conv. + ReLu	64 3×3 filt.
Dropout	$p = .1$
Conv. + ReLu	64 3×3 filt.
Concat(Conv. T., `conv1`)	32 2×2 filt., 2 str
Conv. + ReLu	32 5×5 filt.
Dropout	$p = .1$
Conv. + ReLu	32 5×5 filt.
Conv. + Softmax	8 1×1 filt.

(b) Upsampling Layers

Table E.1: U-Net Architecture of the CNN used for Zurich Dataset, according to Ronneberger et al. [43]. Conv. = convolution, filt = filters, str = stride, p = dropout probability, dim = dimensions, Input dimensions $|b|, w, h, n_c$ = batch size, width, height, number of channels. A convolution or transpose convolution always takes the previous layer in the network as input.

F MNIST Dataset Figures

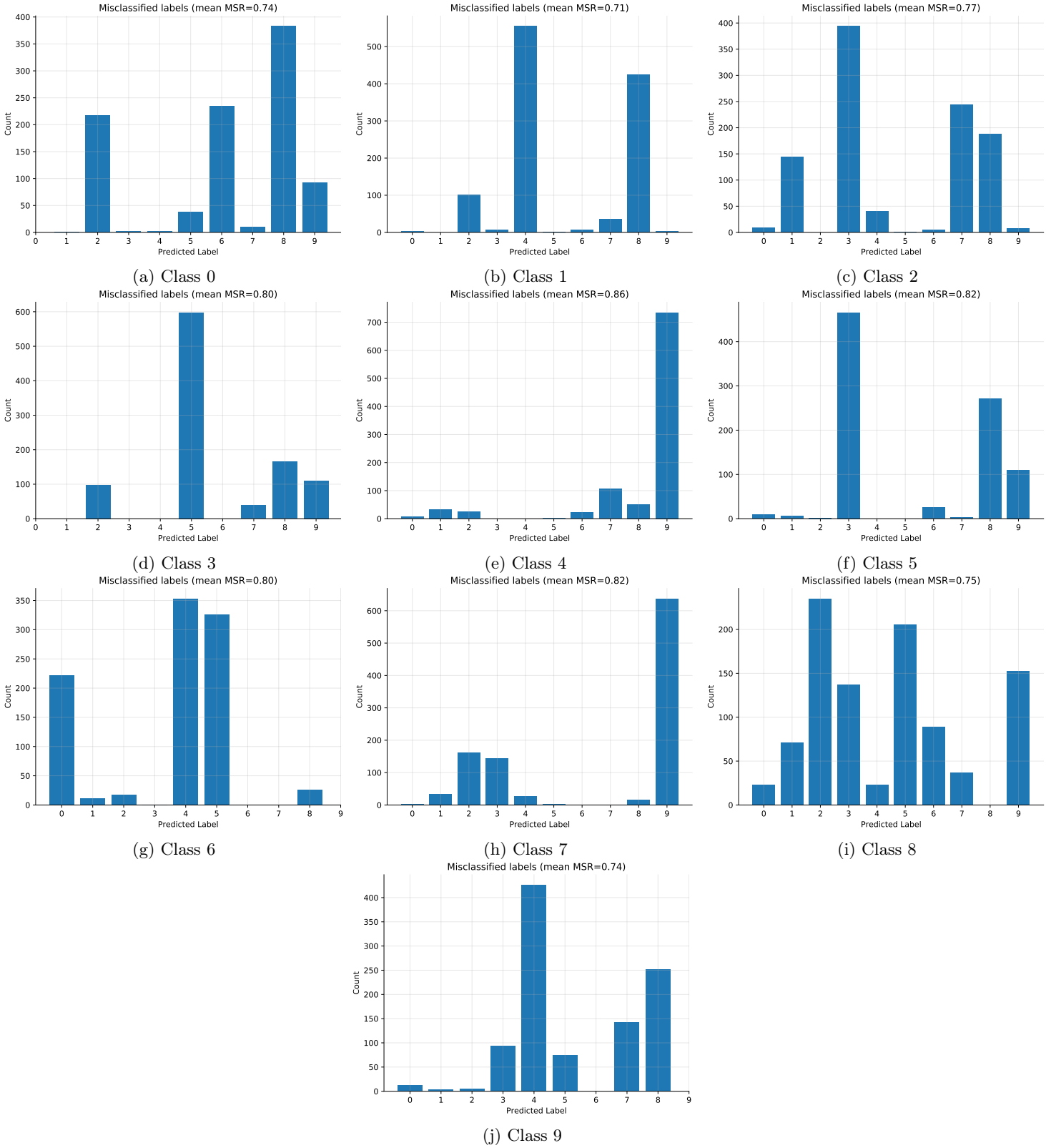

(a) Class 0 (b) Class 1 (c) Class 2

(d) Class 3 (e) Class 4 (f) Class 5

(g) Class 6 (h) Class 7 (i) Class 8

(j) Class 9

Figure F.1: Count of predictions for each left-out class

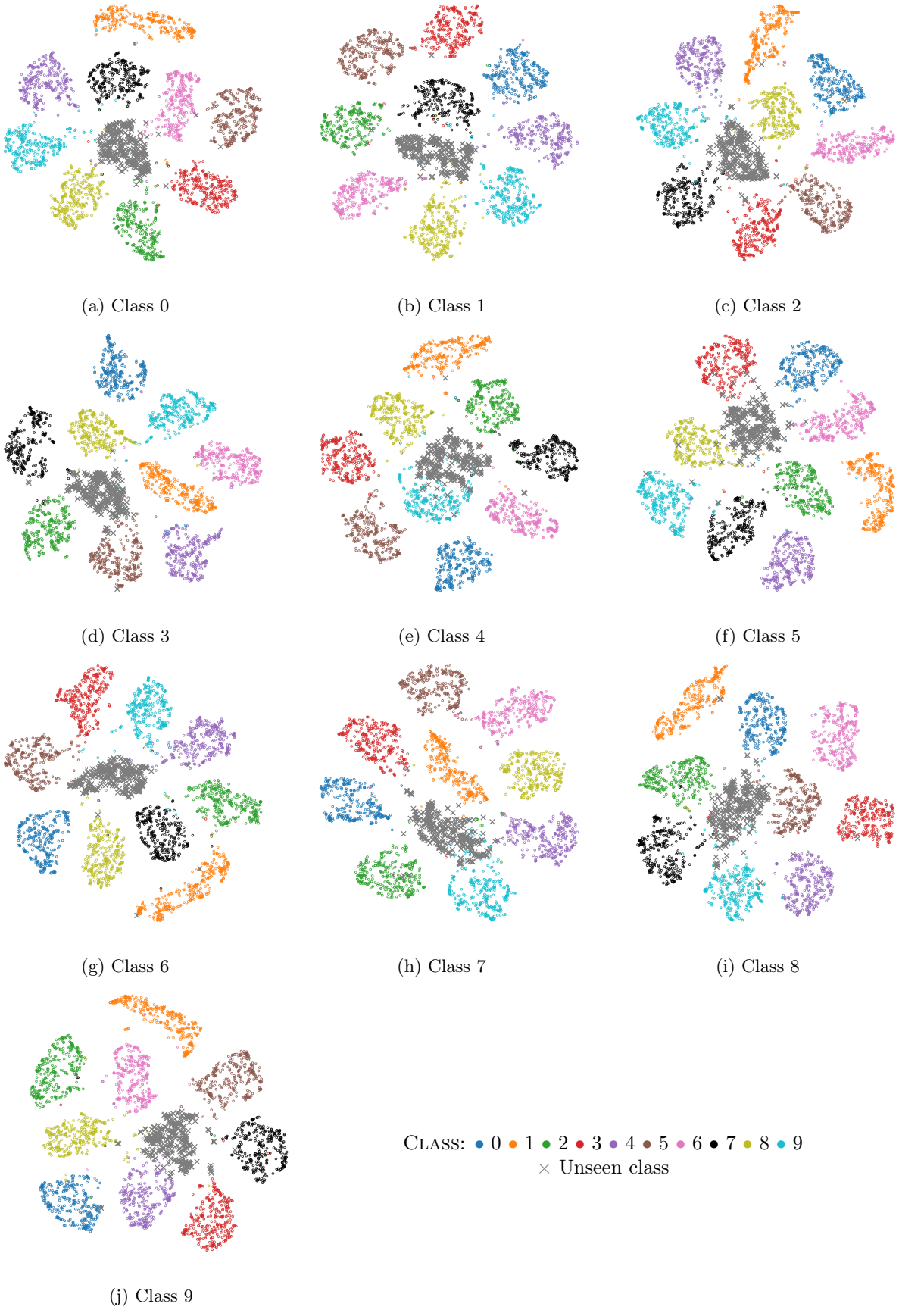

(a) Class 0 (b) Class 1 (c) Class 2

(d) Class 3 (e) Class 4 (f) Class 5

(g) Class 6 (h) Class 7 (i) Class 8

(j) Class 9

Figure F.2: t-SNE of MNIST dataset activations after PCA transformations for each left-out class

G Zurich Dataset Figures

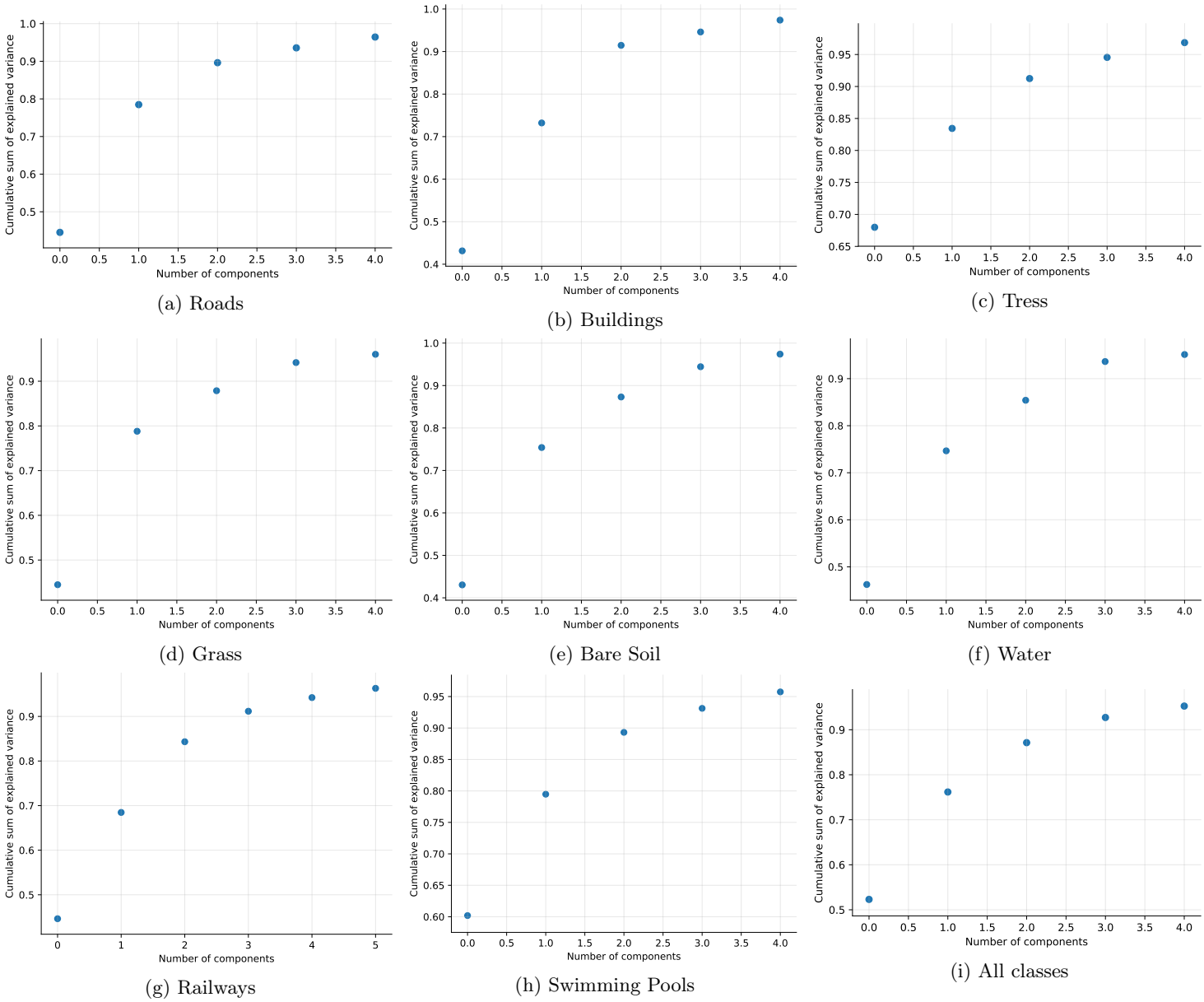

(a) Roads (b) Buildings (c) Tress

(d) Grass (e) Bare Soil (f) Water

(g) Railways (h) Swimming Pools (i) All classes

Figure G.1: Explained variance by first PCA components, for activations of each left-out class and for activations of the model trained on all classes. The number of PCA components was chosen such as to explain more than 95% of the variance.

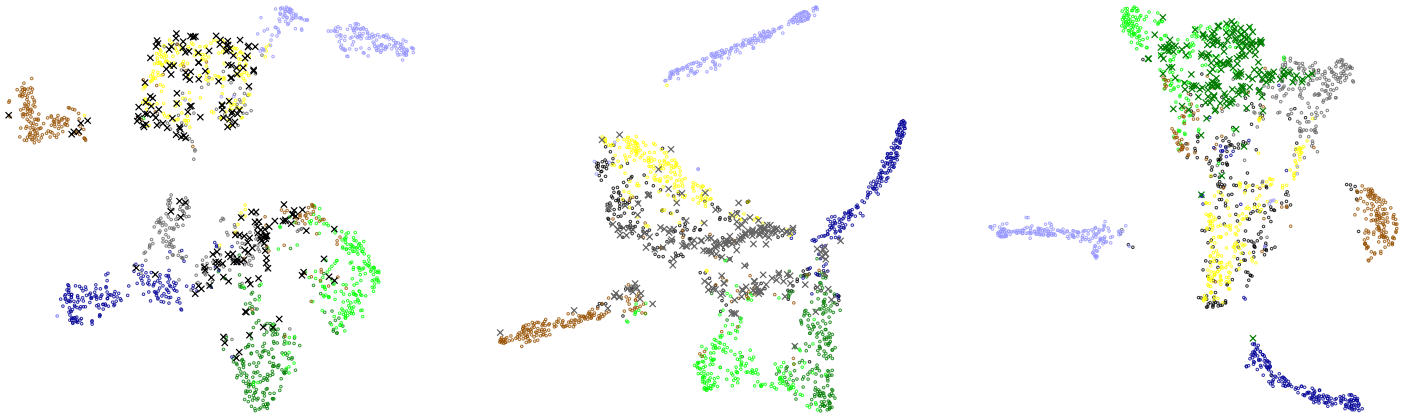

(a) Roads (b) Buildings (c) Tress

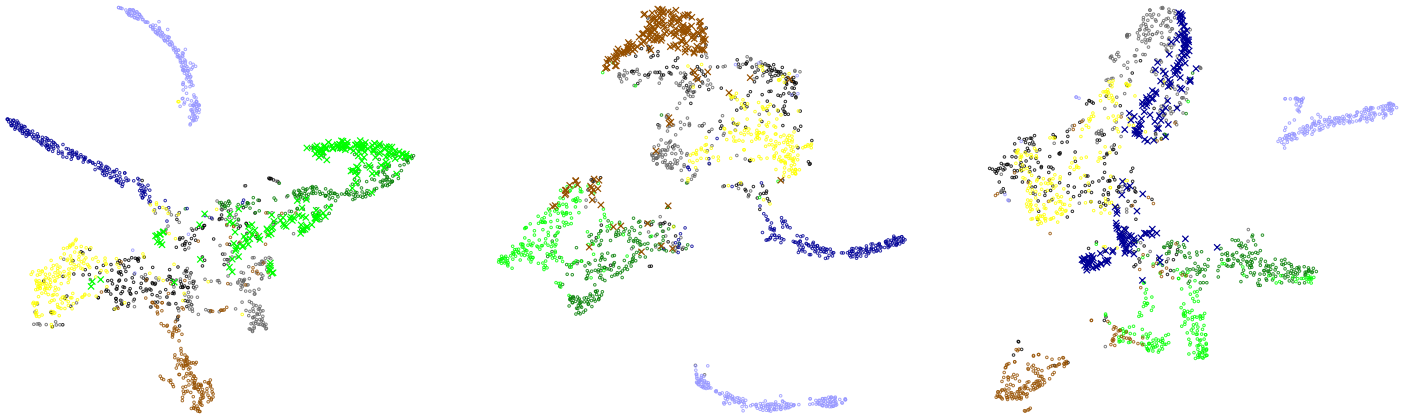

(d) Grass (e) Bare Soil (f) Water

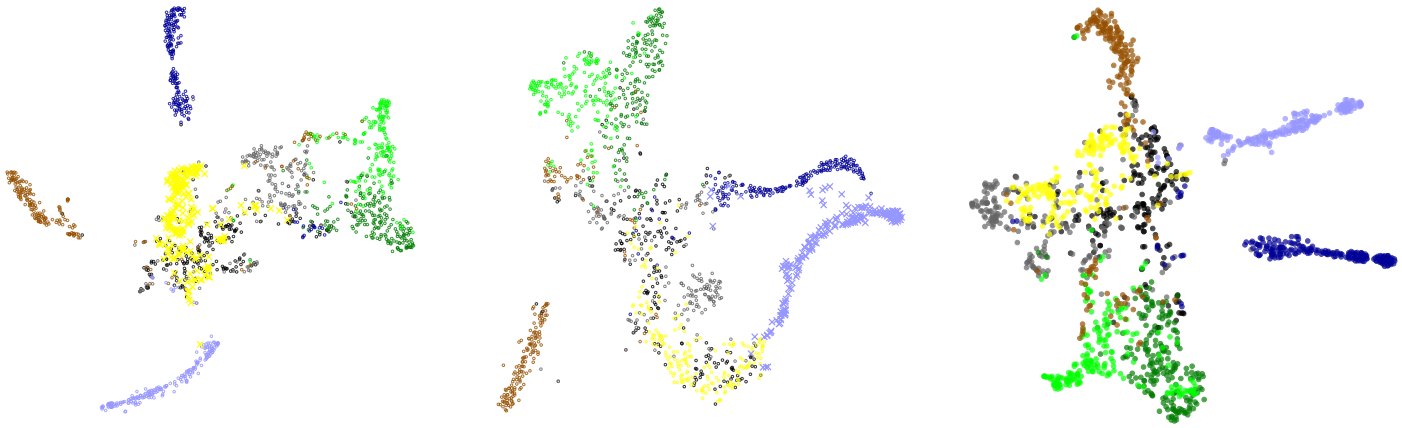

(g) Railways (h) Swimming Pools (i) All classes

Class: • Roads • Buildings • Trees • Grass
• Bare Soil • Water • Railways • Pools
× Unseen class

Figure G.2: t-SNE of Zurich dataset activations after PCA transformations for each left-out class and for the activations of the network trained on all classes. The same number of points are shown by class to show class separability, although the real class distribution is imbalanced (cf. table 8).

For each left-out model and each novelty detection method, visual results are shown below for one image (fig. G.3). More images can be found on `https://github.com/CyrilWendl/SIE-Master/tree/master/Figures/Zurich/Im_cert`.

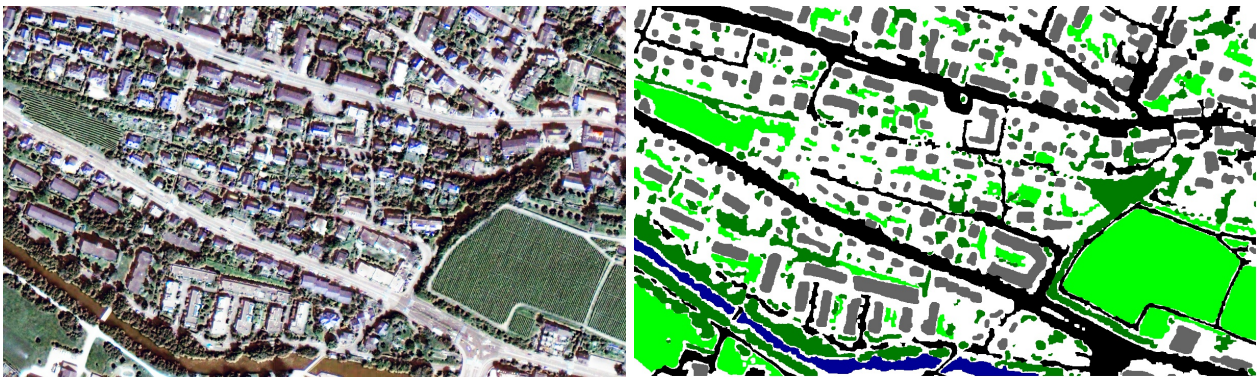

(a) Image (b) Ground Truth

Figure G.3: Image and ground truth for visualized novelty detection methods

On the following pages, confidence scores are shown for all left-out classes and for one confidence estimation method at a time. For each left-out class, the confidence values are shown for one image of the training set containing some object with the corresponding ground truth.

Note that in the some confidence images, not all the variation might be visible due to objects with particularly low values.

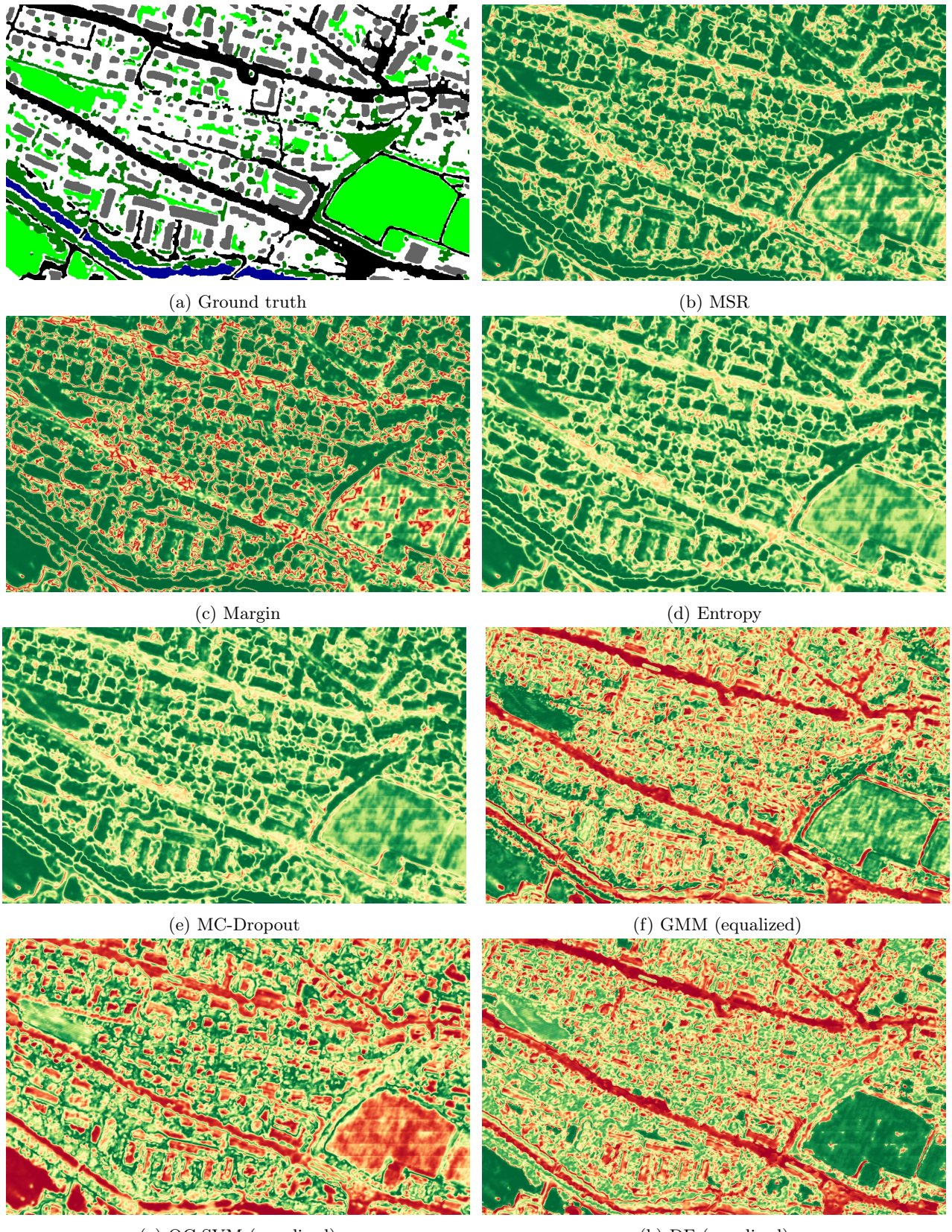

Figure G.4: Ground truth and visual results for left-out class “roads”.

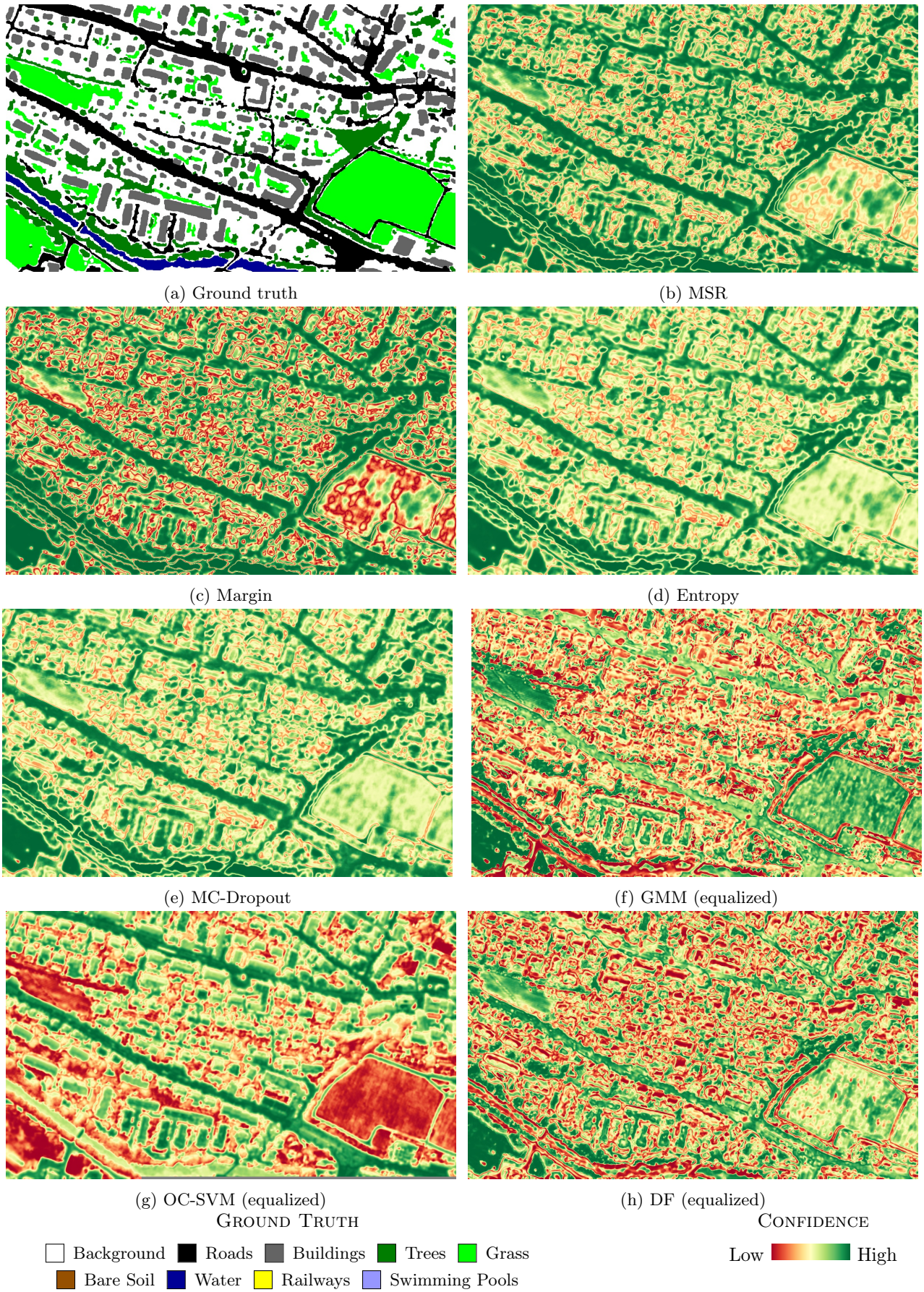

(a) Ground truth (b) MSR

(c) Margin (d) Entropy

(e) MC-Dropout (f) GMM (equalized)

(g) OC-SVM (equalized) (h) DF (equalized)

Figure G.5: Ground truth and visual results for left-out class "buildings".

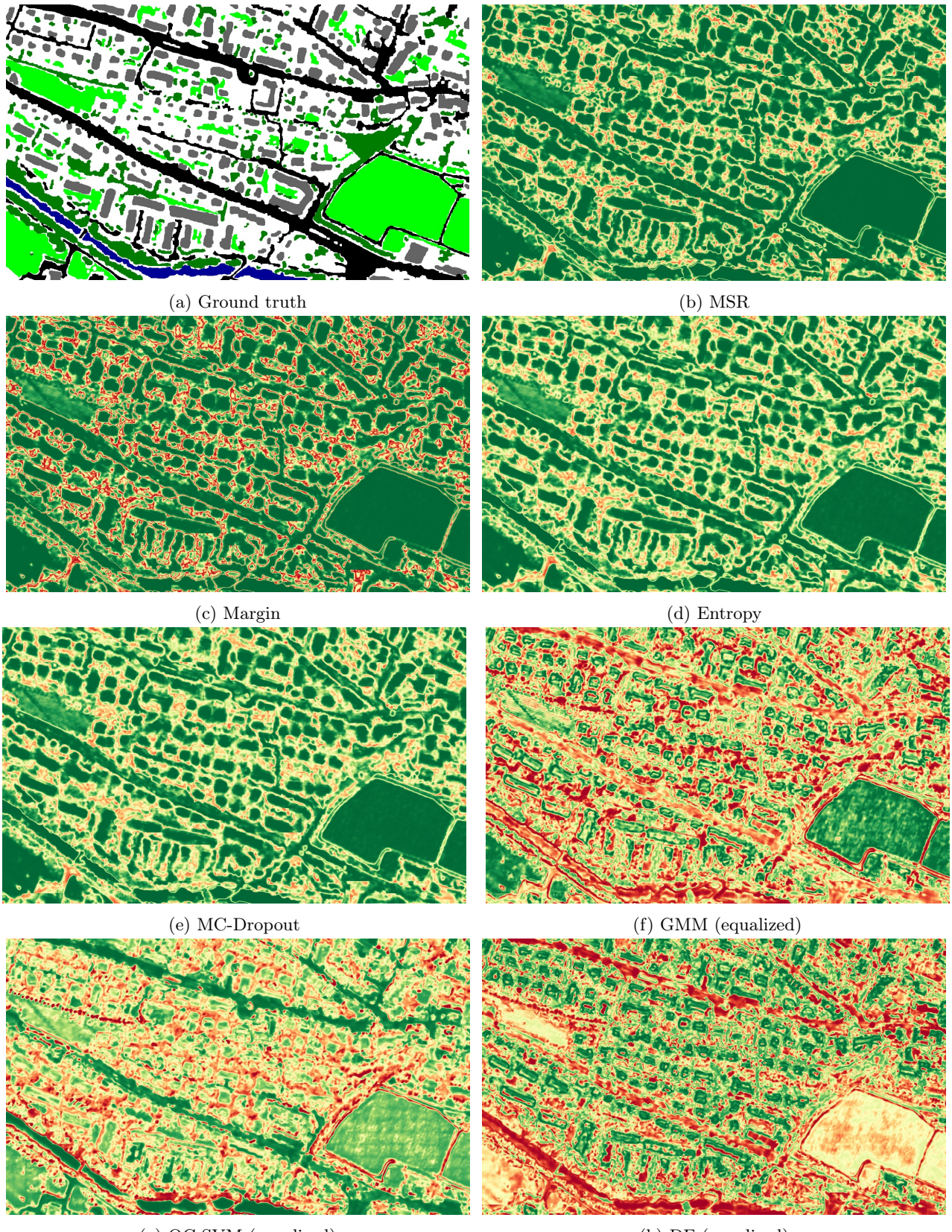

Figure G.6: Ground truth and visual results for left-out class “trees”.

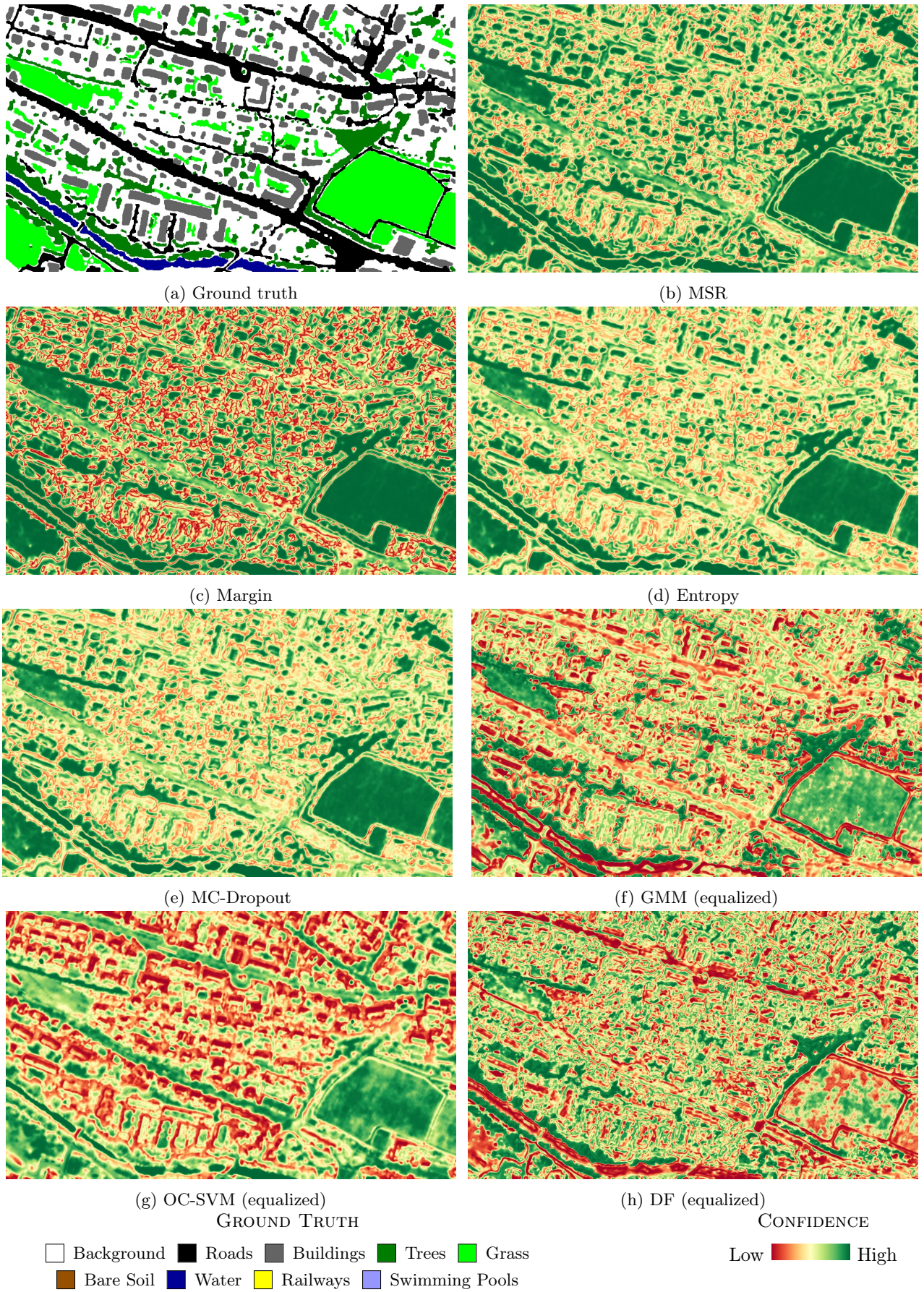

(a) Ground truth (b) MSR

(c) Margin (d) Entropy

(e) MC-Dropout (f) GMM (equalized)

(g) OC-SVM (equalized) (h) DF (equalized)

Figure G.7: Ground truth and visual results for left-out class “grass”.

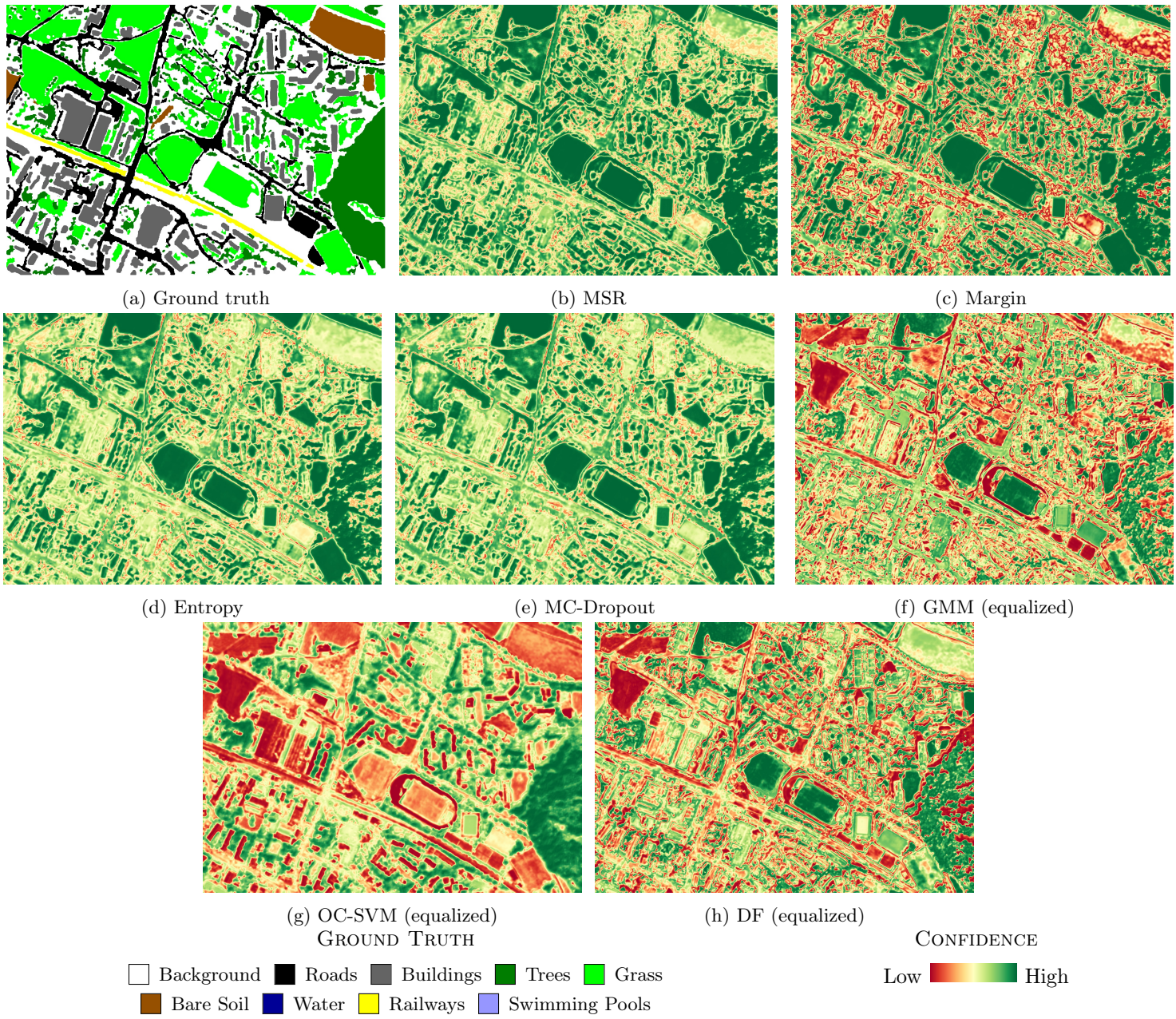

(a) Ground truth (b) MSR (c) Margin

(d) Entropy (e) MC-Dropout (f) GMM (equalized)

(g) OC-SVM (equalized) (h) DF (equalized)

Figure G.8: Ground truth and visual results for left-out class "bare soil".

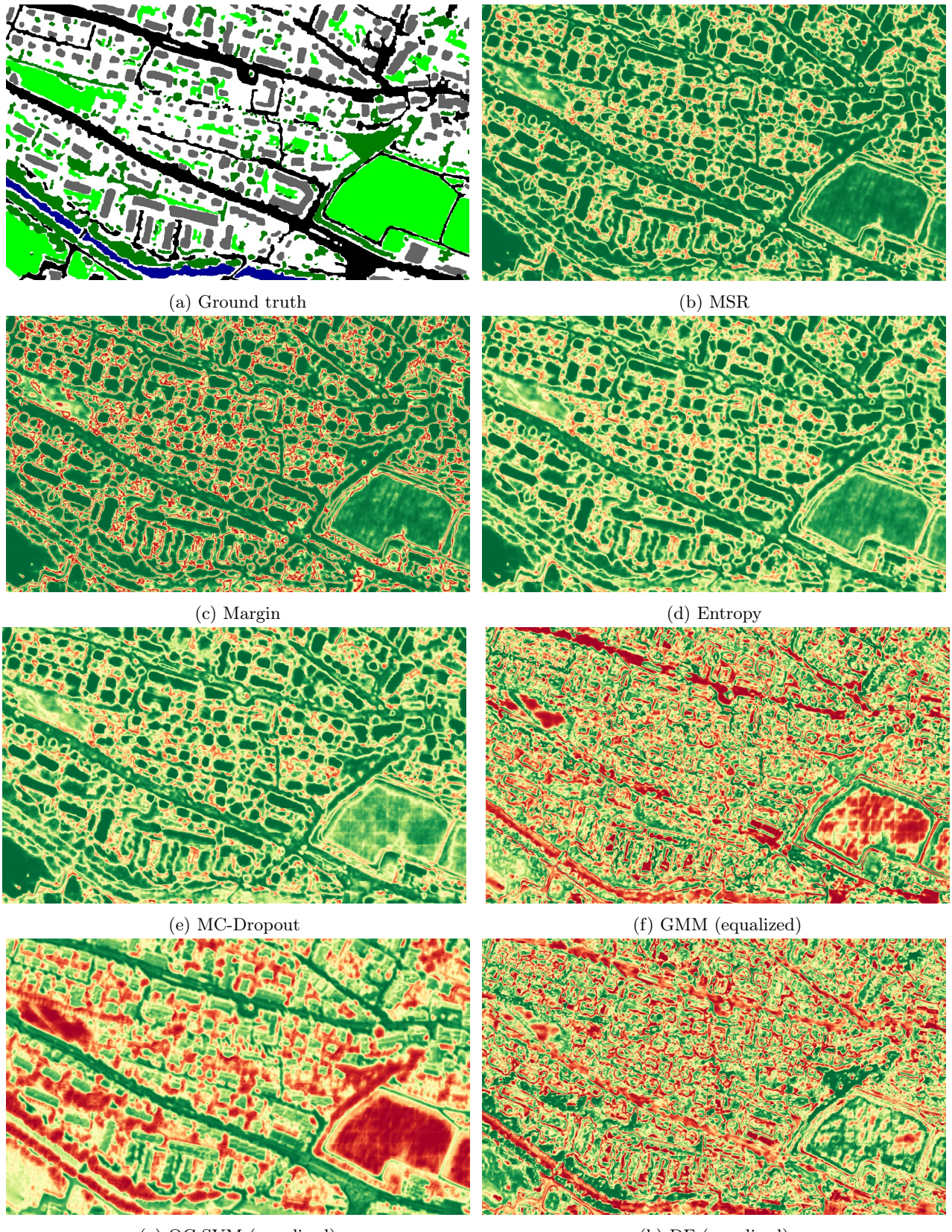

Figure G.9: Ground truth and visual results for left-out class "water".

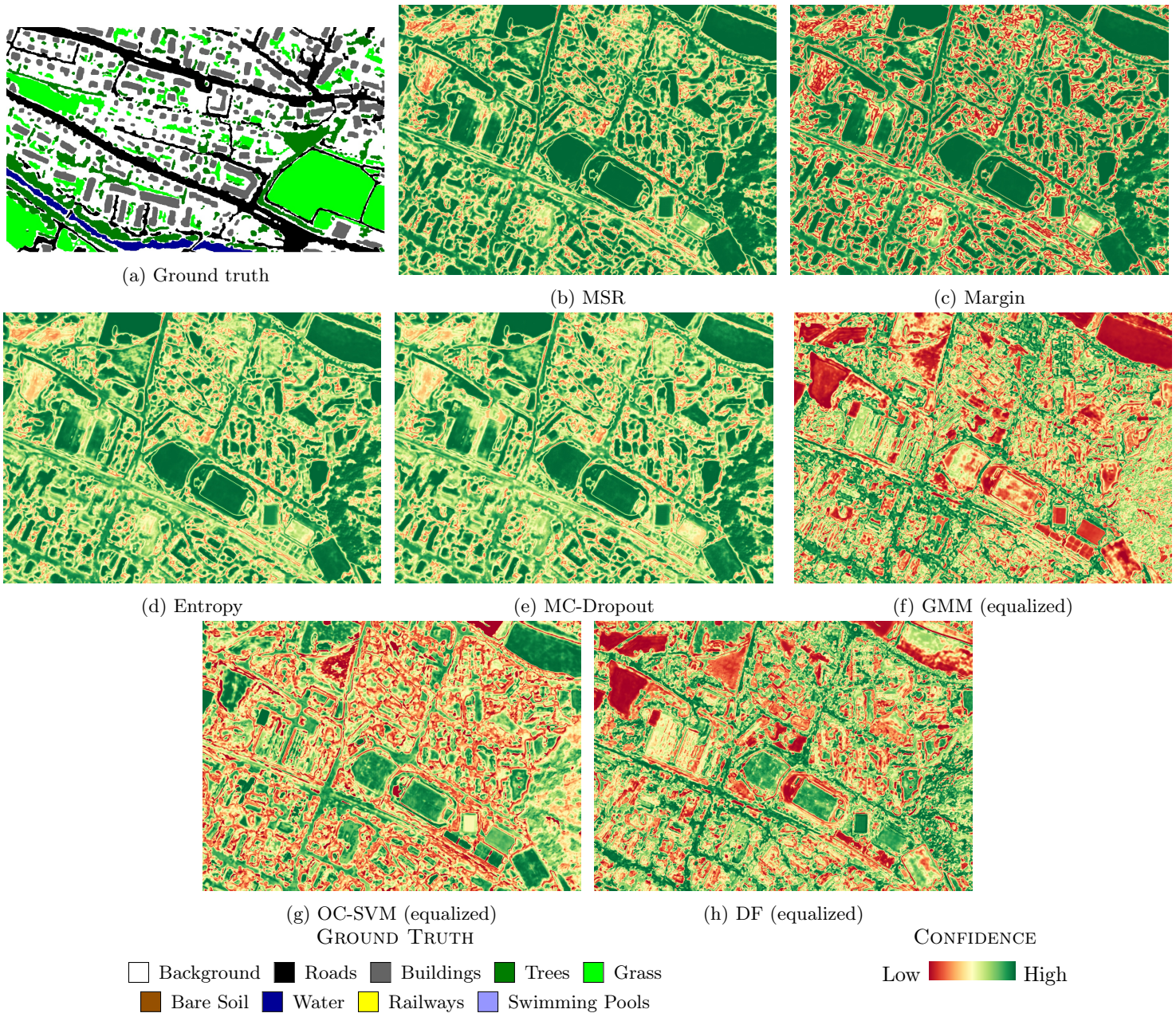

Figure G.10: Ground truth and visual results for left-out class “railways”.

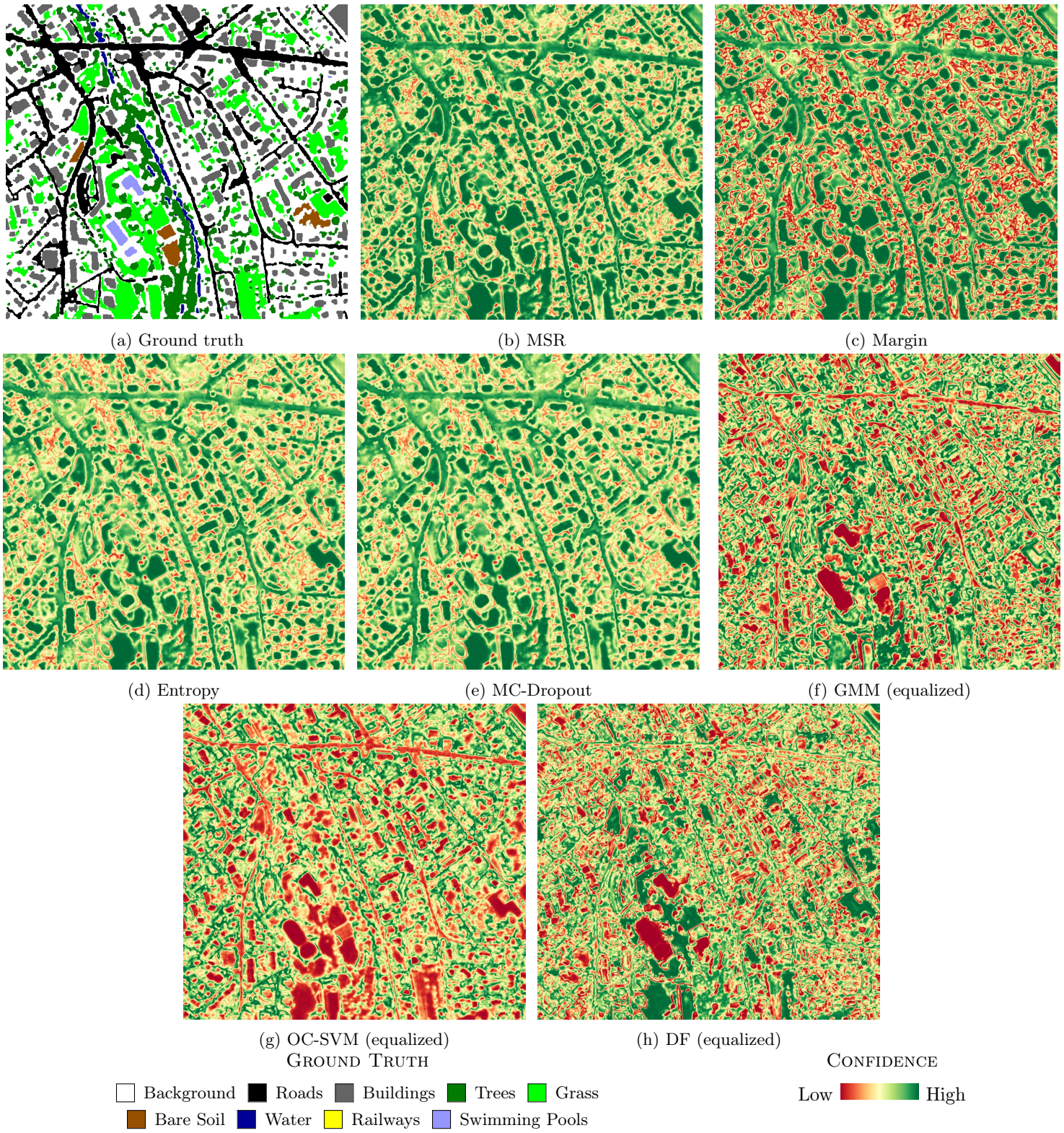

Figure G.11: Ground truth and visual results for left-out class “swimming pools”.

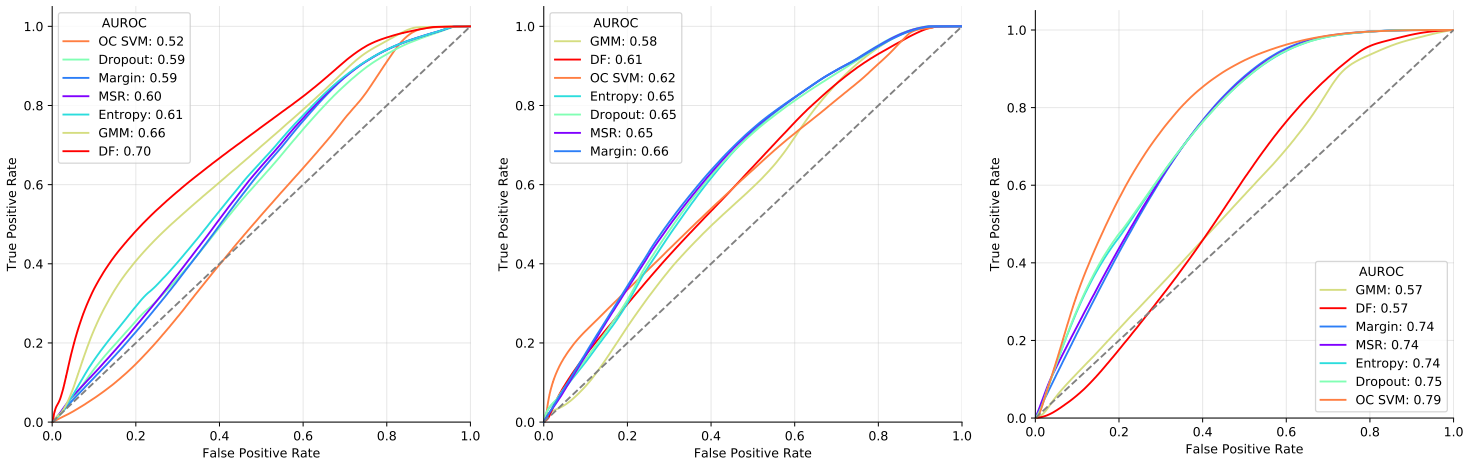

(a) Roads

(b) Buildings

(c) Trees

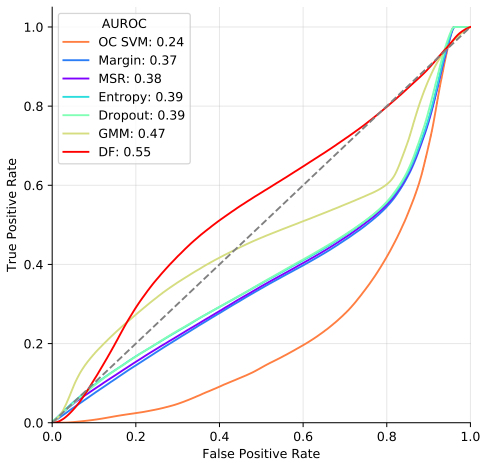

(d) Grass

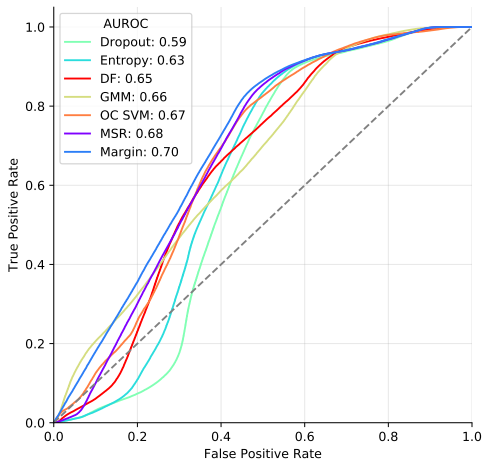

(e) Bare Soil

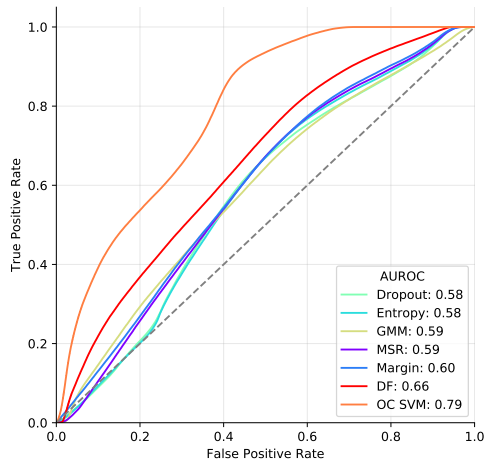

(f) Water

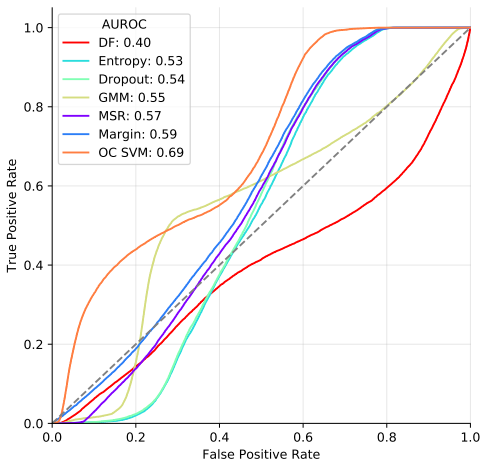

(g) Railways

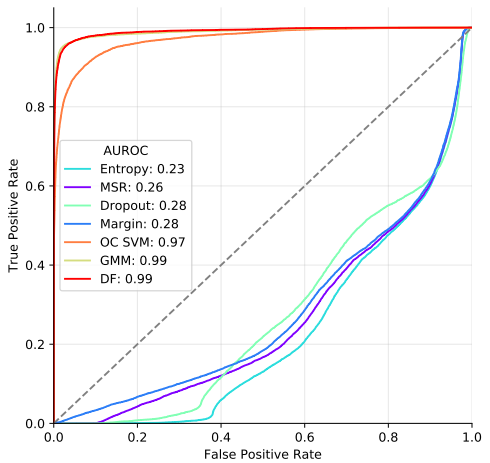

(h) Swimming Pools

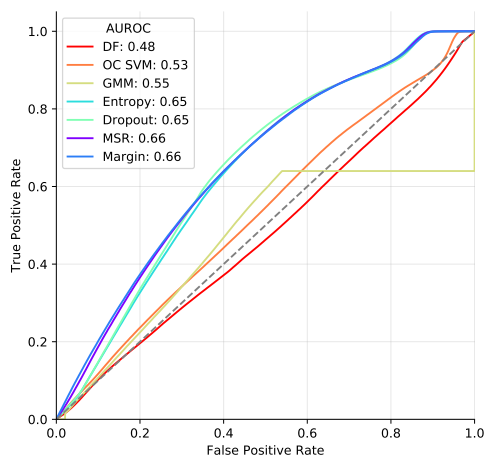

(i) Error Detection

Figure G.12: ROC curves of confidence measures for novelty detection and for error detection

H Hyperparameter Search Results

Hyperparameters were searched in the following ranges:

1. GMM
   - Components: `1 - 10`
2. OC-SVM
   - Kernel: `RBF`, `poly`
   - Degree: `1 - 3` (only for `poly`)
   - Nu: `1e-4, 1e-3, 1e-2, .1, .3, .5`
3. Density Forests:
   - Maximum depth: `2, 3, 4, 5`
   - Minimum IG: `0, .3, .7`

The minimum Information Gain parameter is rather difficult to tune, since it is usually smaller for higher-dimensional data. It can however still have an important effect by avoiding unnecessary splits (table 2).

Hyperparameter search results for the MNIST dataset and for the Zurich dataset using the hyperparameter search scheme shown in fig. 11 are represented in tables H.1 and H.2.

Method	GMM	OC-SVM			Density Forest	
Hyperparameter	Components	Kernel	Degree	Nu	Depth	Min. IG
0	8	poly	15	.1	2	.7
1	8	poly	15	.01	2	.7
2	9	poly	5	.5	4	.3
3	9	poly	13	.01	4	.7
4	4	poly	3	.3	4	.7
5	5	poly	3	.5	5	0
6	9	poly	15	.01	5	0
7	6	poly	15	.1	2	.5
8	8	poly	15	.1	2	0
9	7	poly	9	.3	4	.3

Table H.1: Best hyperparameters for the MNIST Dataset

Method	GMM	OC-SVM			Density Forest	
Hyperparameter	Components	Kernel	Degree	Nu	Depth	Min. IG
Roads	3	poly	2	0.001	1	0
Buildings	5	poly	1	0.001	3	0
Trees	4	poly	1	0.010	1	.7
Grass	3	poly	1	0.001	3	0
Bare Soil	9	poly	1	0.500	1	0
Water	3	poly	1	0.001	1	0
Railways	9	poly	3	0.500	3	.7
Swimming Pools	3	RBF	-	0.500	3	.7

Table H.2: Best hyperparameters for the Zurich Dataset

Regarding OC-SVM, in most cases, a polynomial kernel of degree 1 was found optimal. This makes sense, since a neural network performs the task of making data linearly separable.

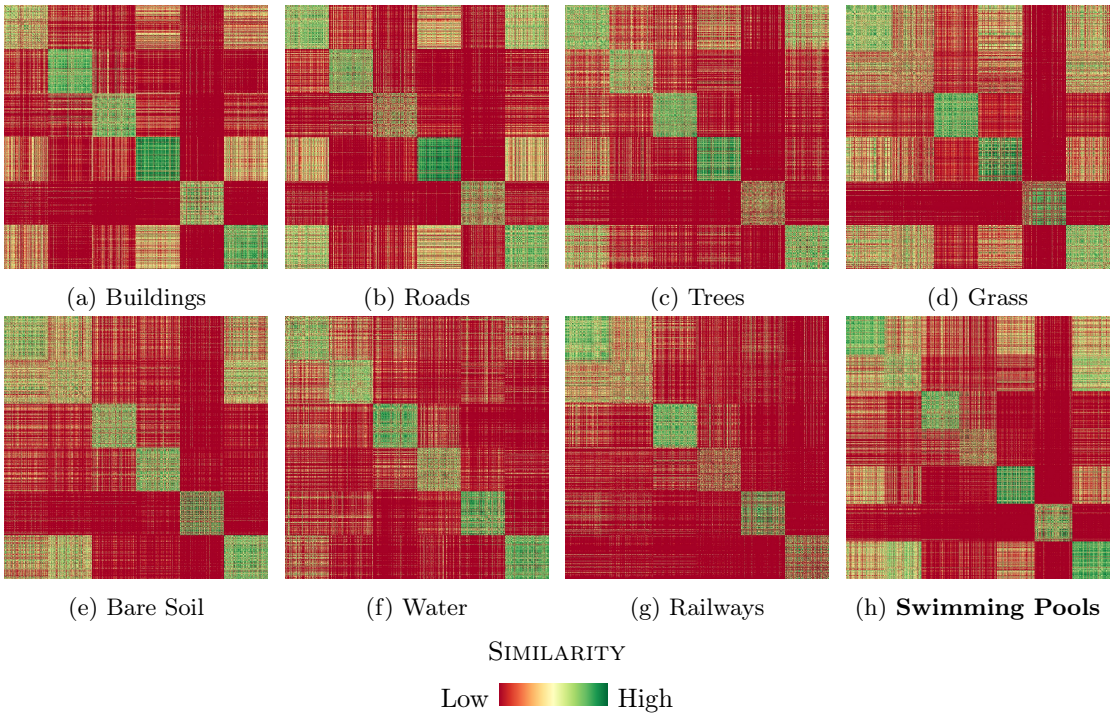

Figure H.1: RBF Kernel visualizations for One-Class Support Vector Machines in Zurich dataset. Kernels were applied to a class-balanced subsample of training activations belonging to the seen classes. Best kernels found using hyperparameter search are labelled in bold.

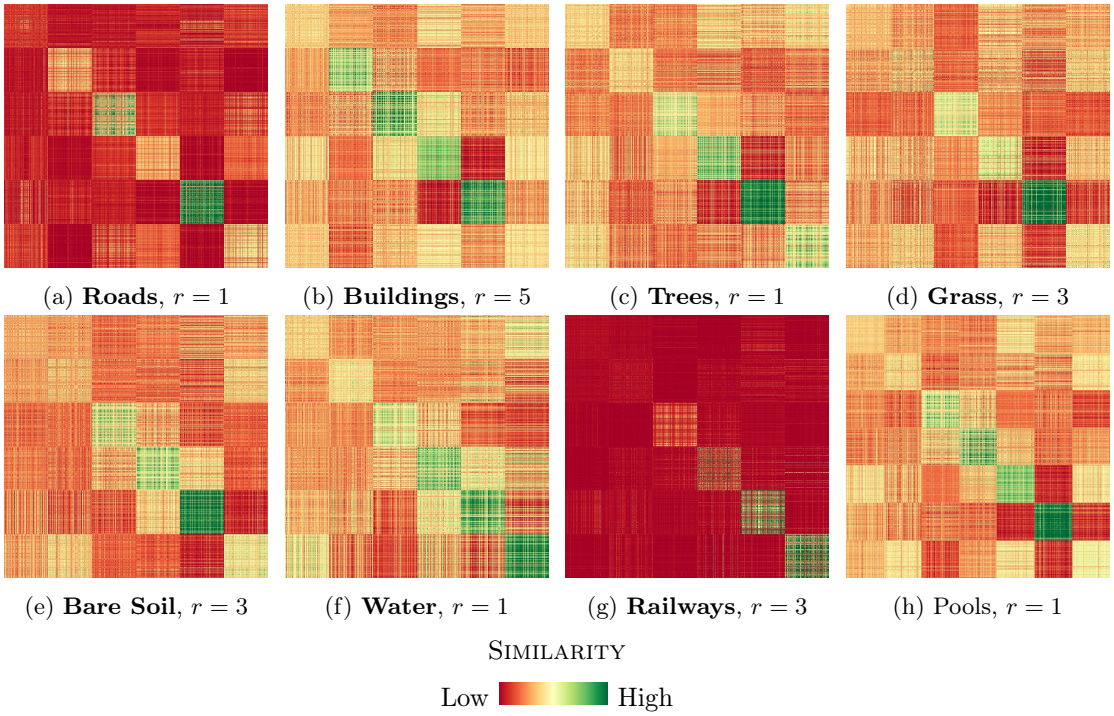

(a) **Roads**, $r = 1$ (b) **Buildings**, $r = 5$ (c) **Trees**, $r = 1$ (d) **Grass**, $r = 3$

(e) **Bare Soil**, $r = 3$ (f) **Water**, $r = 1$ (g) **Railways**, $r = 3$ (h) Pools, $r = 1$

Figure H.2: Polynomial kernel visualizations for One-Class Support Vector Machines in Zurich dataset with best degree r. Kernels were applied to a class-balanced subsample of training activations belonging to the seen classes. Contrast stretching has been applied to the images of the polynomial kernels to highlight more local variation. Best kernels found using hyperparameter search are labelled in bold.